MULTIFUNCTIONALITY OF POROUS COPPER MANUFACTURED BY LOST CARBONATE SINTERING

Thesis submitted in accordance with the requirements of the University of Liverpool for the degree of Doctor in Philosophy

by

David John Thewsey

January, 2009

ABSTRACT

Over the last few decades, porous metals have been receiving a large amount of interest in industry due to the rapidly growing advancement in manufacturing techniques, design and possible applications. Their unique properties and multi-functionality allow them to be utilized in many different uses throughout different industrial sectors. There is a huge range of metallic foams that can be produced implementing different metals, alloys and cellular structures giving a combination of different properties. Industrial interests include impact/energy absorption, thermal management properties, acoustic properties and electrical properties. Metallic foams are still in the early stages of development and so the potential for more and more applications is still expanding rapidly. The relatively cheap production methods make many types of porous metals a cheap alternative to expensive engineering materials.

Thermal, electrical, permeability and sound absorption properties of copper foams are of particular interest. The samples tested for the thermal and sound absorption properties were made using the 'Lost Carbonate Sintering' method, which involves sintering copper granules around carbonate particles within a compact and over a set period of time. The carbonate particles are then removed by a dissolution process, leaving the sintered copper foam structure. The pores within this structure are therefore virtual replicas of the carbonate particles. For this reason, the pore size and porosity of the porous metal are easily controlled.

Thermal and electrical conductivity tests have been carried out on a number of different porous metal specimens, with varying properties, using several different techniques. Correlations between the thermal and electrical conductivity with porosity and pore size have been obtained, showing some promising results.

An open-flow fluid arrangement was used on a range of samples to test the effects of pore size, porosity and pore shape on the permeability. The same test assembly, with a supplementary heating system allowed the heat transfer characteristics of the samples to be measured and correlated with pressure drops and flow rates, when water was used as the coolant. Pressure drops and heat transfer values ranged extensively amongst the test samples, with large pore sizes and low porosities showing excellent heat exchanging capabilities. Pressure drops observed were generally low, demonstrating promising potential for industrial applications.

Tests to measure the sound absorption properties of the foam samples were carried out according to the British Standards test procedure, using the Standing Wave impedance

tube method. Again, tests were carried out on a wide range of copper foam samples, with some unusual results obtained at particular frequencies.

ACKNOWLEDGMENTS

Primarily I would like to thank my Ph.D. supervisor, Dr. Yuyuan Zhao, for his technical advice, teaching, encouragement and invaluable direction throughout this research. It cannot be overstated how important his assistance and backing has been to me from start to finish.

I would like to give my sincere thanks to Dr. Liping Zhang for her priceless assistance with test sample preparation and experimental work. Her enthusiasm and kindness has been an inspiration to me.

I am grateful to Mr. Sozos Stopanos, Dr. Chris Sutcliffe, Mr. David Atkinson, Dr. Gary Seiffert, Prof. Barry Gibbs, Mr. Carl Slawson, Mr. Richard Roberts and Mr. Lawrence Bailey who have all helped in various ways with experimental work. My particular thanks go out to Mr. Lei Zhao for his assistance with quantitative metallography measurements.

I would also like to show my gratitude to the EPSRC for the privilege of a DTA award.

Lastly, I would like to thank my family and friends for their continued support and encouragement, without whom this thesis would not have been possible.

PUBLISHED WORK BY THE AUTHOR

D. J. Thewsey and Y. Y. Zhao, Thermal Conductivity of Porous Copper Manufactured by the Lost Carbonate Sintering Process, **Physica Status Solidi A, 205**(2008), 1126–1131.
DOI: 10.1002/pssa.200723121

LIST OF TABLES

LIST OF FIGURES

NOMENCLATURE

A	Area [m^2]
BSP	British Standard Pipe
C	Form Coefficient [m^{-1}]
C_P	Specific Heat Capacity [$JKg^{-1}K^{-1}$]
D	Diameter [m]
DC	Direct Current
E	Electric Field Intensity [Vm^{-1}]
H	Acoustic Absorption Transfer Function (Defined in Eq. 3.12 – 3.16)
I	Electric Current [A]
J	Current Density [Am^{-2}]
L	Test Line [m]
LCS	Lost Carbonate Sintering
K	Viscous Permeability [m^2]
NRC	Noise Reduction Coefficient (Defined in Section 4.7.2)
Nu	Nusselt Number (Defined in Eq. 2.7)
P	Pressure [Nmm^{-2}]
P_{PORE}	Number of points located in the pores
Q	Heat Flow [Wm^2]
Q_V	Volumetric Flow Rate [m^3s^{-1}]
R	Resistivity [Ω]
Re	Reynolds Number (Defined in Eq. 5.1)
S_V	Specific Surface Area [mm^{-1}]
T	Temperature [°C, K]

V_D Darcian Velocity [ms^{-1}]

V Volume [m^3]

W Weight [kg]

a Sabine Absorption Coefficient

c Speed of Sound [$331ms^{-1}$]

d Thickness [m]

f Frequency [Hz]

h Convection Heat Transfer Coefficient [$Wm^{-2}K^{-1}$]

l length [m]

m Mass Flow Rate [kgs^{-1}]

n Critical Exponent

q Heat Transfer Rate [W]

r Sound Reflection Factor [Defined in Eq. 3.15]

Greek Symbols

Δ Difference

α Acoustic Absorption Coefficient (Defined in Eq. 3.16)

ε Porosity [%]

λ Thermal Conductivity [$Wm^{-1}K^{-1}$]

μ Dynamic Viscosity [$kgm^{-1}s^{-1}$]

ν Kinematic Viscosity [m^2s^{-1}]

ρ Density [kgm^{-3}]

σ Electrical Conductivity [Sm^{-1}]

Subscripts

C	Convection
CH	Chamber
CON	Interfacial Area
Cu	Copper
eff	Effective
f	Fluid
hyd	Hydraulic
G	Gas
i	Imaginary
IN	Inlet
K_2CO_3	Potassium Carbonate
L	Line
OUT	Outlet
p	Particle
V	Volume
r	Real
R	Radiation
S	Solid
TOT	Total

Chapter 1

INTRODUCTION

1.1 Motivation behind the research

Over the last few decades, cellular metallic foams, or porous metals have been receiving a large amount of interest in industry due to the rapidly growing advancement in manufacturing techniques, design and possible applications. Their unique properties and multi-functionality allow them to be utilized in many different uses throughout different industrial sectors. There is a huge range of porous metals that can be produced with different metals, alloys and cellular structures giving a combination of different properties. Industrial interests include impact energy absorption, thermal management properties, acoustic properties and electrical properties. Some typical existing applications are lightweight panels for building and transport, impact absorption panels, thermal and sound insulation, heat exchangers, structural parts for aircraft, heat shielding, electromagnetic shielding, loudspeaker enclosures, heat sinks, filters and condensing towers. Porous metals are still in the relatively early stages of development and the potential for more and more applications is expanding rapidly. The development of low-cost production methods will make many types of porous metals a cheap alternative to expensive, existing engineering materials.

A novel technique used to produce porous metals with unique physical properties was developed by Zhao *et al* (2005). This is known as the Lost Carbonate Sintering (LCS) process and involves sintering metal powder particles around potassium carbonate particles. It is a highly controllable process, which can be adjusted to produce porous metals of known porosities, pore sizes and pore shapes.

The thermal and acoustic properties of porous copper, manufactured by the LCS method, are of particular interest. The prominent thermal properties of copper in its solid form, combined with the unusual pore morphology and topography resulting from the LCS process, give rise to some fascinating and unconventional thermal characteristics.

Similarly, the unconventional microstructure of LCS porous copper makes it an ideal candidate for use as an acoustic absorber in harsh environments. Historically, acoustic absorbers are purpose built to be used solely as absorbers. The combination of a rigid construction, acoustic properties and relative light weight of LCS porous copper would allow it to be used in a wide range of engineering applications where conventional absorbers are not suitable.

1.2 Objectives

The primary objectives of this thesis are to investigate the thermal transport, fluid permeability and acoustic absorption characteristics of LCS porous copper samples with different structural properties. The mechanisms involved in these processes will be analysed, with an aim to identify the optimum structural properties to give rise to the best thermal or acoustic performance.

1.3 Thesis Structure

A total of six chapters are included in this thesis. Chapter 2 evaluates the literature that is relevant to the work presented. The methods currently used to manufacture porous metals and the techniques used to characterize the microstructural and physical properties, including pore parameters, electrical conductivity, thermal conductivity, fluid permeability, heat transfer and acoustic absorption, will be reviewed. An overview of existing porous metals and their properties will also be given in this chapter.

Chapter 3 gives a detailed explanation of each of the different experimental procedures used in this work, including the LCS method used to produce the porous copper test samples, the characterization techniques for structural analysis, and the measurements in thermal and electrical conductivity, acoustic absorption coefficient, permeability and heat transfer. The equipment and process conditions used in the experiments are described.

Chapter 4 presents the results taken from each of the experimental procedures, in graphical and tabulated form. The microstructure of LCS porous copper is described, with particular attention being paid to porosity, pore size and specific surface area. The effect of structural and experimental parameters on thermal conductivity, electrical conductivity, permeability, heat transfer and acoustic absorption are described in detail.

Chapter 5 includes a detailed analysis of the results obtained in Chapter 4, paying particular attention to the correlation between the physical properties and the structural characteristics of the test samples. Performance comparisons with similar existing materials within each experimental area are also made.

Chapter 6 summarises the conclusions drawn from this study and possible areas of future work.

Chapter 2

LITERATURE REVIEW

2.1 Introduction to Porous Metals

Porous metals, or metallic foams can be defined as a metallic bulk material with a dispersion of gaseous bubbles or voids inside. The porosity contained within the metallic structure results in the porous metal possessing a lower density than that of the bulk material. This relatively low density combined with the physical properties of the metal results in a number of unique and fascinating properties. A large number of metallic materials are available for the manufacture of porous metals, such as copper, steel, aluminium, magnesium, lead, zinc, bronze, titanium, gold, graphite and various alloys. Porous metals can have either closed or open pores, depending on the connectivity of the cells. In most cases, porous metals with open pores have a greater number of functional uses and therefore possess a greater number of potential applications.

Porous metals have received a growing interest in both industry and academia in recent years due to their unique physical and structural properties (Gibson and Ashby 1997, Ashby *et al* 2000, Banhart 2001, Banhart *et al* 2003). Their cellular metal structure means that they possess unique combinations of properties. These include: impact energy absorption capacity, air and water permeability, atypical acoustic properties, heat exchanging capabilities and good electrical

insulating properties. The drive in academia to develop new, unique engineering materials has contributed to the advancement of porous metals throughout a large number of industrial sectors. Porous metals are still in the early stages of development and so the potential for more applications is still expanding rapidly. For both structural and functional applications, the most important considerations are bulk materials selection, pore characteristics and cost.

There are a number of methods available to produce porous metals (Gardner 1967, Ashby *et al* 2000, Banhart *et al* 2003, Gibson *et al* 1997). Early methods of manufacture concentrated mainly on casting and foaming techniques. Powder metallurgy manufacturing methods have received a great deal of interest in academia in recent years, but not so much in industry due to the high costs involved in producing metal powders. Powder metallurgy manufacturing methods include slurry foaming, loose powder sintering, fibre metallurgy, sintering slurry saturated foam (Davies and Zhen 1983), and space holder methods.

2.2 Production Methods and Techniques

Recent industrial and academic interest in porous metals has given rise to a large number of production methods being developed. This section briefly describes the common techniques involved in these manufacturing processes.

2.2.1 Foaming in Melts

It is possible to foam metallic melts directly under certain conditions by injecting gases (air, nitrogen, argon) into the liquid metal (Banhart *et al* 2003). The gas is injected using specially designed, rotating impellers. When the gas is injected, the bubbles have a tendency to rise to the surface of the melt. This effect can be reduced by increasing the viscosity of the molten metal by adding ceramic powders or alloying elements. The result is a more even pore distribution in the manufactured foam.

In 1951, Elliot successfully produced foamed aluminium (Elliott 1956). This method involved adding a blowing agent to a molten metal. The mixture is heated, causing the blowing agent to decompose and evolve gas. This gas then expands, resulting in a foaming of the molten metal. After cooling, a solid cellular structure remains. Aluminium is typically used as the metal, with the blowing agents being a metal hydride such as TiH_2 or ZrH_2, although other combinations can be used. The main disadvantage of this manufacturing method was that the pore size and distribution could not be accurately controlled, usually resulting in a larger pore density at the centre of the sample.

One approach used to overcome these problems was using high speed mixing to disperse the blowing agent throughout the molten metal in a very short space of time. This resulted in a more uniform pore distribution throughout the structure (Davies and Zhen 1983). Figure 2.1 shows the pore structure of a metallic foam

manufactured by adding a foaming agent into an aluminium melt (trade name ALPORAS™).

Another improvement to the process was increasing the viscosity of the molten metal by using specific alloys as the bulk material (Davies and Zhen 1983). This aids in preventing the escape of gas bubbles. Thickening the melt enables it to maintain its fluid state for longer periods of time, without collapsing. This gives more time for the foaming agent to be added to the melt. Specific agents, such as air, oxygen, nitrogen, carbon dioxide, argon and water can also be employed to increase the viscosity of a particular molten metal. When these agents are added, the viscosity of the melt increases, resulting in a smaller pore size and a more even pore distribution.

2.2.2 Casting around Granules

This process involves the casting of a particular molten metal around granules, within a casting mould. These granules can be soluble, so that they can be dissolved and leached out after the casting process, leaving a cellular metal structure. A popular material used for the granules is sodium chloride (Kuchek 1966). The granules used can also be in the form of compressible hollow glass or corundum spheres (Davies and Zhen 1983). If this is the case, dissolution of the granules is not required after the casting process. The main disadvantage with this process is that it is difficult to get the molten metal to flow into and around the interstices between granules. One way of overcoming this problem is introducing a vacuum environment in the casting process.

As well as casting the molten metal around the granules, the granules can also be introduced into the molten metal (Banhart *et al* 2003). In this case, the metal is heated in a crucible until molten, at which point the granules are added. Once added, the mixture is mixed vigorously to disperse the granules until the metal mass is sufficiently cooled.

2.2.3 Investment Casting

Investment casting is a unique method of producing metallic foams. This process involves filling the pores of a foamed plastic with a fluid refractory material. This is then hardened and the plastic refractory material is heated until the plastic component is vaporized, leaving a porous mould. A molten metal is then poured into the mould and allowed to cool. Once solidified, the refractory is removed and a metal foam of the same configuration of the foamed plastic remains. In general, only metals with a low melting point can be used as the base material for these foams. These metals include copper, aluminium, lead, zinc, tin and a number of different alloys (Davies and Zhen 1983). An SEM image of a commercially available metallic foam sold by ERG in California under the trade name DUOCEL^{TM} is shown in Figure 2.2.

2.2.4 Metallic Deposition

Metallic foams with high porosities and uniform pore distribution can be manufactured using the metallic deposition method. This process entails applying a metallic cover to a structure of polyurethane strands. It consists of

three basic stages: rigidization, electroless pre-plating and electroplating (Cohen *et al* 1968). The polyurethane structure used is flexible and so the strands must be made more rigid in order to prevent deformation of the metal foam, after the deposition takes place. The rigidization process applies a coating of epoxy to the polyurethane strands to increase their rigidity and eliminate distortion of the resulting metal structure. The polyurethane strands are then treated with an acidic solution, such as a chromic/sulphuric/phosphoric mixture. This process etches the strands, resulting in a micro-roughened surface, which promotes adhesion of the deposited metal layers. The strands are made conductive by the deposition of an electroless thin metal film. This involves immersing the structure in an electroless solution (Carter 1977, Gabe 1972). Metals used for the pre-plating process include copper, nickel, iron, cobalt, silver and gold. Finally, the polyurethane strands are electroplated to the required thickness, depending on the required relative density of the foam. The polyurethane substrate can then be decomposed through heating. Metals that have been used for the electroplating process include copper, zinc, nickel and silver.

2.2.5 Slurry Foaming

This manufacturing process employs powder metallurgy techniques, rather than casting or metallic deposition. It involves mixing a metal powder with a foaming agent to produce a slurry (Drolet 1977). The slurry is whipped into a foam and fired at an elevated temperature to form a porous metal structure. Some common metal powders that have been used in this process are copper, iron, nickel, stainless steel and bronze. Aluminium foams have been used in the slurry

foaming technique, but it has a relatively low strength and therefore can only be used in limited applications (Drolet 1977). The slurry used to produce aluminium foams in this manner consists of aluminium powder and a blowing agent, such as orthophosphoric acid, aluminium hydroxide, or hydrochloric acid. After mixing the slurry, the mixture is poured into the required mould and left to cure at a temperature of 100°C for approximately two hours, which enhances the resulting solid foams mechanical properties.

2.2.6 Loose Powder Sintering

Sintering can be described as the particle coalescence of a powdered aggregate by diffusion that is accomplished by firing at an elevated temperature (Callister 2000). Figure 2.3 illustrates the sintering process. When metal powder particles are in contact with each other (i.e. after pressing), necks form along the contact surfaces of adjacent particles when the sintering temperature for the metal is achieved (Figure 2.3(a-b)). A grain boundary develops on each neck and the void between the particles develops into a pore. At the advanced stages of sintering, the necks increase in size resulting in a reduction in the pore size (Figure 2.3(c)). Mass movements that occur during sintering consist of the reduction of total porosity by repacking, followed by material transport due to evaporation and condensation from atomic diffusion. In the final stages, metal atoms move along crystal boundaries to the walls of internal pores, redistributing mass from the internal bulk of the object and smoothing pore walls. Surface tension is the driving force for this movement.

Although the metal powder can be pressed within a preform prior to sintering, the application of pressure is not critical to the process. The advantage of this is that a metal powder can be used to fill a mould of any shape or size and then be sintered. This makes the process an ideal candidate for the production of complex porous metal structures. The porosities of porous metals produced using this method are relatively low (usually between 40% and 60%). For higher porosities using this method, a spacing agent can be added to the powder before sintering. This agent can then be either decomposed or evaporated during sintering, or removed via dissolution afterwards (Fedorchenko 1979). The sintering and dissolution process (Zhao and Sun 2001) and the LCS process (Zhao *et al* 2005) are two examples of the space holder methods. The loose powder sintering technique is generally used in applications where a high porosity and relatively low pore size are not required.

Of all the manufacturing methods available for producing porous metals, sintering methods are the most promising, capable of economically producing millions of components annually (Haack *et al* 2001).

2.2.7 Sintering a Slurry Saturated Sponge

When powder metallurgy is used to manufacture porous metals with higher porosities, a support structure can be introduced to the sintering process (Arrance 1966, Tracey 1976). A slurry is formed by mixing the desired metal powder with water or another organic liquid. The sponge is then saturated with the slurry and allowed to dry. The water or organic liquid acts as a vehicle to carry the metal

powder so that it is able to penetrate the pores of the sponge. Once dry, the saturated sponge is heated to a temperature that is sufficient to decompose the sponge structure. With the sponge decomposed, the metal powder is heated to its required sintering temperature. After cooling, a high porosity porous metal remains.

2.2.8 Fibre Metallurgy

As well as metal powders, metal fibres can also be sintered resulting in porous metals with some unique properties. A major advantage of this manufacturing process is that the resulting porosity is highly controllable up to approximately 95%. Resulting structures care able to be manufactured in the form of sheets, plates, tubes and cylinders, with applications including gas filtration, catalyst substrates and noise attenuation. Various mechanical methods are used to produce the fibres, such as machining or drawing (Yarnton 1966). The fibres are then sintered using conventional techniques. Following sintering, the metal fibres retain their strength, resulting in a porous metal, which offers good constructional properties. Additionally, the pore structure is such that high permeability can be achieved. This high permeability makes porous metals manufactured using this technique, ideal candidates for use as filters. Metals used in this process include copper, stainless steel, nickel and Ni-Cr alloy (Xie *et al* 1966).

2.2.9 Sputter Deposition

A novel method for manufacturing closed-cell metal foams has been developed in the USA (Sosnik 1948). The process involves sputtering a metal under the pressure of inert gas, onto a substrate, leaving a metal body with atoms of entrapped inert gas distributed throughout. This is then heated to a temperature above the melting point of the metal for a set period of time, allowing the entrapped gas to expand and form individual closed cells. The metal body is cooled, resulting in a porous structure, with evenly distributed closed-pores containing inert gas. The amount of gas contained within the body can be controlled by varying the pressure of the inert gas within the deposition chamber and can vary between 15 and 2300ppm. Porosities can range extensively from several percent up to approximately 80% (Davies and Zhen 1983).

2.3 Structural and Mechanical Characteristics of Porous Metals

The mechanical properties of a porous metal are largely dependent on the base metal and the density, but the pore topology and structure also have an effect. When compared to the base metal, the mechanical properties of a porous metal are generally considered poor. For example, foamed tungsten, with a relative density of 0.3 only exhibits tensile and compressive strengths of 4 to 5% those of the base metal (Gardner 1967). However, when compared to other non-metallic materials of equal density, the mechanical properties are superior. The mechanical properties of any porous metal depend upon the composition of the matrix material and the manufacturing method employed.

The microstructure of a foam sample, showing individual pores and cell walls can be seen in Figure 2.4. This particular foam is aluminium and has been produced using the Sintering and Dissolution process (SDP) (Zhao and Sun 2001). This manufacturing method involves the sintering of a compressed metal powder around sodium chloride granules. They found the SDP process to be a cheap, effective method of producing aluminium foams with accurately controlled pore size, porosity, pore distribution and pore morphology. In this particular metal foam, the internal surfaces of the pore walls are rough and dispersed with a large number of micro pores or interstices. These form small channels between different pores. This large number of internal channels means that the foam has an extremely large surface area. In contrast, metallic foam produced using a melt infiltration method has smoother pore walls with no interstices between the pores. This gives the melt infiltration foams better mechanical characteristics while the SDP metal foam gives improved damping and energy absorption properties.

Figure 2.5 shows the compressive stress-strain curves of a set of porous aluminium samples manufactured by the same SDP method. Each sample has different aluminium fractions, ranging from 0.2 to 0.6. The compression tests of the specimens were conducted on an Instron4505 materials testing system at a crosshead speed of 1 mm/min. The stress-strain curves are distinguished by an elastic response, a smooth, positive plateau slope and finally a transition to densification. Increasing the relative density of the foam increased the macroscopic yield point and plateau stress at a particular strain. All the curves show a smooth plateau region as a result of uniformly distributed pores within a

controlled and narrow size range. If a foaming production method were used to make the foam, the pores would be randomly sized with a completely random distribution. This would give a sharper plateau region in the curves. As might be expected, the higher the percentage of aluminium within the foam, the higher the stress for a given strain. An important factor determining the mechanical properties of the aluminium foams were the sintering conditions. Sintering times shorter than 120 minutes resulted in poor bonding between particles, while sintering times longer than 360 minutes led to considerable oxidation of the structural surfaces. The optimum sintering temperature was judged to be in the range of 640 – 700°C. At temperatures below 640°C, poor bonding ensued, while temperatures above 700°C led to an increase in flowability of the molten aluminium, resulting in a partial separation of the Al/NaCl particles. This caused inadequate uniformity of localised relative density throughout the foam.

In general, the relative density of a porous metal and the compressive strength show a high correlation. Tao *et al* (2007) examined the mechanical response of a sintered porous copper under three-point bending and Charpy impact conditions. The porous copper was manufactured using the Lost Carbonate Sintering method developed by Zhao *et al* (2005). An Instron 4200 mechanical tester at a crosshead speed of 1mm/min was used to carry out the three-point bending tests, while the Charpy impact tests were carried out on a Zwick impact machine. They found that the apparent modulus, flexural strength and energy absorption capacity increased exponentially with increasing relative density. It was also found that the impact strength was significantly higher than the bending energy absorption capacity. Increasing the compaction pressure at the manufacturing

stage increased both the flexural strength and the bending energy absorption capacity. When the compaction pressure was increased from 140 to 210MPa, the flexural strength increased from 1.8 to 3.9MPa and the energy absorption doubled from 0.5 to 1.0 KJ/m^2. Increasing the compaction pressure enhanced the contact surface area between copper particles, resulting in larger neck growth and better bonding upon sintering. The authors also discovered that the flexural strength and bending energy absorption capacity could also be significantly improved, by increasing the pore size. When the pore size was increased at a given porosity, the interstices between the K_2CO_3 particles increased in size due to a reduction in pore density. These larger, thicker interstices were able to be filled with larger amounts of copper powder, resulting in stronger, more integral cell walls after sintering.

Zhang and Wang (2004) used a space holder method to manufacture a series of sintered porous coppers with low to medium porosities in the range of 20 to 50%. The compressive properties were investigated experimentally and the modulus was found to decrease with decreasing porosity. The yield strength showed a linear relationship with porosity. A displacement controlled uniaxial compression was employed as the deformation mechanism. They found that under quasi-static conditions, deformation occurred homogeneously throughout the structure, exhibiting more solid-like properties than a foam material. Similarly, Hyun and Nakajima (2002) found that the compressive yield strength of a porous copper produced by unidirectional solidification decreased linearly with increasing porosity, when the cylindrical pores were parallel to the direction of compression. When the pores were perpendicular to the direction of

compression, a different stress-strain curve was observed. This was due to the stress concentration around the pores and the buckling of the copper under stress in the pore walls.

Although the relative density, or porosity is the dominating influence over the mechanical behaviour of porous metals (Ashby 1983), other structural parameters, such as pore size and pore distribution should also have an effect if the relative density remains constant (Fazekas *et al* 2002). Han *et al* (2003) studied the effect of pore size and pore combination on the mechanical behaviour of an open cell aluminium foam, manufactured using an infiltration method. The authors found that the mechanical response could be improved, by introducing smaller pores into nodes of the pore walls. A combination of large pores with relatively small pores resulted in a higher specific yield strength and elastic modulus. A simulation using finite element (FE) analysis to examine the stress distribution and failure mode was carried out, so that the deformation mechanisms could be analysed. Significant stress concentration was observed at weak locations in the pore walls when no small pores were introduced in the nodes. When small pores were present within the pore walls, the concentrated stress moved to the nodal areas between the large and small pores, reducing the premature failure at the original stress-concentrated areas. These changes in stress distributions and deformation modes accounted for the increased elastic modulus and yield strength, when a combination of large and small pores was introduced, when compared to samples with a uniform pore size.

Processing conditions play an important role in the mechanical response of a porous metal. Different manufacturing processes and process conditions result in differences in pore structure and topology. Sun and Zhao (2003) examined the effects of processing conditions on the static and dynamic energy absorption of porous aluminium. The test specimens were manufactured using the SDP method (Zhao and Sun 2001). They found that for solid-state sintering, higher sintering temperatures resulted in better bonding between particles. This gave rise to improved energy absorption. At a given temperature, an optimum sintering time existed. When the sintering temperature or the relative density decreased, the optimum sintering time increased. The optimum pore sizes for static and dynamic energy absorption were 1200 to 1500μm and 710 to 800μm respectively. The energy absorption in static conditions was found to be significantly larger than that under dynamic conditions.

As well as manufacturing methods and process conditions, mechanical properties of porous metals can be altered using traditional methods. There are a number of different alloy porous metals available, which all show unique mechanical characteristics. As with solid materials, the foam can be heat-treated. It is also possible to increase the strength by adding reinforcing fibres to porous metals (Bjorksten and Rock 1972, Niebylski 1974). The mechanical strength of reinforced aluminium foam using this strengthening method is significantly larger than conventional aluminium foams.

2.4 Electrical Conductivity

If an electrical potential difference is placed across a conductor, positively charged particles will flow in the field direction and negatively charged particles will flow in the opposite direction. The electric current is a result of the flow of electrons and this is termed the electronic conduction. The electrical conductivity can be defined as the ability of a material to conduct an electric current (Callister 2000). It can be expressed as the ratio between the current density, or current per unit area of the conductor, J, and the electric field intensity, E (Eq. 2.1), or the voltage difference across the conductor divided by the distance separating them.

$$J = \sigma E \tag{2.1}$$

where the electrical conductivity, σ, is measured in Siemens per meter (Sm^{-1}).

Electrical conductivity can also be expressed as the reciprocal of the resistivity, ρ. Resistivity is a measure of a material's ability to oppose the flow of an electric current and is measured in ohm meters (Ω-m). The resistivity of a material can be expressed as:

$$\rho = \frac{RA}{l} \tag{2.2}$$

where R is the electrical resistance of the material through which the current is passing, A is the cross-sectional area of the conductor perpendicular to the

direction of current flow and l is the distance between the two points on the conductor at which a voltage is applied.

In metals, the charges that are responsible for current are free electrons. These electrons are not bound to any particular atom and therefore able to move freely in the field. Although the number of free electrons does not vary with temperature, an increase in temperature decreases electrical conductivity. The reason for this is that the number of imperfections in the atomic lattice structure increases with temperature and this hampers electron movement. These imperfections include dislocations, vacancies, interstitial defects and impurity atoms. Additionally, above absolute zero, even the lattice atoms participate in the interference of directional electron movement, as they are not always found at their ideal lattice sites. Thermal energy causes the atoms to vibrate about their equilibrium positions. At any moment in time many individual lattice atoms will be away from their perfect lattice sites and this interferes with electron movement.

In a porous metal, the mechanisms behind electrical conductivity indicate that conduction will only be possible via the solid phase in the pore structure.

Ma *et al* (2005) measured the electrical conductivity of an open-celled aluminium foam. The foam samples tested were manufactured using the SDP method developed by Zhao and Sun (2001). Eddy current techniques were used to measure the electrical conductivity of nine test samples, with porosities ranging between 63.1 and 83.4%. Pore sizes were split into four categories: 425 –

710μm, 710 – 1000μm, 1000 – 2000μm and >2000μm. They concluded that the electrical conductivity of the foam samples was strongly dependant on both the porosity and the pore size. Test samples with higher porosities displayed lower values of electrical conductivity due to the decreased volume ratio of the metal matrix in the foams. At a fixed porosity, a larger pore size resulted in a higher electrical conductivity due to the better-bonded network within the microstructure. Finite element simulations were also carried out on the foam samples. The simulations involved calculating the mutual impedance between two coils to solve the forward electromagnetic induction problem. The resulting calibration curve obtained from the simulation was used to relate the mutual impedance change with the electrical conductivity of the samples. The finite element simulations were found to be in good agreement with the experimental results obtained from the investigation.

Feng *et al* (2002) examined the effect of relative density and pore size on the electrical conductivity of a series of closed-cell aluminium alloy foams. The test samples were manufactured by mixing metal powders and a foaming agent, and compacting them into a foamable precursor material, expanded by heating it up above its melting point. The resulting foam samples displayed relatively uniform structures, with relative densities ranging from 0.129 to 0.313 and mean pore diameters varying between 1.7mm and 3.6mm. They found that the power law function could be applied to describe the dependence of electrical conductivity of the foams on the relative density. They concluded that pore size had a negligible effect on the electrical conductivity.

2.5 Thermal Conductivity

Thermal conduction is the phenomenon by which thermal energy is transported from a region of higher temperature to a region of lower temperature within a substance. The ability of a particular substance to conduct heat is characterized by its thermal conductivity. In steady-state conditions, where the heat flow is constant, the thermal conductivity can be described by:

$$Q = -\lambda \frac{dT}{dx} \tag{2.3}$$

where Q is the heat flow or heat flux per unit time per unit area (Wm^{-2}), λ is the thermal conductivity ($Wm^{-1}K^{-1}$) and dT/dx is the temperature gradient through the medium conducting heat. The area involved is taken to be perpendicular to the direction of heat flow (Callister 2000).

2.5.1 Mechanisms of Thermal Conduction

In solid media, heat is conducted through lattice vibration waves and free electrons. The sum of these two contributions represents the total thermal conductivity of the solid medium. Conduction through lattice vibration waves occurs when adjacent atoms vibrate against one another. The thermal energy is transported in the direction of motion of the lattice waves, or phonons. When free electrons within a substance are heated, their kinetic energy increases. These electrons then migrate to cooler areas within the substance, where some of this energy is transferred through vibrations to other atoms. The vibrational energy occurs as a result of the electrons colliding with phonons within the

substance. Thermal conduction in solids is greater than in liquids or gasses as a result of atoms being in constant proximity with each other. It can generally be said that as the density of a material decreases, so does its thermal conductivity. In gases, the distance between adjacent atoms is greater than in solids or liquids, resulting in fewer collisions between atoms. The consequence of this is a relatively low thermal conductivity. In metals, thermal conduction is generally superior to non-metallic substances. Heat conduction via electron movement is prevalent in metals due to their crystalline structure and metallic bonding.

2.5.2 Thermal Conduction in Porous Metals

The thermal conductivity of a porous metal will be less than that of the bulk material. The effective thermal conductivity of a porous metal can have four contributions (Gibson and Ashby 1988). In addition to conduction through the solid phase, conduction via the gas phase within the pores, convection and radiation will also contribute to the total thermal conduction. This can be summed up by:

$$\lambda = \lambda_S + \lambda_G + \lambda_C + \lambda_R \tag{2.4}$$

where λ is the total thermal conduction, and λ_S, λ_G, λ_C and λ_R represent the thermal conductivity contributions through solid conduction, gaseous conduction, convection and radiation respectively. Impurities and metal oxides contained within porous metals may also contribute to the total thermal conductivity

(Degischer and Kriszt 2002). In most cases, the gas contained within the pores will be air. The thermal conductivity of air at atmospheric pressure is 0.025 $Wm^{-1}K^{-1}$ (Jackson and Leach 1993). The low thermal conductivity of air means that the contribution of the thermal conduction from the gas phase, λ_G, is negligible when compared to that in the solid phase, λ_S. The effects of convection within the pores are only important when the Grashof number (ratio between the force driving convection and the viscous force opposing it) is greater than approximately 1000. This value is achieved when the pore size exceeds 10mm in diameter (Gibson and Ashby 1988). For pore sizes smaller than this, thermal conduction through convection, λ_C, can be ignored. In the case of optical non-transparent metals, radiation through the pore walls is not possible. When the thermal conduction in the solid phase of the porous metal is greater than 20 $Wm^{-1}k^{-1}$, the contribution of radiation, λ_R, can be ignored (Lu and Chen 1999).

Extensive experimental and analytical research has been carried out on heat transfer in porous media. A comprehensive review of heat transfer in general porous media has been carried out by Kaviany (1995). Heat transfer in polymeric foams has been examined by Glicksman *et al* (1994), while Lee and Cunnington (2000) have investigated conduction and radiation heat transfer in high porosity fibre insulation. The thermal transport processes in closed-cell aluminium alloys were observed in a study carried out by Lu and Chen (1999). The apparent thermal conductivities of two-dimensional foams possessing different microstructures were calculated. The microstructures considered included regular honeycombs and randomly distributed pores created in manufacturing processes such as foaming, where a supersaturated gas is made to separate from

the molten metal, creating a random distribution of bubble nucleation. These randomly distributed pore structures were represented using Voronoi structures and Johnson-Mehl models. The affects of geometric imperfections within the pore structure, such as pore edge misalignments, fractured pore edges, pore size variation and missing pores were studied using these analytical techniques as well as finite element methods. This study neglected the effects of conduction through the gas phase and convection, focusing on solid conduction and thermal radiation. They concluded that the transport of heat is dominated by solid conduction along the cell walls, with the effect of thermal radiation being negligible, even at elevated temperatures of approximately 600°C. The thermal conduction was dependent upon the pore shape, connectivity and topology, with conduction decreasing when imperfections in the pore structure were present. They found that solid inclusions also caused a decrease in the thermal conductivity.

The computational aspects of effective thermal conductivity of highly porous metal foams were considered by Singh and Kasana (2004). Their study was based on numerical simulations, using a resistor model to estimate the effective thermal conductivity of both the solid and gas phases within porous metals. The model considered a two-phase medium where the matrix consisted of layers oriented parallel and perpendicular to the direction of heat flow, representing the pore walls. A weighted arithmetic mean represented the parallel layers, while the perpendicular layers were represented by a weighted harmonic mean. These were the upper and lower bounds of the effective thermal conductivity in a two-phase medium. The study introduced a correlation term, f, to take into account the solid conducting phase, non-linear flow of heat flux lines and the random

distribution of the phases. They found that as well as porosity and the ratio of thermal conductivity of the constituent phases, *f* was also dependant on the pore shape and sphericity of the particles.

Ogushi *et al* (2004) carried out an analytical and experimental investigation on the effective thermal conductivities of lotus-type porous copper. The structure of this porous medium contains straight, cylindrical pores, formed as a result of the precipitation of supersaturated gas dissolved within a copper melt during solidification. The lotus copper showed anisotropy of the effective thermal conductivity. The effective thermal conductivity perpendicular to the pores was found to be lower than that parallel to the pores. They found that for a relative density of 0.4, the effective thermal conductivity along the pores was 40% that of the solid lotus copper bulk material (Ogushi *et al* 2004). Abramenko *et al* (1999) determined the thermal conductivity of an aluminium foam that was produced by mixing aluminium powder with a foaming agent. They found that for a porosity of 69%, the thermal conductivity was just 6.8 $Wm^{-1}K^{-1}$ compared to 247 $Wm^{-1}K^{-1}$ for solid aluminium.

Thermal conduction through a solid medium increases with increasing temperature. This is a result of free electrons gaining more momentum. If the thermal conductivity of a bulk material increases with temperature, the same behaviour is expected of a porous metal. Zhou *et al* (2003) analysed the temperature dependence of effective thermal conductivity of open-celled steel alloy foams. The sintered alloy foams were highly porous with two relative densities of 0.05 and 0.1 tested. The pores per inch varied between 30 and 90.

The thermal conductivities of the samples were measured experimentally using a guarded-hot-plate apparatus, in both atmospheric and under vacuum conditions. The results showed that the effective thermal conductivity increased significantly as the temperature increased. They found that at 800K, the effective thermal conductivity could be three times greater than at 300K. At higher temperatures (500 – 800K), the transport of heat was dominated by thermal radiation. When tested in a vacuum, the effective thermal conductivity increased with pore size and decreased with porosity. The effective thermal conductivity at ambient pressure was found to be twice the value as that in a vacuum. The results showed that natural convection within the alloy foams was strongly dependant on porosity. This was attributed to varying temperature distributions along the vertical cross sections as a result of differing relative densities. Baillis *et al* (2000) modelled heat transfer in open cell carbon foams. They found that at temperatures exceeding 1000K, radiation is the primary source of heat transfer.

Calmidi and Mahajan (1999) modelled the thermal conductivity of aluminium foams at temperatures up to 75°C. They considered a one-dimensional heat conduction model where the porous structure consisted of a two-dimensional array of hexagonal cells, with a square 'blob' of metal at the intersection of two sides of a hexagon. It was found that under these experimental conditions, heat transfer was dominated by conduction through the solid phase, with the effects of convection and radiation being negligible. The square intersections in the hexagonal array meant that the model only had a two-fold rotational symmetry. A development on the model proposed by Calmidi and Mahajan was projected by Bhattachrya *et al* (1999). The model again consisted of a two-dimensional array

of hexagonal cells, with metal fibres making up the hexagonal sides. This model consisted of circular intersections, which are more representative of a physical porous matrix when compared to the square intersections applied in the model developed by Calmidi and Mahajan. They found that the effective thermal conductivity was largely dependent on porosity and pore geometry, while pore density had little effect. These analytical predictions were in good agreement with experimental data using aluminium and reticulated vitreous carbon (RVC) foams.

2.6 Heat Exchange

2.6.1 Introduction

The thermal diffusivity of a material can be defined as the ratio of thermal conductivity to the volumetric specific heat capacity:

$$\alpha = \frac{\lambda}{\rho C_P} \tag{2.5}$$

where α is the thermal diffusivity (m^2s^{-1}), λ is the thermal conductivity ($Wm^{-1}K^{-1}$), ρ is the density of the material (kg m^{-3}) and C_P is the specific heat capacity of the material (J kg^{-1} K^{-1}).

Substances with low specific heat capacities such as metals require less energy to increase their bulk temperature. The specific heat capacity can also be interpreted as a measure of how well a material preserves its bulk temperature

and controls the time in which it takes for the material to achieve a steady-state temperature. A porous metal has a low specific heat capacity when compared to that of the base metal from which it's made due to the volume fraction of gas within it.

Thermal diffusivity governs the heat flow through a substance prior to a steady-state being achieved. Porous metals possess higher thermal diffusivity as a result of their low density, when compared to the bulk material from which it is composed. This allows them to achieve a steady-state heat flow in less time than the bulk material. This makes porous metals promising materials for heat transfer applications, or heat exchangers.

The emissivity of a material is a measure of its ability to radiate absorbed energy. The large surface area of porous metals gives rise to a higher emissivity to that of the metal from which it is made. The low specific heat capacity per unit volume of a porous metal, combined with its high emissivity can be exploited in applications where a fast rate of heating or cooling by radiation is required (Degischer and Kriszt 2002).

Open pore porous metals are well suited to heat exchanging applications where efficient heat dissipation is required. This is due to a high specific solid-fluid interface surface area, a good thermally conducting solid matrix and a tortuous internal network of pores which promote turbulence and mixing of the coolant (Boomsma *et al* 2003). Good thermally conducting metals can be used to produce the porous matrix, such as aluminium or copper. The mere presence of

these metals in a static fluid can increase the overall effective thermal conductivity of the fluid system significantly (Calmidi and Mahajan 1999). The complete effective thermal conductivity of the solid-fluid system (λ_{eff}) can be described by the porosity of the metal matrix (ε) and the individual thermal conductivities of the solid (λ_s) and fluid (λ_f) phases (Kaviany 1995):

$$\lambda_{eff} = \varepsilon\lambda_f + (1-\varepsilon)\lambda_s \tag{2.6}$$

Calmidi and Mahajan (1999) produced a model to show this increase in the overall effective thermal conductivity of the solid-fluid system. An improvement to this model, based on an idealized 3D unit cell of a porous metal with open pores was developed by Boomsma and Poulikakos (2001).

2.6.2 Heat Transfer Performance

A porous metal can be used as a system to transfer heat from hot to cold media. An effective way of measuring the performance of a heat exchanger is using the Nusselt number, *Nu* (Bejan 1995). This is a dimensionless number, which can be expressed by:

$$Nu = \frac{hD_{hyd}}{k_f} = \frac{q}{A\Delta T}\frac{D_{hyd}}{k_f} \tag{2.7}$$

where h is the convection heat transfer coefficient, which is a measure for the heat transfer between a solid and a liquid, D_{hyd} is the hydraulic diameter of the flow channel, k_f is the thermal conductivity of the coolant flowing through the

porous media, q is the heat transfer rate to the coolant, ΔT is the temperature difference which drives the flow of heat and A is the convection surface. The heat transfer rate, q, can be calculated by an energy balance involving the mass flow rate of the coolant flowing through the porous media:

$$q = mc(\Delta T) \tag{2.8}$$

where m is the mass flow rate of the coolant and c is the specific heat of the coolant.

2.6.3 Porous Metal Heat Exchangers

The main design considerations for porous metal heat exchangers are the thermal conductivity of the metal from which it is made (this is usually copper or aluminium due to their high conductivity values), a low pressure drop of the fluid flowing through the heat exchanger and the generation of a turbulent flow through the porous metal, to maximize heat transfer (Ashby *et al* 2000). Generally, a compromise has to be made on either the heat flux or the pressure drop.

Boomsma *et al* (2003) conducted an in-depth experimental study on the use of metal foams as compact high performance heat exchangers. The open-cell foams were manufactured from 6101-T6 aluminium alloy and compressed by varying degrees. They had porosities between 60.8% and 88.2% and a measured specific surface area in the order of 10,000m^2/m^3. The test samples were tested in a

forced convection arrangement, with water used as the coolant flowing through the samples. The samples were heated externally using cartridge heaters. The heat fluxes measured at the heater-foam interface varied up to 688 kWm^{-2}. This corresponded to Nusselt numbers up to 134 at an interface area of $1600mm^2$. The pumping power versus the thermal resistance was used to compare the samples tested. It was found that the thermal resistance of the foams was up to three times lower than commercially available heat exchangers tested, while still using the same pumping power.

The fluid flow and heat transfer of liquid cooled, open–cell porous copper heat-sinks were investigated experimentally by Zhang *et al* (2005). The aim of the experiment was to assess the performance of the foams for use as heat sinks on flip chip BGA packages. The sample fabrication process involved using a polymer precursor to make a foam frame, which was coated with a copper powder. The frame material was then removed by thermal decomposition. The samples had porosities ranging from 60% to 90%, with pore densities of 60 and 100 pores per inch. A liquid cooling arrangement was used to assess the thermal resistances and pressure drops across the test samples. Deionised water was used as the coolant. The sample with the lowest porosity of 60% was found to have the lowest thermal resistance with the highest pressure drop across it. The samples with higher pore densities possessed slightly lower thermal resistances, with larger pressure drops.

A comparison between metal foam heat exchangers and several commercially available heat exchangers was made by Mahjoob and Vafai (2007). The effects

of porosity, pore size and tortuosity were observed. They deduced that metal foam heat exchangers performed better than the commercially available heat exchangers under identical conditions. This was a direct result of a larger heat transfer surface area. Structural characteristics of the metal foams, such as porosity and pore density controlled the heat transfer process. A higher heat transfer was found at lower pore sizes and porosities. The pressure drop also increased as the pore size and porosity decreased.

2.7 Acoustic Absorption

2.7.1 Absorption of Sound at a Surface

The law of the conservation of energy states that energy can neither be created nor destroyed, but it can be transformed from one form to another. Sound energy is the vibration of air particles and this can be dissipated in the form of heat. When a sound wave travelling through air hits a surface covered with an acoustical material, there is a reflected component that is returned to the air. A result of this is a heat loss in the air, but this is only significant at higher frequencies (Everest 2001). A portion of the sound will penetrate the acoustical material. As the sound wave begins to penetrate, the direction of travel will be refracted due to the difference in densities between the material and air. As the sound wave penetrates the material, friction between the vibrating air particles and the material will cause more energy to be dissipated in the form of heat. Obviously the amount of sound absorbed by a material depends on its structure. Non-porous materials yield slightly due to the fact that they are never perfectly

rigid. When a sound wave hits these materials, the air- flow will cause the structure to vibrate. Porous materials will allow a certain amount of air to penetrate below the surface, generating an effective motion of the surface. The reaction of the surface can be described in terms of its specific surface impedance, which is the ratio between the pressure at the surface and the normal velocity at the surface (Morse 1948). The value can depend on the structure of the absorbing material, the frequency of the incident sound wave and the angle of incidence of the sound wave.

Another measure of a material's acoustic absorption is its absorption coefficient (Morse 1948). The absorption coefficient defines the efficiency in which the surface of a material can absorb sound. If 75% of the energy of an incident sound wave is absorbed, the absorption coefficient of that material is said to be 0.75 (Everest 2001). There are two kinds of absorption coefficient: the Sabine absorption coefficient, a, and the energy absorption coefficient, α. The Sabine absorption coefficient is based on the arithmetic of the absorption at a number of incident surfaces, whereas the energy absorption coefficient is based on the geometric mean reflection. The Sabine absorption coefficient and the energy absorption coefficient are related by:

$$a = -\log(1-\alpha) \tag{2.9}$$

2.7.2 Acoustic Absorption Measurement

There are three methods of measuring the acoustic absorption of materials, namely the reverberation chamber method, the tone-burst method and the impedance tube method.

The reverberation chamber consists of a large room with highly reflective walls, floor and ceiling. The high reflectivity of the internal walls of the chamber gives rise to an extremely long reverberation time. The test procedure involves laying a large sample of the material to be tested on the floor of the chamber. The standard size of the sample used in this test is 2.44 x 2.74m (Everest 2001). The reverberation time is then measured and compared to the reverberation time of the empty chamber. The difference can be attributed to the amount of sound absorbed in the test sample and the absorption coefficient can be calculated.

The tone-burst method can be used to measure the absorption coefficient of a material at any desired angle of incidence (Everest 2001). A sound pulse is fired at the sample surface, from the desired angle and the magnitude of the reflected pulse is measured. The absorption coefficient can be calculated by the difference in intensity between the incident and reflected sound pulses. The system uses short pulses of sound, which make anechoic acoustical measurements possible in ordinary rooms. The short pulses allow the sound waves to be fired and measured before external interference has time to be detected.

The impedance tube, or standing wave tube is a convenient way of measuring the acoustic absorption performance of small sized test samples (Everest 2001). This method is generally used to measure the performance of porous materials. The method employs the same basic theory as with the tone-burst method, in that it measures the difference in intensity between an incident and reflected sound wave. A disadvantage of using this measurement process is that the incident sound source is directed in one direction down the impedance tube to the test sample. The direction of the incident wave is therefore only in one direction, normal to the surface of the absorber. In reality, the source of sound comes from all directions and the absorption of sound waves arriving from different angles of incidence cannot be measured.

2.7.3 Porous Acoustic Absorbers

When a material is porous enough, the air motion normal to the surface is dependant more on the air flow into and out of the pores than the motion of the panel as a whole. When sound enters a porous material, the air flow will cause the interstices within the structure to vibrate. The resulting mechanical movement of the interstices dissipates energy in the form of heat (Pizzirusso 1981). There are several mechanisms which contribute to this energy dissipation: through viscous losses as the sound pressure is pumped in and out of the absorber's cavities, by mechanical damping in the structure of the absorber itself, thermoelastic damping, Helmholtz resonance and by vortex shedding from sharp edges.

The acoustic absorption properties of the porous structure depend on the frequency if the incident wave, flow resistivity, the porosity and the effective air density (Morse 1948). The flow resistivity, r_P, under steady-state conditions can be described by:

$$r_P = \frac{u_x}{d\Delta P} \tag{2.10}$$

where u_x is the flow of air through the pores, ΔP is the pressure drop across the porous material and d is the thickness of the material (Morse 1948).

If the rear face of the absorbing material is placed against an impervious backing, the velocity of the sound wave immediately adjacent to the backing will be zero. A sound wave entering the pores will cause the air pressure inside them to increase. If the pores within the material are small enough, the air within them can lose its heat to the pore walls. It is in this situation that the absorber will be most effective.

When materials are selected specifically for sound absorbing purposes, highly permeable substances are the obvious choice. A highly permeable material will allow the sound wave energy to penetrate the structural cavities, allowing more energy to be dissipated via frictional and viscous losses in the form of heat. Open cell polymer foams and glass or mineral fibre materials are generally used. The disadvantage of using polymer foams is that they are flammable when subjected to high temperatures. Fibrous materials such as flexible polyurethane are generally regarded as excellent acoustic absorbers, but have a tendency to wear

down and erode over time due to air flow and vibration within their structure (Degischer and Kriszt 2002). These are generally used in automobiles, aircraft and industrial applications (Everest 2001).

2.7.4 Acoustic Absorption in Porous Metals

Porous metals combine good mechanical properties with a cellular structure, which make them ideal contenders for acoustic absorption applications, particularly for use in hostile surroundings (Han *et al* 2003). The main parameter for good acoustic absorption properties is the material's permeability. In the case of open-pore porous metals, the air flowing into the absorber is able to penetrate the pores and interstices within the structure, and subsequently the energy can be dissipated by the mechanisms described in 2.7.3.

In most cases, porous metals exhibit greater acoustic absorption characteristics if the pores are open (Davies and Zhen 1983). Porous metals with closed pores are generally considered poor absorbers, owing to the fact that air flow is unable to penetrate the internal pores of the structure. Lu *et al* (1999) conducted a study on a type of closed cell aluminium alloy foam. They concluded that the closed cell foam did not absorb sound well, but the performance of the foams could be enhanced by subjecting the foams to rolling or compression. By doing this, the faces of the cells began to fail and show signs of cracking. This enabled the air flow to penetrate in and out of the cracks and the energy was dissipated more effectively. In addition to rolling and compression, hole drilling can also significantly improve the acoustic absorption performance of closed-cell porous

metals (Kovacik *et al* 1999). By drilling holes in the normal surface of a closed cell porous metal, air is allowed to enter the internal structure of material. The energy can then be dissipated through viscous losses within the pores.

Lu *et al* (2000) also analysed the acoustic absorption in aluminium foams with semi-open pores. The foams were produced using a negative-pressure infiltration, using a preform consisting of water-soluble spherical particles. The acoustic absorption and static flow resistance was measured on a series of six samples to observe the effect of porosity, pore size and pore opening. They found that selected samples exhibit an acoustic absorption coefficient greater than 0.8 at frequencies between 800 and 2000Hz. No correlation between acoustic absorption and pore size or porosity was observed. A relationship was found between the acoustic absorption and the pore opening size, with the absorption coefficient increasing as the opening size decreased.

The acoustic absorption behaviour of a set of open-celled aluminium samples was observed by Han *et al* (2003). The foam samples, manufactured using an infiltration process had pores ranging in size between 0.5mm and 3.5mm. The porosities ranged between 57% and 61%. The samples demonstrated better absorption properties at frequencies over 1000Hz than commercial metal foams currently available. They found that a smaller pore size and increasing foam thickness allowed for improved absorption when no air gap was present between the sample and an impervious backing. At low frequencies, the absorption performance was enhanced by the introduction of an air gap behind the absorber. The predominant sound dissipation mechanisms involved were viscous and

thermal losses with no air gap present and Helmholtz resonant absorption when an air gap was present.

Berg *et al* (2003) measured the acoustic performance of a series of aluminium foams. In this case, a comparison was made between open pore structures and closed pore structures having undergone subsequent pore opening. The open pore foams, with pore sizes between 2mm and 3.5mm exhibited a low air flow resistance, when compared to typical absorber materials such as mineral fibres. The acoustic absorption coefficient did however peak at over 0.8. The acoustic absorption behaviour of the closed pore samples was significantly lower than that of the open pore samples due to the high air flow resistance.

Kovacik *et al* (1999) carried out an experimental study on the noise attenuation of a series of closed-cell aluminium foam. The dissipation mechanisms in the aluminium foam were predominantly due to friction between neighbouring surfaces of the cracks appearing in the structure and the vibration of pore walls. Higher loss factors were achieved in foams of high porosity, with thin pore walls containing a large number of cracks. They found that the addition of non-soluble particles to the porous matrix could significantly improve the absorption properties as a result of the additional interfaces introduced to the structure. This idea was expanded on by Jiejun *et al* (2002) in their research on the acoustic absorption properties of aluminium matrix composite foams, which used SiC particle reinforcement within the composite. They established that the A356/SiC foams revealed better damping and sound absorption qualities than aluminium

foams due to the large amount of Al/SiC interfaces present in the matrix, where the interfaces are beneficial to the absorption of vibration energy.

The acoustic behaviour of melt extracted metal fibres and commercially available metal fibres was investigated experimentally by Albracht and Lotze (1999). The acoustic absorption coefficient was determined over a frequency range of 200Hz to 2000Hz, on both sintered and non-sintered test specimens. They discovered that the sintering process degrades the acoustic absorption capabilities of the metal fibre networks.

An interesting study was carried out by Xie *et al* (2004) on the acoustic absorption of a lotus-type porous copper. The test samples were fabricated by unidirectional solidification of melt dissolving hydrogen in a pressurized hydrogen atmosphere. The samples had porosities ranging between 30% and 62% and pore diameters ranging between 270μm and 867μm. The absorption coefficient was shown to increase with frequency, porosity and specimen thickness, while it decreased with increasing pore diameter. They discovered that as the thickness of the sample increased above 20mm, the pores became more difficult to permeate as the length of elongated pores is limited in this lotus-type porous copper.

As has already been discussed, acoustic absorption in porous metals is dependent on the frictional energy losses occurring within the pore structure. Golovin and Sinning (2004) carried out a study to analyse the internal friction in metallic foams and a series of cellular structures. They studied the mechanical damping

and elastic moduli of the porous metals using the mechanical spectroscopy technique. It was found that density, pore size and shape, chemical composition, pre-deformation, vibration frequency and air pressure all influence the damping of porous metals. They found that different mechanical damping mechanisms are involved within porous metals, including thermoelastic damping in aluminium and zinc foams, reversible dislocation motion in all samples studied, magnetomechanical damping in nickel sponges, micro and macroplastic deformation and crack-induced damping in all the sintered porous metals.

It can generally be said that the acoustic absorption behaviour of a porous metal depends greatly on the manufacturing method and resulting structural characteristics. Open pores allow sound energy to penetrate the cavities within the medium, causing an increase in vibrational energy of the pore walls and nodes. This vibrational energy is then dissipated in the form of heat. Thermoelastic damping, viscous and frictional losses are generally considered to be the dominant acoustic absorption mechanisms within porous metals. Increasing the pore density, either by reducing the pore size or increasing the porosity will give rise to a greater permeability, resulting in more energy dissipation as a result of frictional losses and thermoelastic damping. The low permeability of closed pore materials results in poor acoustic absorption. The absorption performance of closed pore materials can be improved upon by using pore-opening techniques such as hole drilling.

2.8 Permeability

The interconnection of pores within a porous metal means that a fluid or gas can be made to flow through it. The resistance to flow through the porous metal is an important consideration in design applications. If the flow resistance is high, more energy is required to push the gas or liquid through the material. Despite this, high flow resistance can be of benefit, such as an attractive transition in reactant mass transport mode in fuel cells (Kumar and Reddy 2003), or more efficient heat transfer between fluid and solid in compact heat exchangers (Kim *et al* 2000).

Flow resistance of a Newtonian fluid through a porous medium is measured by the excess pressure required to cause the fluid to flow at steady-state, with a given uniform average velocity through a unit length of the porous medium (Despois and Mortensen 2005). A related but more widely used parameter is permeability, which can be defined as the ability of a material to transmit fluids.

2.8.1 Darcy's Law

At low fluid velocities, when flow is governed entirely by viscous friction within the fluid, Darcy's law can be used to describe the relationship between the fluid flow pressure drop across a porous medium, the fluid flow velocity and the permeability of the material (Darcy 1856):

$$\frac{\Delta P}{L} = \frac{Q_V \mu}{AK} \tag{2.11}$$

where ΔP is the pressure drop across the medium (Pa), L is the length of the medium (m), Q_v is the volumetric flow rate of the fluid ($m^3 s^{-1}$), μ is the dynamic viscosity of the fluid (N s m^{-2}), A is the cross-sectional area of the flow channel (m^2) and K is the viscous permeability coefficient (m^2).

A number of researchers have verified that Darcy's law only applies for slow, viscous flows, where the pressure drop is linearly proportional to the flow rate. Davis *et al* (1992) demonstrated that experimental data published by Darcy fitted the quadratic better than the linear model when higher flow velocities (> $4x10^{-3}$m s^{-1}) were observed. At higher flow velocities, the effects of inertia and turbulence become greater and the pressure gradient exhibits a parabolic trend. The mechanism responsible for this turbulence is the drag force imposed on a fluid by any solid surface impeding the flow (Khayargoli *et al* 2004). At these higher flow velocities, the pressure drop is higher and the flow relationship is no longer linear and the quadratic term must be accounted for in order to give an accurate description of the pressure drop (Boomsma and Poulikakos 2002). In general engineering applications, the law governing this fluid flow is a modified version of Darcy's equation (Dupuit 1863 and Forchheimer 1901):

$$-\frac{\Delta P}{L} = \frac{\mu}{K} V_D + \rho C V_D^{\ 2} \tag{2.12}$$

where K is the permeability of the medium, V_D is the Darcian velocity of the

fluid, ρ is the density of the fluid and C is the drag form coefficient of the medium. The term $\rho C V_D^2$ accounts for the inertia effects in the flow.

2.8.2 Permeability-Structure Relationship in Porous Metals

Open-pore porous metals are of particular interest when considering fluid-dynamical properties. When considering a function of an open-pore porous metal, the permeability is of great significance. A number of factors can affect its permeability, such as porosity, pore size, pore morphology and microstructure. The permeability of open-pore porous metals has been the subject of several prior investigations. The permeability of porous metals is difficult to model and is more accurate if determined experimentally (Antohe *et al* 1997). A number of investigations have been carried out by researchers to attempt to relate the permeability with the structural parameters and microstructure of different porous metals. Boomsma *et al* (2003) established that when the flow velocity exceeds $0.110 ms^{-1}$, the flow exhibits quadratic rather than linear behaviour in porous metals. Diedericks and Du Plessis (1997) modelled flow through homogenous foams. They showed that the form coefficient of the medium, C, becomes more significant as the flow velocity increases, giving rise to an increase in the drag force, which must be considered for an accurate depiction of the pressure drop.

Bhattacharya *et al* (2002) found experimentally that the drag form coefficient and the permeability show a good correlation to the structure of high porosity metal foams. Their results showed that the permeability increased with pore diameter and porosity, while the inertial coefficient depends only on porosity. Du Plessis

et al (1994) devised a model where a volumetric averaging approach was adopted to calculate the flow resistance of a fluid through a periodic unit cell shaped as a cube containing three perpendicular solid rods of rectangular cross-section located along three of its edges. The model agreed fairly well with experimental data obtained on ERG aluminium foams of high porosity, between 92% and 96%; however, a modification to the model was required to fix the ratio between the edge length of the cell and the average pore diameter. This issue was resolved when Fourie and Du Plessis (2002) calculated the ratio between the cubic pore size and a more realistic tetrakaidecahedral pore shape. This model showed very good agreement with experimental data obtained.

Tadrist and Miscevic (2003) investigated the use of randomly stacked fibrous materials and commercially available, high porosity metallic foams in compact heat exchangers. They related the pressure drop, inertial effects, the porosity, ε, and the mean particle diameter, D_p, by:

$$\frac{\Delta P}{L} = A\frac{(1-\varepsilon)^2}{\varepsilon^3 D_p^{\,2}}\mu V + B\frac{(1-\varepsilon)}{\varepsilon^3 D_p}\rho V^2 \tag{2.13}$$

where A and B are constants, which depend on the structure of the porous metal. The permeability, K, can be estimated using the first term in Eq. 2.13 as:

$$K = \frac{D_p^{\,2}\varepsilon^3}{A(1-\varepsilon)^2} \tag{2.14}$$

These equations are suitable for the granular media studied, but problems arise when the structural properties of the porous metal differ.

Khayargoli *et al* (2004) tested the impact of microstructure on the permeability of two types of porous metal. The aim of the study was to relate the pressure drop with important related parameters, such as the permeability and the drag coefficient by combining experimental and modelling techniques. They concluded that differences in the permeability and drag coefficient in the two types of porous metal result from the differences in the microstructure between them.

Dukhan (2006) correlated the pressure drop with flow on a series of open pore aluminium samples, using an incompressible airflow. The pressure drop generated by the test samples increased with the Darcian flow velocity, following the quadratic equation developed by Forchheimer in 1901 (Eq. 2.12). Samples with higher porosity produced the lowest pressure drops, with the permeability and drag form coefficient correlating well with porosity.

When the porosity of a porous metal increases, the flow resistance decreases, resulting in a lower pressure drop. Several researchers have found that as the porosity increases, the permeability increases using experimental and modelling techniques (Boomsma and Poulikakos 2002 & 2003, Bhattacharya and Mahajan 2002, Dukhan 2006). Generally, the permeability of a metal foam increases as the pore size increases, for a fixed porosity (Pack *et al* 2000).

2.9 Applications of Porous Metals and Metallic Foams

There are a vast number of variables which affect the potential applications of porous metals. These include the base metal, pore type (open or closed), pore size, porosity, pore shape and structure, connectivity and the pore uniformity. These factors are all dependant on the manufacturing method used for producing the porous metal. In general, closed-pore structures are favoured for applications where a high specific strength, stiffness and energy absorption are required, whilst open pore structures are more adaptable to thermal and acoustic management.

2.9.1 Structural and Mechanical Applications

The mechanical properties of porous metals vary extensively, due to the varied structural parameters characteristic of the base metal and manufacturing process. For this reason, it is difficult to limit them to certain characteristics and applications. Low density, combined with reasonable shear and fracture strength, makes porous metals ideal for sandwich construction. A sandwich structure consists of two face sheets, usually made from metals or composites, enclosing a sheet of porous metal. It can be used in self-supporting lightweight structures for the building and transport industries (Gibson and Ashby 1997, Ashby *et al* 2000, Banhart 2001, Banhart *et al* 2003).

The excellent energy absorption characteristics of porous metals, combined with good mechanical strength make them ideally suited for use as internal and

external impact protection in transport applications (Thiele 1972). Metal foams could exploit their good isotropic properties and replace expensive honeycomb filler materials, which are currently being used. Similarly, closed-cell porous metals could be used as lightweight decks and bulkheads in the marine industry.

Porous metals can also be used as structural parts in aircraft, gearbox housings, motorcycle frames, aircraft crash recorders, safety pads in systems for lifting and conveying and shock absorbing mounts (Dilley 1974).

2.9.2 Thermal Management

Porous metals, especially copper and aluminium are an obvious choice for use as heat exchangers, because of their permeability to fluids and the good thermal conductivity of the base metal. The pore structure of a porous metal gives rise to an extremely high surface area, allowing heat to be transferred efficiently. Due to the porosity and permeability of the foams, water can easily flow through the foam with varying degrees of resistance. The flow-rate will depend upon the relative density and the pore size, which can be controlled depending on which process is used to manufacture the material.

One particularly interesting area is the use of copper and aluminium foams as heat sinks in the electronics industry. If the foam is attached to an electronic power device where a heat sink is required, the foam could absorb heat from the component and transfer it to the water flowing through the foam in a continuous circuit. Boomsma *et al* (2003) carried out a study on a set of open-cell,

compressed aluminium alloy foams, intended for electronic cooling applications, which dissipate large amounts of heat. They found that the compressed foams decreased the thermal resistance by almost half when compared to currently used heat exchangers designed for the same application. The controlled porosity and permeability would make porous metals, such as copper, ideal candidates for use in radiator construction, particularly in the automotive industry. Klett *et al* (2001) discovered that a graphite foam filled radiator can transfer heat more efficiently than conventional finned radiators.

The low thermal conductivity of porous metals, together with a very useful property that they are highly permeable and fireproof, make them ideal materials for flame arresters, preventing flame propagation along pipe-work and enclosures. A low thermal conductivity is beneficial to fire resistance as it prolongs the time required for the temperature of the unexposed surface to reach its critical temperature (Lu and Chen 1999). It has been found that a 6mm sample of RETIMET^{TM} has stopped hydrocarbon flames travelling at 210ms^{-1} (Davies and Zhen 1983).

NASA has recently been researching into the use of open-celled nickel foam in a thermal protection system for a wide range of aerospace applications, especially for reusable launch vehicles, which need to re-enter the earth's atmosphere (Sullins *et al* 2001). Porous nickel has a high melting point and a low relative density. Obviously this would be advantageous for space flight, where weight consideration is of major importance.

2.9.3 Acoustic Applications

Porous metals have been utilized in the operation of high-pressure gas-pipe lines for noise reduction. When gas is transported over large distances into local networks, the reduction in pressure produces a high intensity noise. Porous metal arrangements gently diffuse the gas, almost eliminating the noise (Davies and Zhen 1983). Porous metals have also been used as exhaust silencers for air tools and automobiles. High porosity porous copper sheet arrangements, with interleaved open-mesh nylon spacers, have been successfully used in these applications (Dilley 1974).

Due to the relatively early stages of development, the number of current applications for the use of porous metals in acoustic absorption is low. A limited number of studies have been made regarding the acoustic absorption properties of porous metals; however early results look promising.

2.9.4 Other Applications

The permeability qualities of porous metals make them the obvious choice for use in various industrial filters, to separate solid particles from flows of liquids, such as refrigerants, oils, petrol, polymer melts, aqueous suspensions, or from flows of gasses (Davies and Zhen 1983). The most popular materials used for porous metal filters are bronze and stainless-steel (Davies and Zhen 1983). Copper FOAMETAL™ can be used to filter foreign matter and contaminants in air-lines, preventing them from reaching valves and other pneumatic controls.

Correspondingly, nickel FOAMETAL™ can be used to filter out contaminants in hydraulic systems (Dilley 1974). A form of compressed porous metal is currently being used as a support for the osmotic membranes in kidney machines, where osmosis is carried out (Bray 1972).

Porous metals have been used in electrochemical applications to manufacture electrodes for alkaline batteries and fuel cells. Electrodes in alkaline batteries are generally made from a highly porous nickel with porosities ranging between 70 and 90%. For fuel cell applications, porous nickel with porosities ranging between 50 and 60% is the most efficient (Lenel 1980). Foam based nickel metal hydride batteries are currently competing with lithium ion batteries for applications in lightweight, cordless electronics (Ettel 1998).

As well as the engineering properties, the other properties, such as the aesthetic characteristics, of porous metals can also be exploited.

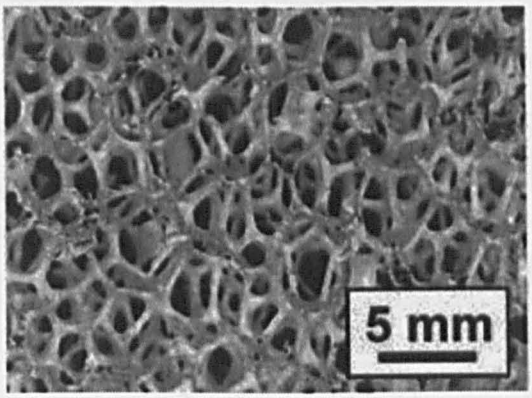

Figure 2.1 *Scanning Electron Microscope image of an ALPORAS™metallic foam manufactured using a foaming agent (www.imechanica.org).*

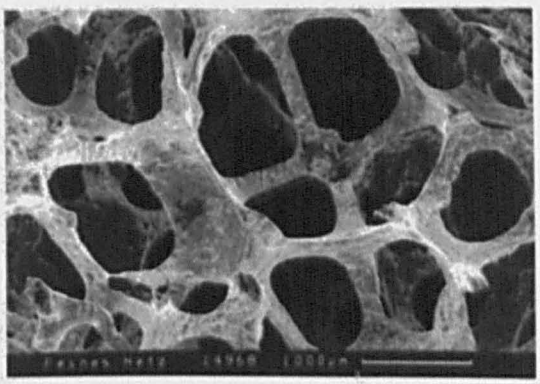

Figure 2.2 *Scanning Electron Microscope image of a DUOCEL™ metallic foam manufactured using Investment Casting (www.metalfoamheatexchangers.com).*

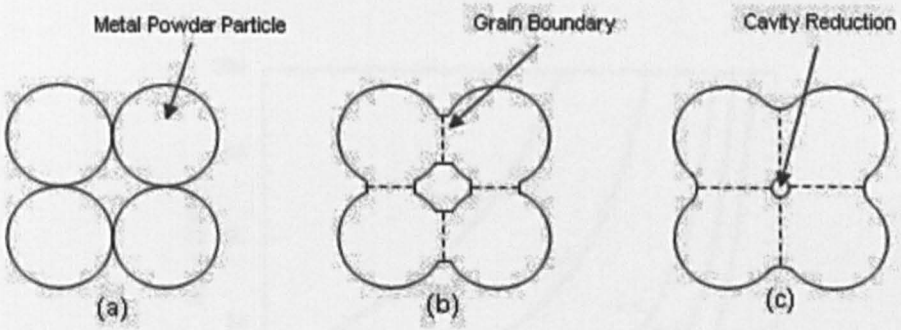

Figure 2.3: *The sintering process showing (a) four adjacent metal powder particles, (b) neck formation and particle coalescence and (c) cavity/pore size reduction and development.*

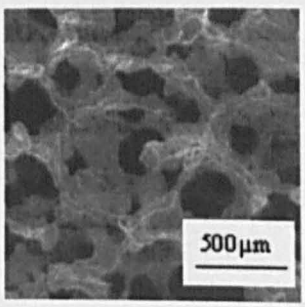

Figure 2.4: *Scanning Electron Microscope photograph showing microstructure and cell morphologies of Al foams manufactured using the SDP process (Zhao & Sun 2001).*

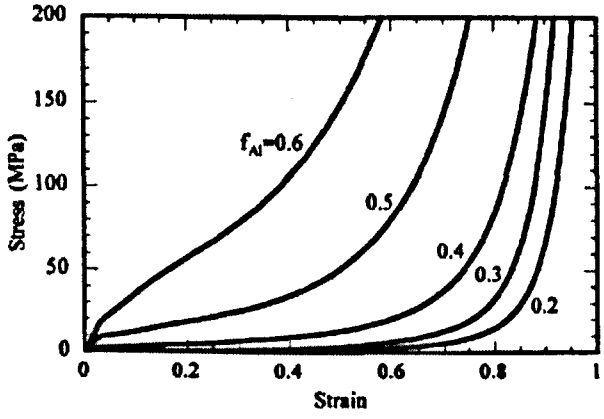

Figure 2.5: Compressive stress-strain curves of Al foams with varying Al weight fractions (Zhao & Sun 2001).

Chapter 3

EXPERIMENTAL

All the porous copper test samples used in this study were manufactured using the LCS process developed by Zhao *et al* (2005). A series of experimental tests were carried out on these samples to study and examine their electrical conductivity, thermal conductivity, fluid permeability, heat transfer properties and acoustic absorption behaviour. The experimental procedures are described in detail in the following sections.

3.1 Preparation of Test Samples by LCS

The LCS process involves four basic stages: mixing, compaction, sintering and dissolution (Zhao *et al* 2005). Figure 3.1 gives a graphical representation of the basic process. These stages are described separately below.

3.1.1 Raw Materials

The LCS process allows the pore dimensions and porosities of the test samples to be accurately controlled by mixing a copper (Cu) powder with potassium carbonate (K_2CO_3) granules at a specific volume ratio. The copper powder was supplied by Ecka Granules UK Ltd. and had a purity of 99 – 99.5% as quoted by the manufacturer. The copper powder particles are shown in Figure 3.2(a). The

shape of the particles was spherical. The particle size of the copper powder was not of critical importance, but was required to be considerably smaller than the size of the required pores, i.e. the size of the potassium carbonate granules. The diameter of the copper powder particles used for all test samples ranged between 20 and 75μm, having a mean diameter of approximately 40μm. The potassium carbonate granules were supplied by E&E Ltd. and had a purity of 98 – 100% as quoted by the manufacturer. The potassium carbonate granules are shown in Figure 3.2(b). The shape of the carbonate granules used was rounded. The particle size of the carbonate granules was selected according to the required pore size of the final test sample, because the morphology and size of the pores within the samples are virtual replicas of the shape of the carbonate granules. The carbonate powder was sieved mechanically and categorised into five different size ranges: 125 – 250μm, 250 – 425μm; 425 – 710μm; 710 – 1000μm and 1000 – 1500μm. These five size ranges resulted in the five different pore sizes used in all the tests.

The amounts of copper powder and carbonate granules for each particular test sample were determined by the intended size and porosity of the sample. Neglecting the air trapped in the copper/carbonate mixture, the total volume of the copper and carbonate powders is equal to the volume of the resultant sample, and the volume ratio between the carbonate powder and the copper/carbonate mixture is equal to the porosity of the resultant sample. The weights of the copper powder, W_{Cu}, and the carbonate powder, W_{K2CO3}, needed for fabricating for a porous copper sample of volume V and porosity ε (expressed as a fraction) were therefore determined by:

$$W_{Cu} = (1-\varepsilon)V\rho_{Cu} \quad W_{K_2CO_3} = \varepsilon V\rho_{K_2CO_3} \tag{3.1}$$

where ρ_{Cu} = 8.9g/cm^3 is the density of copper and $\rho_{K_2CO_3}$ = 2.3g/cm^3 is the density of potassium carbonate.

3.1.2 Container Preparation

Mild steel cylindrical tubes were used as containers for copper/carbonate mixtures for subsequent compaction and sintering. The tubes were machined to size using a metal cut-off saw and a mechanical lathe. The sizes of tube used depended on the final sample sizes required, which were different for different tests. The wall thickness of tube needed to be sufficient to withstand the force of the hydraulic press used during the compaction stage. A thin tube wall would result in twisting and distortion of the wall during compaction. For cylindrical samples with a diameter less than 30mm, a tube with wall thickness of 2mm or greater was sufficient. For the larger samples with a diameter of 100mm, a wall thickness of 10mm was used, due to the larger force required on compaction. After machining, the internal surface of the tube was smoothed and cleaned thoroughly using a 1200 grit sandpaper and a cloth. Any impurities left on the internal walls of the tube could result in contamination of the final sample and so thorough cleaning was imperative. Once clean, the tube was placed on a machined stainless steel plug and an amount of iron powder was poured into the tube through a funnel. The iron powder consisted of irregularly shaped particles in the order of 100μm (Figure 3.3). A stainless steel punch was then inserted into the tube. The diameter of the punch was such that a "sliding" fit within the tube

was achieved; the length of the punch was approximately one and a half times the length of the tube. The whole assembly of tube, plug, iron powder and punch were then placed under a hydraulic press and the iron powder was compacted at a pressure of 60MPa. The tube was safely lifted from the press and the punch was removed. The iron powder (once compacted) acted as a seal to prevent the copper/carbonate mixture from reacting with air during the sintering stage. The amount of iron powder was required to be enough to achieve a 5 – 10mm seal after compaction.

3.1.3 Mixing and Compaction

The copper and carbonate powders were weighed and mixed together in the pre-specified ratio, according to the final porosity required. Approximately 1 – 2% vol Ethanol was added to the mixture to act as a binding agent between the copper and carbonate particles. The mixing took place in a sealed plastic beaker by manual shaking. The sealing of the beaker ensured no evaporation of the ethanol during mixing. Full mixing was realized after approximately thirty seconds when a clear separation between the copper and carbonate particles could not be seen visually. A layer of potassium carbonate powder, approximately 2 – 3mm thick, was first added to the aforementioned tube container to act as a barrier between the iron seal and the copper/carbonate mixture. The copper/carbonate mixture was then added to the tube using a different funnel to the iron powder to avoid contamination. The copper/carbonate mixture was compacted in the hydraulic press using the punch at a pressure of 200MPa for approximately ten seconds. This compaction pressure was selected based on the

principle laid down in the previous research (Zhao *et al* 2005). The tube was again safely removed from the press. Another 2 – 3mm layer of potassium carbonate powder and a second layer of iron powder were poured on top of the compressed copper/carbonate mixture and then compacted at a pressure of 60MPa in order to achieve a seal at the other end of the tube. The plug at the bottom of the tube was then removed manually. A schematic diagram of a typical perform/tube assembly ready for sintering is shown in Figure 3.4.

3.1.4 Sintering

The sintering process took place in an electric furnace. The preform/tube assembly was placed at the centre of a cold furnace to allow maximum aeration and even heat distribution. The furnace was then heated up to the sintering temperature of 850°C, normally reached in one hour from cold, and was programmed to remain at this temperature for a period of time depending on the sample size. This sintering temperature was selected such that the particles of potassium carbonate, which have a melting point of 891°C, remained in the solid state. The sintering times for different sample sizes are shown in Table 3.1. Once the sintering process was complete, the assembly was left to cool from 850°C to room temperature within the furnace. The time taken for cooling depended on the sample size, as shown in Table 3.1. The preform/tube assembly was then removed from the furnace.

Table 3.1 Sintering and cooling times of different sized test samples.

Sample Diameter (mm)	Sintering Time (Hrs)	Approximate Cooling Time (Hrs)
21mm	4	18
30mm	4	18
100mm	8	30

3.1.5 Preform Removal and Shaping

The next stage involved removing the copper/carbonate preform from the tube container. This was achieved using a milling machine to cut down the lengths of opposite sides of the tube. The depth of the cut was controlled to be the thickness of the tube wall, so that it did not interfere with the contained preform. Once the two cuts were complete, the two sides of the tube were removed by manually, leaving the sintered copper/carbonate preform together with the two iron seals and the separating carbonate layers. The preform was further separated from the carbonate and iron layers. This operation was easily carried out because of the low adhesion between the preform and the carbonate layer.

The sample was machined to its required size and shape using a standard mechanical lathe. The surfaces of each sample were ground using a laboratory grinding machine with sandpapers ranging between 400 and 1200 grit. All machining and grinding was carried out in dry conditions while the potassium carbonate was still present within the perform in order to prevent damages and smearing of the pores.

3.1.6 Carbonate Dissolution

The sintered copper/carbonate preforms were placed in a running bath of cold water for a period of four hours. This allowed the water to penetrate the preforms and all the carbonate particles were dissolved and removed, leaving a porous copper network. After four hours, the wet porous copper samples were immediately placed inside an electric furnace at a temperature of 100°C for one hour. The finished samples were safely removed from the furnace, and allowed to dry to room temperature.

3.1.7 Density Measurement

In theory, the volume of the potassium carbonate in a copper/carbonate preform is equal to the volume of the pores in the resultant porous copper, if full compaction is achieved. The porosity would be easily calculated from the volume ratio of copper powder and potassium carbonate powder. In practice however, there always exists porosity in the copper/carbonate preform due to incomplete compaction and there is always some amount of shrinkage during subsequent sintering. The actual porosity of the porous copper sample often deviates from the target porosity as determined from Eq. (3.1). Grinding and polishing of the samples can also lead to some deviations. Therefore, it is necessary to measure the density or porosity experimentally.

Two methods can be implemented to measure the density of the test samples. The porosity can be obtained from the relative density, which is the ratio between

the density of the porous copper and the density of solid copper. The first method is the simpler technique, where the weight of the sample is measured by an electronic balance and the volume of the sample is determined by measuring the dimensions of the sample using a vernier calliper. The density can then be calculated. The second method is the Archimedes method. This principle states that the weight of an object in a fluid equals its dry weight minus the buoyant force (or the weight of the fluid displaced). This involves taking the samples dry weight, its saturated weight in a fluid, and its net saturated suspended weight. The second method is far more accurate than the first method, especially when the physical measurements of the dimensions of a sample are difficult, e.g. when the sample is damaged or has an irregular shape. In this study, the Archimedes method was employed to measure the density of the porous copper samples, from which the relative density and porosity were calculated.

3.2 Structural Analysis

Optical microscopy, Scanning Electron Microscopy (SEM) and quantitative metallography were used to analyse the microstructure of the sintered porous copper test samples. A Nikon optical microscope was generally used at low magnifications to inspect the presence of any oxide films on the surfaces of the completed samples, as well as a check for homogeneity of pore distribution between batches of samples. The optical microscope was also used to take micrographs of various samples for quantitative metallography. A Cambridge Instruments Stereoscan 100 SEM was used for more detailed analysis on particle bonding and pore structure.

For quantitative metallographic analysis, the samples were first set in a dissolvable polymer so that no deformation to the pore structure occurred during the grinding and polishing processes. Each sample was then ground 3mm into the surface and polished to a degree of 6μm, so that low magnification optical micrographs of the cross section could be taken and analysed. A typical ground and polished test sample set in the dissolvable polymer is shown in Figure 3.5.

The porosity and the specific surface area of the porous copper samples were measured by applying the point counting method. A counting grid was superimposed onto a micrograph of the test area of the sample. Figure 3.6 shows the micrographs and corresponding counting grids for eight test samples, A1 to A8. The porosity, ε can be defined as the volume fraction of the pores with respect to the total volume of the sample and can be calculated by:

$$\varepsilon = \frac{P_{PORE}}{P_{TOT}} \times 100 \tag{3.2}$$

where P_{PORE} is the number of points located in the pores and P_{TOT} is the total number of testing points within the selected area (Thomson 1930, Glagolev 1933, Underwood 1970). The specific surface area is defined as the ratio of the total internal surface area to the total volume of a sample, and can be obtained by:

$$S_V = 2P_L \tag{3.3}$$

where S_V is the specific area and P_L is the point per line, i.e. the number of points that the testing lines intercept with pores per length of the lines. Testing lines can be applied in any direction on the surface of the test specimen. The point counting method was applied over the complete face area of each sample with a fine grid, so that an accurate estimation of the porosity and specific surface area could be made.

3.3 Thermal Conductivity

The thermal conductivity tests on five porous copper samples were carried out at atmospheric pressure using a method developed by Corsan (1984). The basis for this method can be explained as follows. The heat flow rate of a one-dimensional steady state problem in any one conductor can be expressed as:

$$Q = \lambda A\left(\frac{\delta T}{\delta x}\right) \tag{3.4}$$

where Q is the heat flow rate, λ is the thermal conductivity, A is the cross-sectional area of the conductor and $\delta T/\delta x$ is the temperature gradient. Assuming that the porous copper specimen and the comparator were perfectly insulated circumferentially, the heat flow rate is a constant throughout the porous specimen and the solid comparator. As the cross sectional area, A, is also the same in both the comparator and the porous specimen, the thermal conductivity of the porous copper, λ_2, is given by:

$$\lambda_2 = \lambda_1 \frac{\left(\frac{\delta T}{\delta x}\right)_1}{\left(\frac{\delta T}{\delta x}\right)_2} \tag{3.5}$$

where λ_1 is the thermal conductivity of the solid copper comparator, given by the manufacturer as $390 Wm^{-1}K^{-1}$, $(\delta T/\delta x)_1$ is the temperature gradient in the solid copper comparator and $(\delta T/\delta x)_2$ is the temperature gradient in the porous copper test specimen.

Figure 3.7 shows a schematic diagram of the test apparatus designed and built for this purpose. The porous copper specimen is cylindrical in shape and has a length 110mm and diameter 19mm. Two of the test samples are shown in Figure 3.8. A commercially pure solid copper comparator of length 150mm and diameter 19mm was clamped down onto the test specimen using an aluminium clamping jig. The adjusting nuts on the upper clamping plate were tightened manually with a torque wrench, each to 20Nm. Thermally conductive grease, supplied by CHEMTRONICS® was applied to the end of the test specimen and the end of the comparator, so that the heat was conducted effectively through the interface. The value of thermal conductivity as given by the manufacturer was 9.6 $Wm^{-1}K^{-1}$. The clamp held the solid copper comparator and the porous copper sample together firmly and ensured a good contact at the interface.

Holes with a diameter of 2mm were drilled at specific, measured locations along the length of the comparator and the porous copper test specimen using a pillar drill. Each hole had a depth of 9.5mm and had a K-type thermocouple located in

it. The end of each thermocouple had a heat-shrunk plastic shroud around it to provide a tight fit in the drilled hole and to ensure that the temperature reading was from the precise axial centre of the specimen. All the thermocouples were linked up directly to a data acquisition unit, with a resolution of 0.01°C. The solid copper comparator had a 6mm bore at the top end for an 80W cartridge heater to be located. The heater was controlled using a variable transformer so that a steady-state temperature could be achieved accurately at thermocouple 1, in the comparator. The test specimen and comparator were insulated circumferentially, using a combination of calcium-magnesium-silicate wool and polyethylene to minimize radial heat losses. Thermal insulation in the form of calcium-magnesium-silicate wool was also added between the comparator and the upper clamping plate to prevent heat conduction and subsequent dissipation through the aluminium apparatus. The lower plate of the clamping apparatus acted as a heat-sink for the test specimen, to ensure a steady temperature gradient through the comparator and the test specimen. Figure 3.9 shows typical temperature plots of the 8 thermocouples as a function of time.

Once the temperature within the samples reached its steady-state (after approximately one hour, depending on the relative density of the sample), the temperature reading was taken at each of the thermocouple locations by the data acquisition unit. The steady-state temperatures at thermocouple 1 varied slightly among the samples, but all were in the range of 100± 6°C. The temperature gradients in the comparator and the porous copper can be obtained from the temperature plots along the lengths of the comparator and the porous copper sample. The thermal conductivity of the porous copper sample was then

determined from the temperature gradients obtained from the test specimen and comparator using Eq. (3.5).

3.4 Electrical Conductivity

Since free electrons are responsible for both electrical and thermal conduction in pure metals, theoretical treatments suggest that the electrical and thermal conductivities should be related. Assuming that the dominant mechanism for both electrical and thermal conduction in the porous copper sample is conduction by free electrons, then the thermal conductivity of the sample can be estimated from its electrical conductivity by the Wiedemann – Franz law as (Callister 2000):

$$\lambda = LT\sigma \tag{3.6}$$

where λ is the thermal conductivity, L is a constant with a theoretical value of $2.44X10^{-8}$ Ω-W/(K)^2, T is the absolute temperature, and σ is the electrical conductivity. It should be noted that L should be independent of temperature and equal for all metals provided that heat energy is transported entirely by free electrons.

The electrical conductivity of thirty porous copper specimens was measured using a Sigmatest 2.068 conductivity meter. The instrument uses eddy currents to establish the resistance to the flow of current in the material and hence the conductivity. Each measurement was taken six times at different locations on the

surface of each sample and a 16.7% trimmed mean value for the electrical conductivity was calculated for each, by discarding the uppermost and lowermost values. All tests were carried out in atmospheric conditions at a temperature of 21± 0.5°C. In order to verify the thermal conductivity results obtained using the Corsan method, the thermal conductivity values of each electrical conductivity measurement was calculated using Eq. (3.6).

3.5 Permeability

3.5.1 Principle for Permeability Measurements

Permeability of a porous material quantifies its ability to conduct a fluid. The permeability of a porous copper sample can be measured by directing a fluid flow through the sample and measuring the fluid pressure drop across the sample and the flow rate of the fluid directed through it. The relationship between pressure drop and permeability is normally expressed as (Davies and Zhen 1983):

$$\frac{\Delta P}{l} = \frac{\mu Q_V}{\psi_v A} \tag{3.7}$$

where ΔP is the fluid pressure drop across the test sample (N/mm^2), l is the length of the test sample (m), A is the cross sectional area of the sample (m^2), μ is the dynamic viscosity of the test fluid, Q_V is the volumetric flow rate of the fluid (m^3) and ψ_v is the viscous permeability coefficient, or simply permeability (m^2).

3.5.2 Experimental Apparatus

A schematic diagram of the experimental apparatus used for the permeability tests is shown in Figure 3.10. The fluid used in the tests was water, which has a dynamic viscosity of 0.001 N s/m^2 at 20°C. The system was connected to the mains water supply through a 19mm copper pipe. The water flowed through a filter, one of the two flow meters, a first ball valve, a needle valve, the input pressure transducer, the porous copper sample contained in the sample holder, the output pressure transducer and a second ball valve before discharged to the drain. The polypropylene cartridge filter was fitted with a relief button, so that any air trapped within the system could be released after each test to avoid air-traps. The two flow meters were connected to the water pipe via a plastic push-fit water trap tee connection. An isolator valve was fitted at the output of each flow meter so that one could be by-passed when the other was in use. The flow meters had different resolutions, so that more accurate measurements could be made when lower flows below 1bar were used. The range of the first flow meter was from 0.2 to 2 l/min and the range of the second from 1.5 to 10 l/min. The flow meters were calibrated by catching water exiting the flow meter over a given time. The first ball valve acted as an isolator, shutting off the water supply to the test sample when closed. The needle valve acted as a fine adjuster for the water input pressure to the test sample. The input pressure transducer was screwed into a 1/2inch BSP stainless steel tee. One end of the tee was connected to the needle valve through an over braid hose and the other end was connected through a hexagonal equal nipple into the flange of the sample holder. The flange was machined from 316 stainless steel and bolted to the input end of the sample

holder using 5mm hexagonal stainless steel bolts. Similarly, the output pressure transducer was also connected to a tee, which was connected to the output end of the sample holder through a flange at one end and connected via a second ball valve to the drain at the other end. 1.5mm silicone gaskets were used between the flanges and the sample holder to form a seal, to prevent water leakage. Figure 3.11 shows a photograph of the key components in the assembled form.

The sample holder, as shown in Figure 3.12, was designed to house porous copper samples with lengths up to 40mm and diameters between 20 and 20.7mm. It was machined to shape using a block of commercially pure solid copper. A technical drawing of the sample holder is given in Figure 3.13. The housing consisted of two pieces of copper, which were bolted together using 6mm hexagonal bolts. When bolted together, a cylindrical bore ran through the centre, in which the test sample was located. The test sample was clamped in place by tightening the bolts, ensuring no gaps existed between the sample and the walls of the housing and water was channelled solely through the porous copper. A 1.5mm silicone gasket was inserted between the two copper pieces on either side of the bore. The gasket served two purposes: firstly it acted as a tensioner, so that test samples with slightly varying diameters could still be used within the housing; secondly it formed a seal, so that no water could penetrate between the two copper pieces.

The pressure transducers used for measuring the input and output pressures were Omega PXM219 powered using a 24V DC power supply. Each device was ready calibrated by the supplier. The transducers had a current output of 4 to

20mA± 1% over the full-scale, corresponding to 0 to 4bar in pressure. The transducers were connected to a data acquisition unit, which was linked to a personal computer.

3.5.3 Test Procedure

The permeability of twenty samples with different pore sizes and porosities was measured at different water flow rates at atmospheric conditions at a temperature of 20°C± 3°C. All samples were cylindrical in shape with diameters of 20mm ± 0.7mm and lengths in the region of 30mm. Each test sample was located within the bore of the sample holder and clamped in place using the hexagonal bolts. The holder was then bolted to both the inlet and outlet flanges. The flow threshold, or maximum flow rate, of the sample was first determined by opening the valves fully to allow the maximum surge of water flowing through the system and through the sample. The flow rate was then increased at systematic intervals up to this maximum flow rate using the needle valve. At each flow rate, the inlet and outlet pressures were recorded. With known cross sectional area and length of the sample, viscosity and flow rate of water, and input and output pressures, the permeability was calculated by Eq. (3.7).

3.6 Heat Transfer

The aim of the experiment was to measure the thermal performance of the porous copper samples, when used as heat exchangers in an open flow arrangement. The concept of the experiment was to direct a coolant through the test sample enclosed in a heating chamber and measure the heat transfer coefficient as an indication of the heat transfer efficiency of the test sample. Two typical test samples are shown in Figure 3.14.

3.6.1 Experimental Apparatus

A schematic overview of the experimental apparatus is shown in Figure 3.15. The experimental set-up was basically the same as that used for the permeability tests, with some modifications made to various parts of the apparatus. Specifically, the sample holder was replaced with a heating chamber and a series of thermal couples and thermometers were inserted at different locations for temperature measurements.

Figure 3.16 shows a photograph of the heating chamber. The chamber consisted of two machined blocks of oxygen-free copper, with a thermal conductivity of approximately 390 $Wm^{-1}K^{-1}$. The two blocks were bolted together in the same manner as those used in the permeability tests. The chamber was heated externally using ten Watlow FIREROD® cartridge heaters, delivering a maximum of 1.2kW to the chamber. The cartridge heaters were located in 6.5mm holes drilled at specific locations within the copper blocks. The heaters

were controlled using a variable transformer to generate a variable heating power and a steady electric current. The heating chamber was insulated using fibreglass lagging and the inlet and outlet pipes to and from the heating chamber were insulated using polyethylene pipe lagging.

The heat delivered to the chamber was conducted into the test sample and eventually convected into the coolant (mains water in this study) flowing through it, causing the coolant to heat up. The difference in temperature between the coolant flowing in and out of the sample was measured using two platinum resistance PT 100 thermometers, which offer a high accuracy of ±0.1°C over a wide temperature range. The thermometers were fixed into two machined brass blocks, with the tip of each temperature probe being located at the circumferential centre of the coolant flow at a distance of approximately 5mm from the surface of the test sample ends. A K-type thermocouple was located in a drilled 1.5mm hole on each half of the heating chamber to measure the temperature of each block. The data from the thermocouples and thermometers was acquired using a data acquisition unit and transferred to a personal computer.

3.6.2 Test Procedure

Each test sample was located into the bore of the heating chamber, which was then clamped together using the four hexagonal bolts and fixed into position by bolting it to the input and output flanges. Each of the ten cartridge heaters were located in the pre-drilled holes within the chamber, ensuring that each was pushed in fully. The fibreglass insulation was then placed around the chamber,

ensuring no surface of the block was open to the air. The polyethylene pipe insulation was then put in place over the input and output pipes. Measurements were taken using four different power inputs to the heating chamber, namely 150W, 350W, 600W and 1kW, and a series of water flow rates up to the maximum flow rate for the sample. Once the correct heating power was set, the flow rate was adjusted to the required level using the needle valve and the system was left to reach its steady state. Once a steady state was achieved, which took approximately ten minutes, the inlet temperature, T_{IN}, the outlet temperature, T_{OUT}, and the temperature of the heating chamber, T_{CH}, were recorded.

3.6.3 Compensation of Heating Chamber Effect

The heating chamber had a length of 40mm in order to accommodate enough cartridge heaters for the power density required for the tests. Due to discrepancies within the sample manufacturing process, some samples were shorter than 40mm. When these samples were located within the chamber, a section of the chamber wall was exposed to the coolant flow and transferred a certain amount of directly to the coolant that was independent of the sample being tested. The heat transfer coefficient of the walls of the heating chamber, with no sample inside, was measured at different flow rates and heating powers, and was found to have an average value of 4.1 kW/Km^2 over the full length. Taking this effect into account, all the experimental results were adjusted by removing the heating effect made by the section of the chamber wall exposed to the coolant.

3.6.4 Calculation of Heat Transfer Coefficient and Nusselt Number

The heat transfer between a solid and a liquid can be measured by the convection heat transfer coefficient (Boomsma *et al* 2003):

$$h = \frac{q}{A_{CON}\Delta T} \tag{3.8}$$

where q is the rate of heat transfer to the coolant, A_{CON} is the interfacial area between the solid and the coolant, and ΔT is the temperature difference between the solid and the coolant. As this study is concerned with the performance of the porous copper samples as a heat transfer medium from a heat source to a coolant, A_{CON} is taken as the circumferential surface area of the sample in contact with the heat block, and ΔT is taken as the difference between the temperature of the heat block and the average temperature of the coolant.

The temperature difference, ΔT, was estimated by:

$$\Delta T = T_{CH} - 0.5(T_{IN} + T_{OUT}) \tag{3.9}$$

where T_{CH} is the average block temperature measured by the two thermocouples, and T_{IN} and T_{OUT} are the temperatures of the water entering and exiting the sample, respectively.

The heat transfer rate to the coolant, q, was calculated by:

$$q = \dot{m}c(T_{OUT} - T_{IN}) \tag{3.10}$$

where m is the mass flow rate of the coolant flowing through the test sample, c is the specific heat capacity of the coolant, given as 4181.6 $Jkg^{-1}K^{-1}$ for water at 20°C (Cox *et al* 1989).

The performance of a heat exchanging device can be measured using the dimensionless Nusselt number (Boomsma *et al* 2003):

$$Nu = \frac{hD_{hyd}}{\lambda_f} \tag{3.11}$$

where D_{hyd} is the hydraulic diameter, given as a function of the cross-sectional area and wetted perimeter of the flow channel, and k_f is the thermal conductivity of the coolant. In this experiment, D_{hyd} was taken as the pore diameter of the test sample and λ_f for water was assumed to be 0.6 $Wm^{-1}K^{-1}$ at 20°C.

3.7 Acoustic Absorption

3.7.1 Standing Wave Tube Method

The standing wave tube method was employed to determine the sound absorption coefficient of the porous copper samples. This method allows measurements to be reproduced quickly and easily, whilst only requiring relatively small cylindrical samples with diameters of 30 or 100mm. Two methods are available that utilize the standing wave tube: the standing wave ratio method and the transfer-function method. The transfer-function method was used in this case. A comprehensive description of the standing wave tube method and calculation of the transfer-function can be found in EN ISO 10534-2:2001.

The test method uses a sound source with a flat spectral density within the required frequency range, connected to one end of an impedance tube. The test sample is fixed at the other end. A microphone located at two different positions along the length of the impedance tube measures the acoustic pressures and the decomposition of the interference field between the two positions. The acoustic transfer-function can then be calculated to determine the sound absorption coefficient. The normal incidence absorption and impedance ratios of the test samples can also be measured using this technique.

3.7.2 Calculation of Transfer Function

The measurement method is based on the principle that the sound reflection factor at normal incidence, r, can be determined from the measured transfer function, H_{12}, between two microphone positions (x_1 and x_2) in front of the test sample (BS EN ISO 10534-2:2001)

The transfer-function for the incident wave is given by:

$$H_I = \frac{P_{2I}}{P_{1I}} = e^{-jk_0(x_1-x_2)} = e^{-jk_0 s} \tag{3.12}$$

where P_{1I} and P_{2I} are the incident acoustic pressure at positions x_1 and x_2, $s = x_1 - x_2$ is the distance between the two microphone positions and k_0 is the wave number which is a function of frequency. In the same way, the transfer-function for the reflected wave is given by:

$$H_R = \frac{P_{2R}}{P_{1R}} = e^{jk_0(x_1-x_2)} = e^{jk_0 s} \tag{3.13}$$

where P_{1R} and P_{2R} are the reflected acoustic pressures at positions x_1 and x_2.

The transfer-function for the complete sound field can be expressed as:

$$H_{12} = \frac{P_2}{P_1} = \frac{e^{jk_o x_2} + re^{-jk_o x_2}}{e^{jk_o x_1} + re^{-jk_o x_1}} \tag{3.14}$$

where P_1 and P_2 are the complex acoustic pressures at positions x_1 and x_2.

Using equations (3.12), (3.13) and (3.14), the sound reflection factor, r, can be written as:

$$r = \frac{H_{12} - H_1}{H_R - H_{12}} e^{2jk_o x_1} \tag{3.15}$$

The sound absorption coefficient can be expressed in terms of the real and imaginary terms of r, r_r and r_i:

$$\alpha = 1 - |r|^2 = 1 - r_r^{\,2} - r_i^{\,2} \tag{3.16}$$

3.7.3 Test Procedure

Figure 3.17 shows the basic experimental set-up. The measurement equipment used consisted of an impedance tube, a test sample holder, an in-tube traversing microphone, a signal generator, a portable two-channel Fast Fourier Transform (FFT) analyser, a power amplifier, a loudspeaker and a sound level detector. The loudspeaker provided a broadband random signal, which was directed via the impedance tube to the surface of the test sample. The samples were either located directly against the back-plate of the test sample holder within the

impedance tube, or with a gap of 20mm or 50mm, between the sample and back-plate. The back-plate provided a solid, impermeable backing, so that after the incident wave passed through the test sample, it was reflected back from the back-plate. A single, traversing microphone was employed to ensure that there was no phase mismatch between the two measurement locations along the tube. The upper working frequency at which the measurements are taken was determined by the internal diameter of the impedance tube. This avoids the occurrence of non-plane wave mode propagation. Two sizes of tube were used for two frequency ranges. Measurements taken in the range of 100 – 1000Hz employed a tube with an internal diameter of 30mm, while measurements in the range of 500 – 5000Hz used a tube with an internal diameter of 100mm. The internal diameter size of the impedance tube determined the outside diameter of the test samples.

The sound absorption coefficient of a series of sixteen porous copper tests samples was measured. Vaseline was applied around the perimeter of the test samples to ensure that any pores or cavities were filled between the tube and the sample walls and that there was a total incident surface. Before the tests began, the sound absorption coefficient of the back plate of the impedance tube was measured. It had an average of just 0.05 over all frequencies tested and so its effect on any measurements was deemed to be negligible.

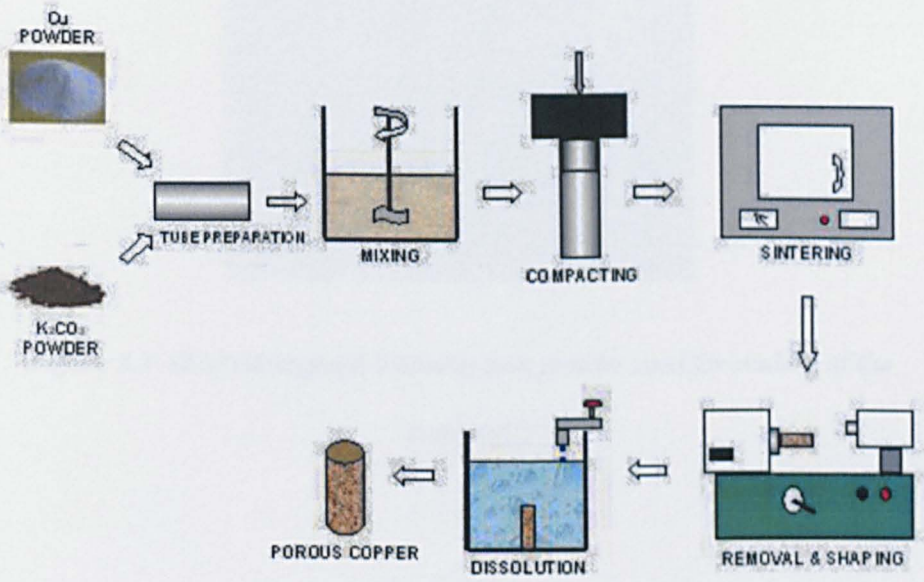

Figure 3.1: *Graphical representation showing each stage involved within the LCS process.*

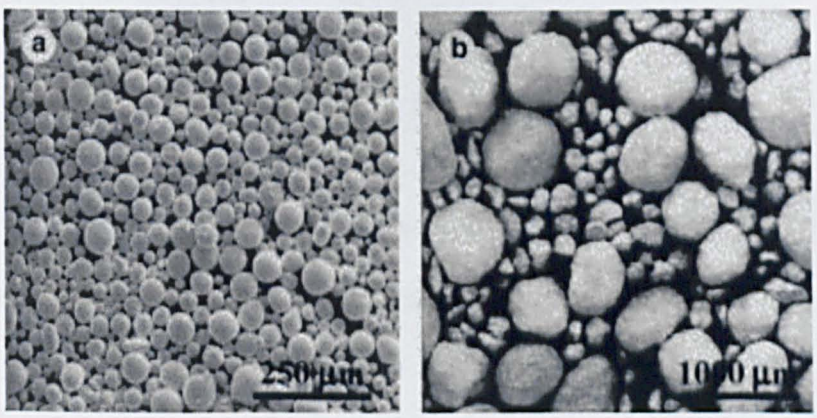

Figure 3.2 *SEM micrographs showing (a) copper powder particles and (b) potassium carbonate granules.*

Figure 3.3 *SEM micrograph showing iron powder used for sealing of the compact.*

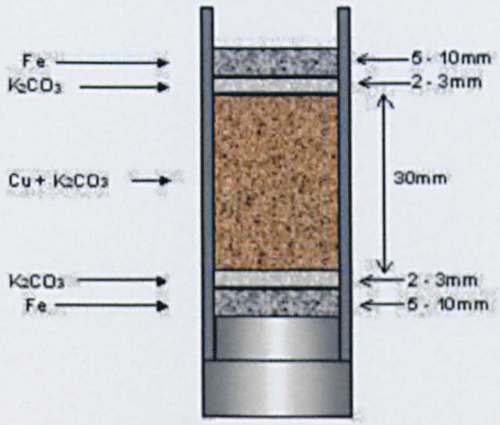

Figure 3.4 *Schematic diagram of a perform/tube assembly ready for sintering.*

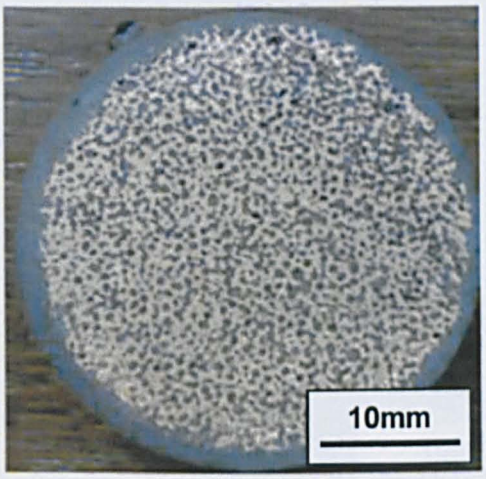

Figure 3.5 *Test sample set in a dissolvable polymer, ground and polished.*

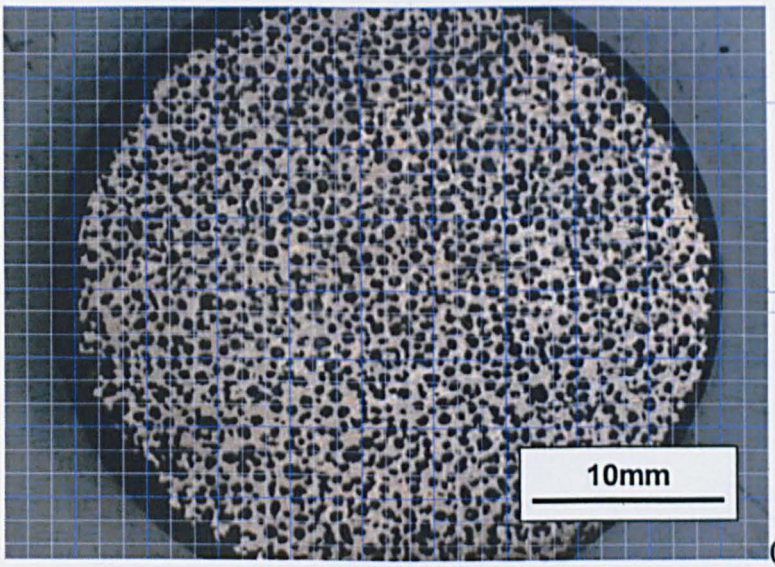

(a)

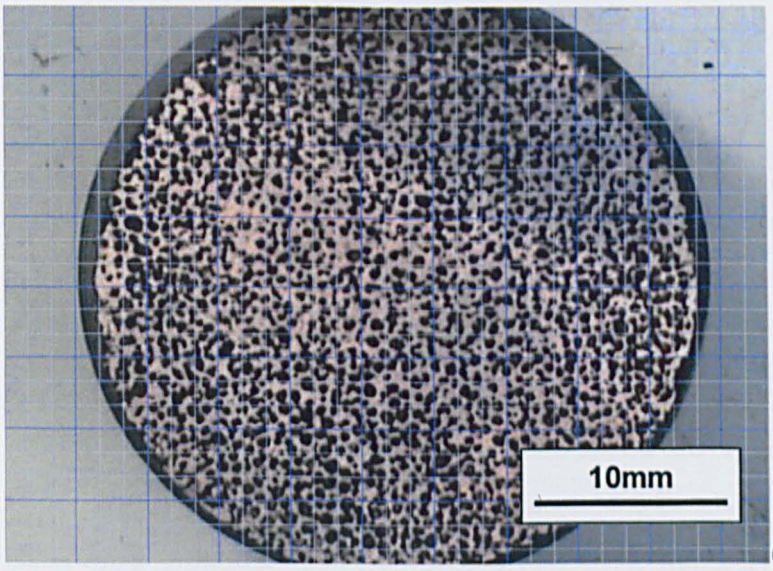

(b)

Figure 3.6 to be continued

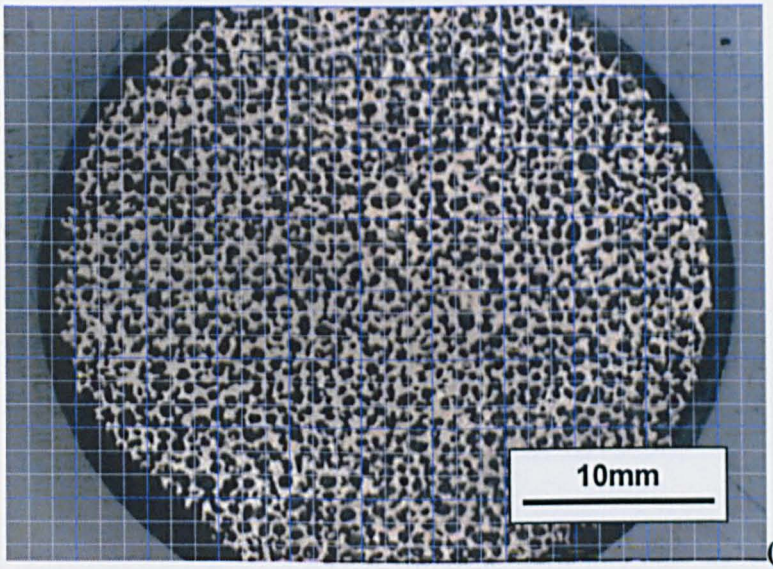

(c)

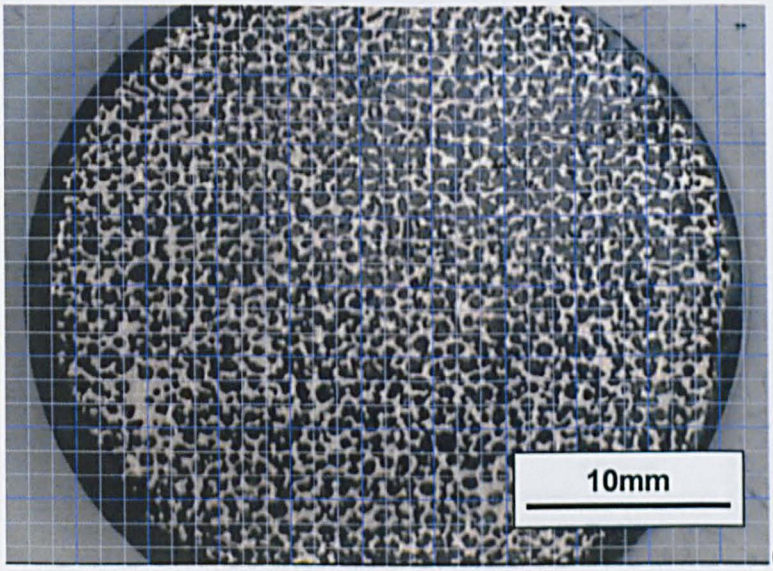

(d)

Figure 3.6 to be continued

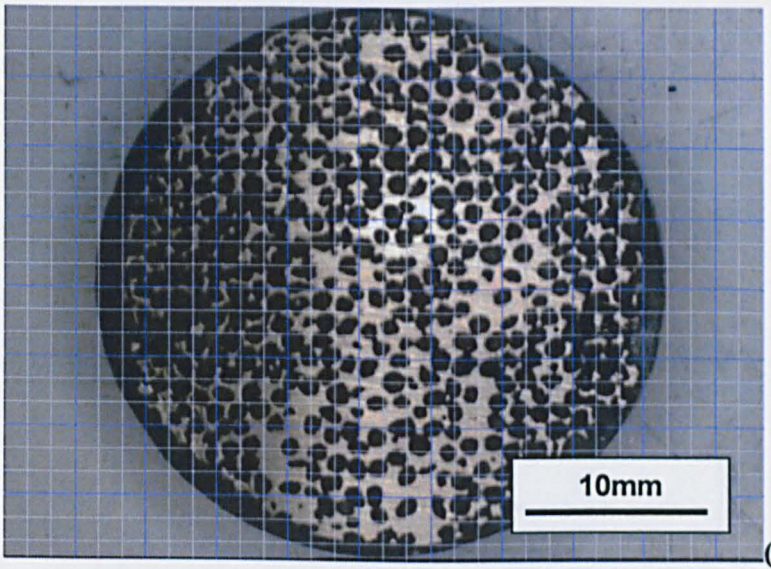

(e)

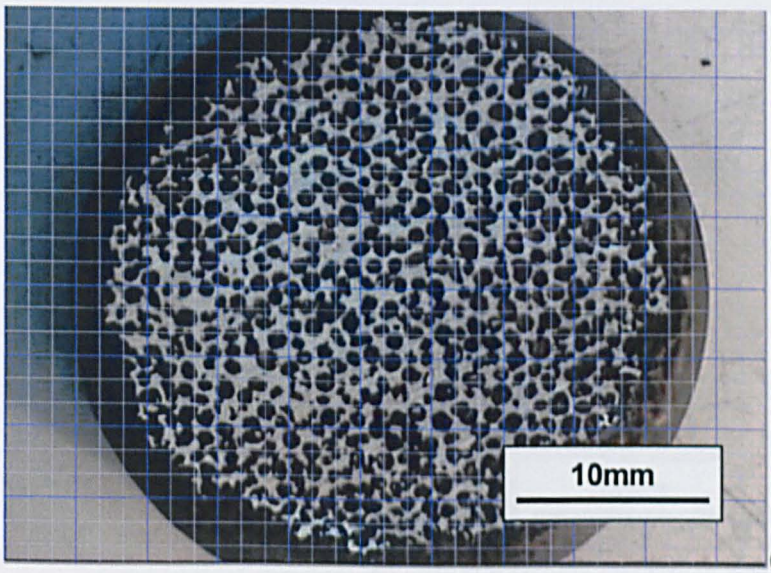

(f)

Figure 3.6 to be continued

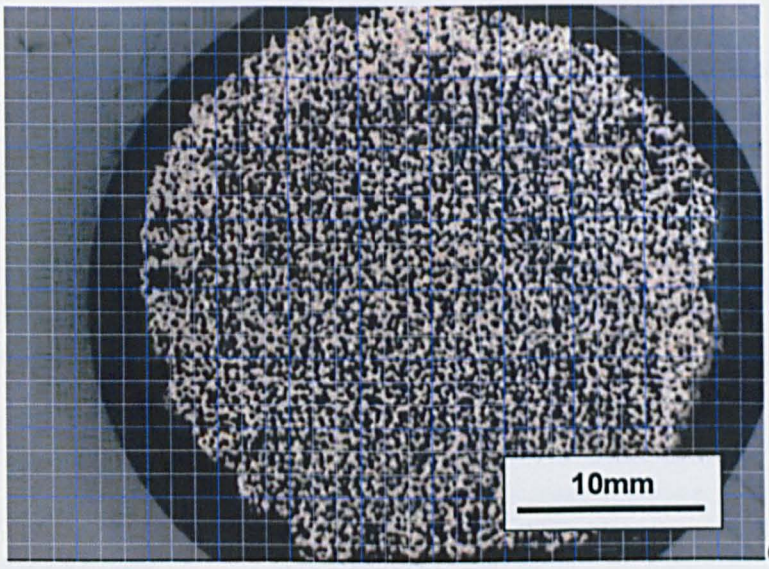

(g)

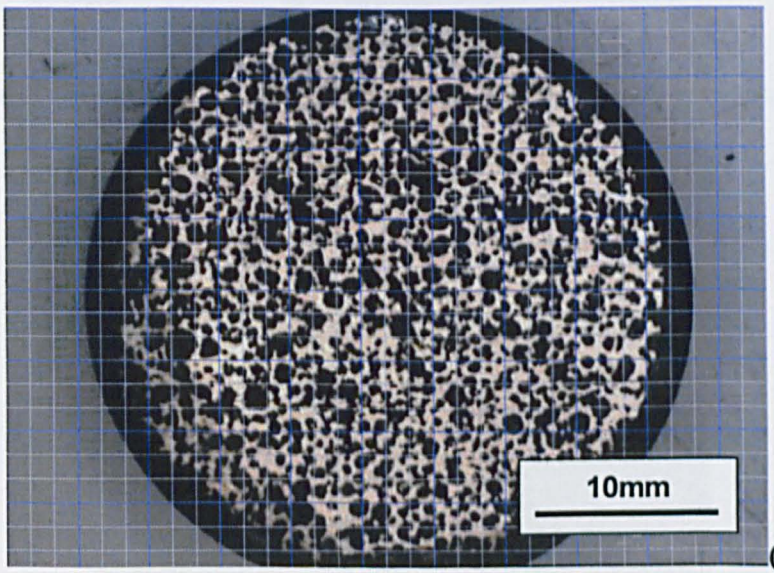

(h)

Figure 3.6 *Low magnification micrographs of samples A1 to A8 (a to h), with corresponding superimposed point counting grids, for quantitative analysis.*

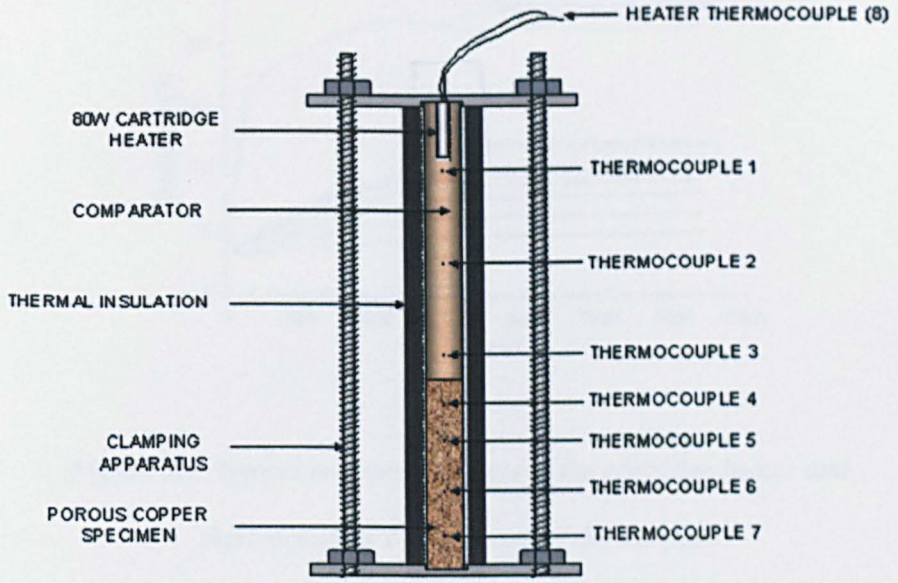

Figure 3.7 *Schematic diagram of the test apparatus showing the clamping jig, test specimen and comparator set-up.*

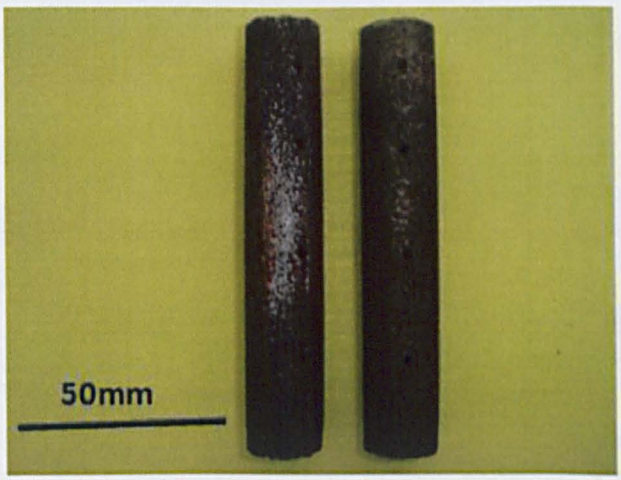

Figure 3.8 *Two thermal conductivity test samples, showing pre-drilled holes for thermocouple location.*

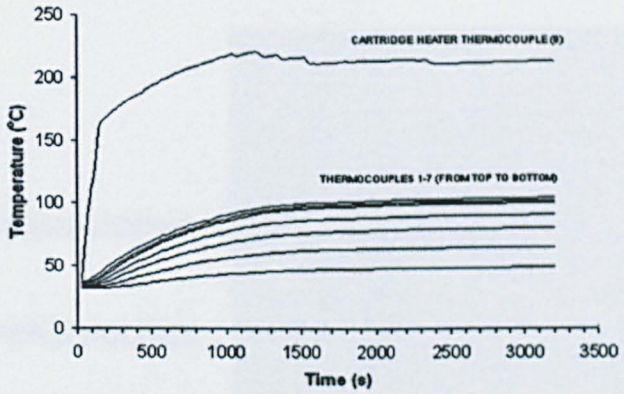

Figure 3.9 *Typical temperature plots of the cartridge heater and thermocouples 1 – 8 for one of the samples.*

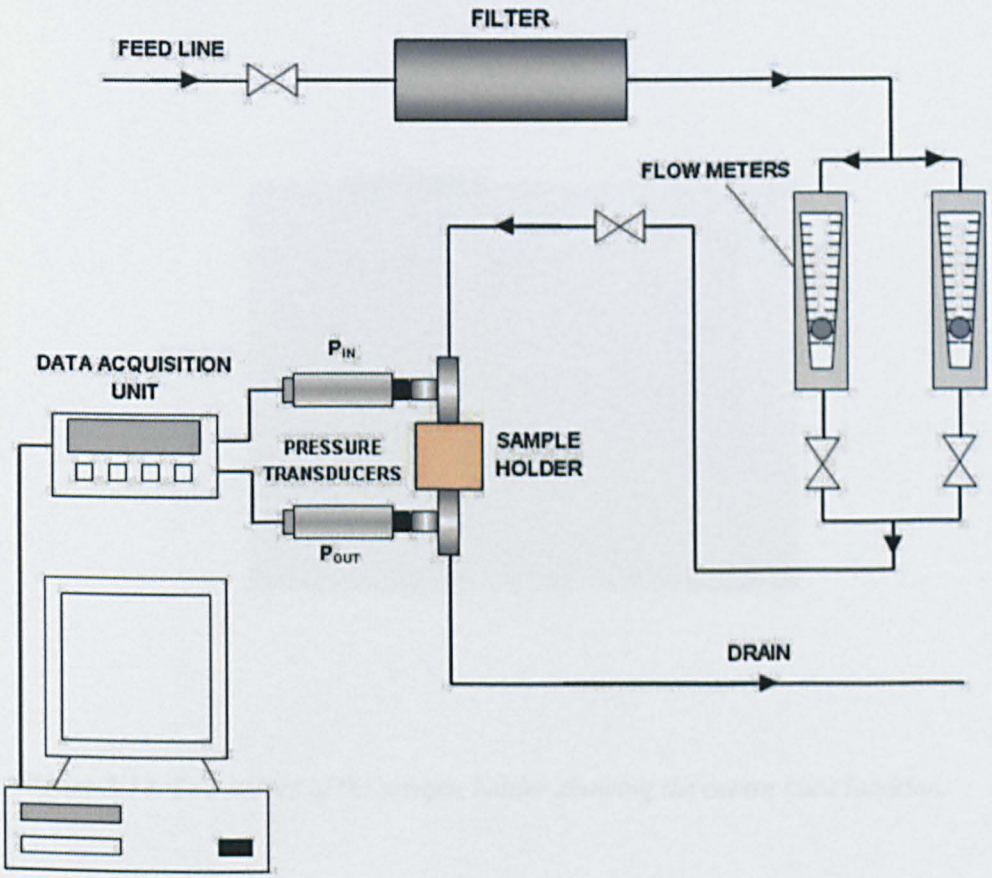

Figure 3.10 *Schematic diagram of the permeability test apparatus.*

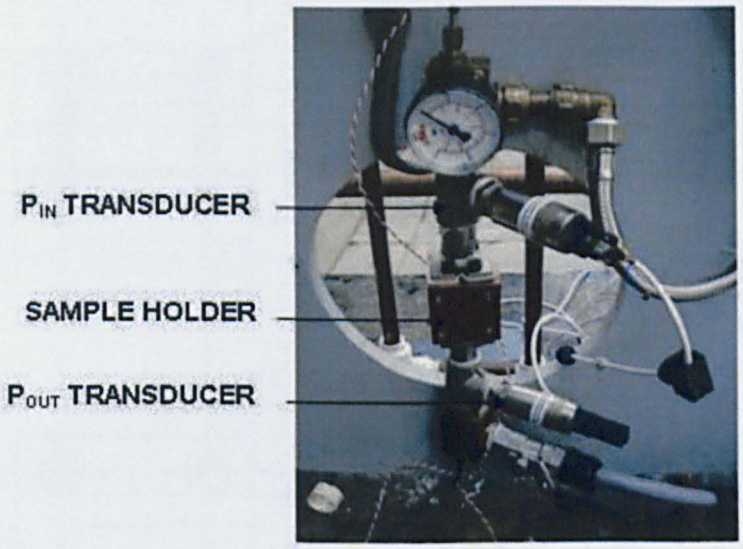

Figure 3.11 *Key components of the apparatus when fixed in series with the fluid flow.*

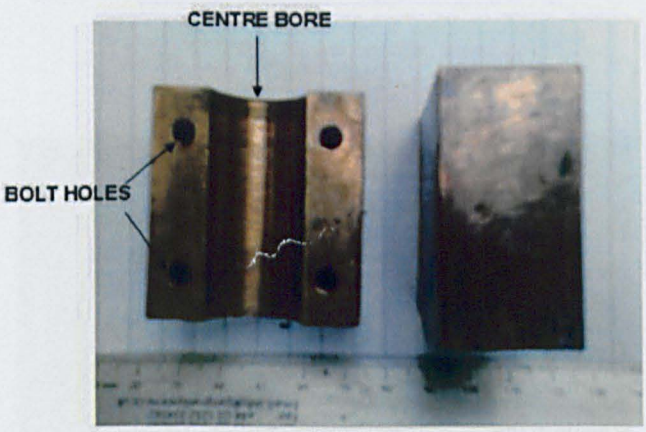

Figure 3.12 *Two halves of the sample holder showing the centre bore location.*

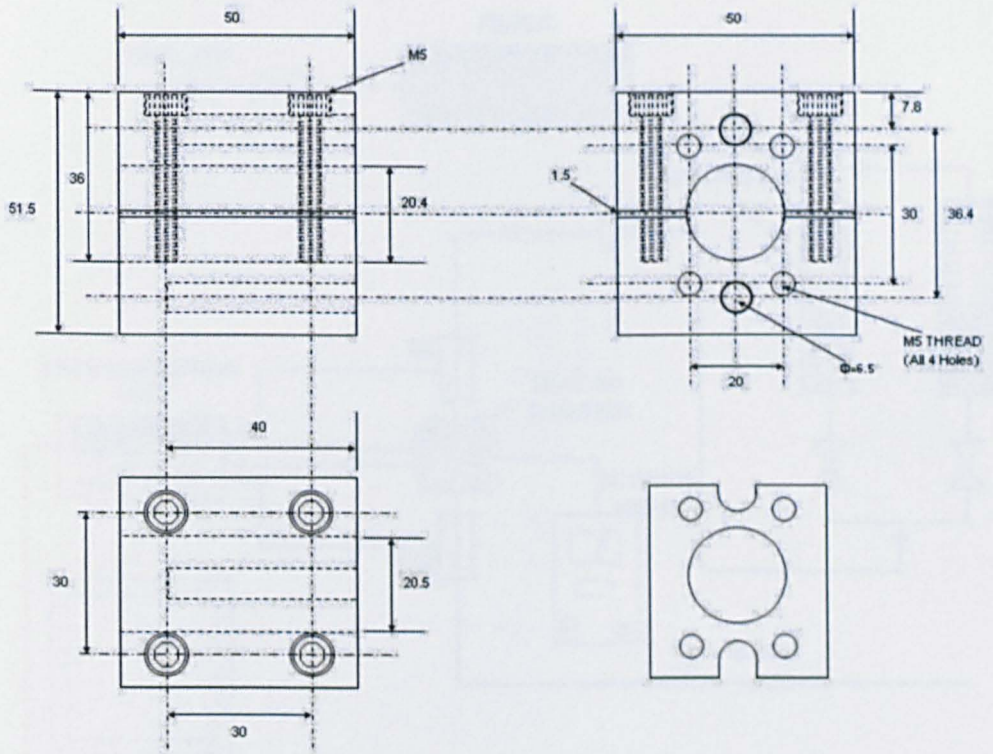

Figure 3.13 *Technical drawing of the sample holder.*

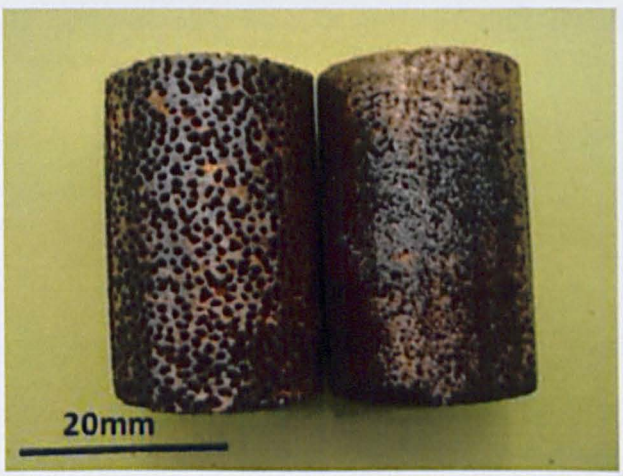

Figure 3.14 *Two heat transfer test samples.*

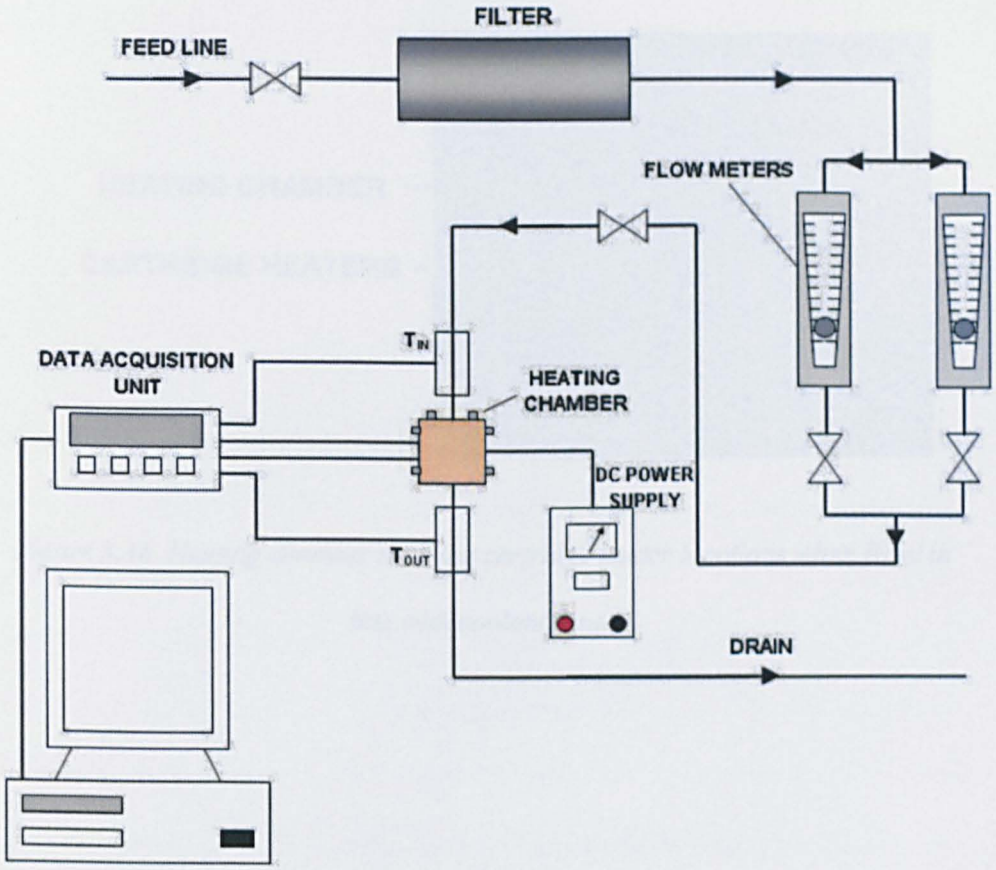

Figure 3.15 *Schematic diagram of the thermal transfer test apparatus.*

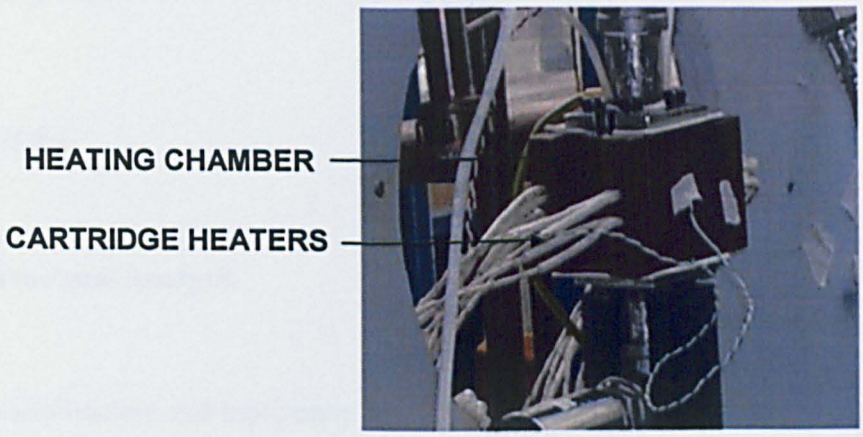

Figure 3.16 *Heating chamber showing cartridge heater locations when fixed in line with coolant flow.*

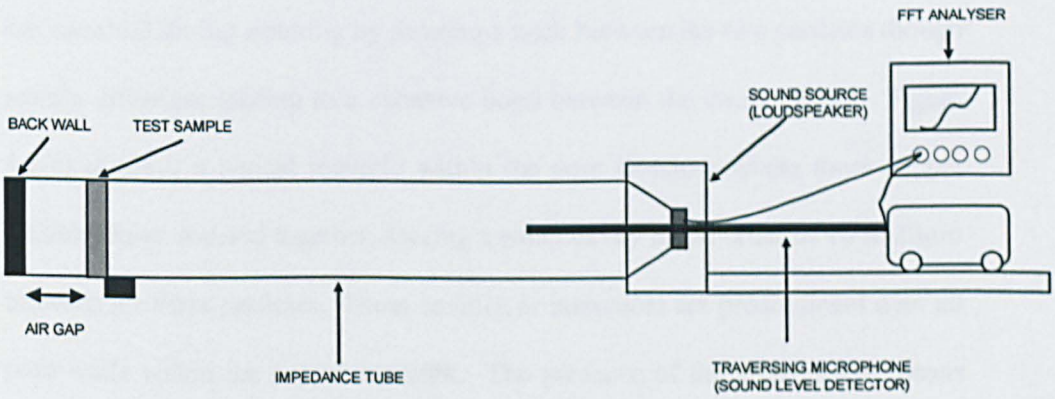

Figure 3.17 *Schematic diagram showing the basic experimental set up of the standing wave impedance tube method for measurement of the sound absorption coefficient.*

Chapter 4

RESULTS

4.1 Structural Analysis

The microstructure and topography of the LCS porous copper specimens were examined using SEM. The representative features of a typical specimen are shown in Figure 4.1. Figure 4.1(a) shows the surface of a single copper powder particle, contained within the copper structure after sintering. The spherical form and smooth surface is clearly visible. A thin oxide film can be seen on the surface of the particle. Figures 4.1(b, c and d) show how the copper particles have bonded together during sintering. Figure 4.1(d) demonstrates how densification has occurred during sintering by forming a neck between the two particles though atomic diffusion, leading to a cohesive bond between the two particles. Figure 4.1(c) displays a typical scenario within the pore structure where three copper particles have sintered together, leaving a small cavity in the order of 10 to 20μm between the three particles. These cavities or interstices are predominant over all pore walls within the copper network. The presence of these interstices means that pores are interconnected by vast numbers of channels, resulting in a high connectivity. Pores are also connected in a more obvious fashion, where two or more potassium carbonate granules were adjacent during compaction, as can be seen in Figures 4.1 (e, f, g and h). For samples with a higher porosity, connectivity between pores is extremely high.

Figure 4.1(g) clearly shows how the pore walls are composed of the individual sintered copper powder particles, resulting in an extremely high surface area of the matrix. The consequence is an almost nebulous appearance when viewed at medium magnification. The sample viewed in Figure 4.1 had a fairly high porosity of 73%. As a result, the connectivity between pores is relatively large so the pore shape is not so distinctive. In the samples with a lower porosity, the pores are connected by narrower channels and are clearly seen to reflect the shapes of the potassium carbonate particles.

4.2 Porosity and Specific Surface Area

The porosity of eight porous copper samples (A1 to A8) was measured using the point counting technique and the Archimedes method described in Section 3.2. In the point counting method, a grid was superimposed over each image so that the ratio of the number of points located in the pores, P_{PORE}, to the total number of testing points within the selected area, P_{TOT}, could be measured. From this ratio, the porosity of each sample could be calculated by Eq. (3.2). Table 4.1 summarises the data collected from the samples and compares the porosity values obtained using these two methods to the nominal or intended porosity values. The variation in measured porosities between the point counting method, Archimedes method and the nominal values are shown in Figure 4.2. The porosity measured using the point counting method is generally lower the porosity measured using Archimedes method. The latter is generally close to, and in most cases slightly lower than, the nominal value. All test samples had a diameter of 30mm and a length of 10mm.

Table 4.1: Summary of point counting data and measured porosity values in comparison with nominal values for Samples A1 to A8.

Sample Reference	Nominal Porosity (%)	Pore Size (μm)	P_{PORE}	P_{TOT}	Porosity by Point Counting (%)	Porosity by Archimedes Method (%)
A1	60	425-710	174	288	60.42	59.13
A2	65	425-710	176	288	61.11	62.34
A3	70	425-710	192	288	66.67	66.32
A4	75	425-710	204	288	70.83	76.9
A5	70	1000-1500	192	288	66.67	67.83
A6	70	710-1000	195	288	67.71	68.21
A7	70	250-425	193	288	67.01	69.02
A8	70	MIXED	186	288	64.58	68.25

The specific surface area (S_V) of samples A1 to A8 was obtained from the micrographs shown in Figure 3.6 (*a to h*), using the point counting method (Section 3.2). Table 4.2 summarises the data collected from the micrographs, together with the values calculated for S_V using Eq. (3.3). Column 4 shows the number of interceptions between pores and the test line (P_{TOT}), while column 5 represents the length of the test line (L). Sample A4, with the highest porosity shows the highest value of S_V, closely followed by sample A7, which has the smallest pore size of 250 – 425μm. Sample A5, with the largest pore size of 1000 – 1500μm shows the lowest value of S_V. Samples A3, A5, A6 and A7 show that S_V increases with decreasing pore size, while samples A1 to A4 show that S_V increases steadily with increasing porosity. Figures 4.3 and 4.4 present the data in Table 4.2 graphically, showing the variations of specific surface area with porosity and pore size, respectively.

Table 4.2: Summary of collected data and calculated specific surface areas of samples A1 to A8.

Sample Reference	Nominal Porosity (%)	Pore Size (μm)	P (total)	L (mm)	S_V (mm^2/mm^3)
A1	60	425-710	283	165.65	3.42
A2	65	425-710	302	151.2	3.99
A3	70	425-710	320	150	4.27
A4	75	425-710	345	156	4.42
A5	70	1000-1500	157	135.38	2.32
A6	70	710-1000	175	142.86	2.45
A7	70	250-425	368	166.82	4.36
A8	70	MIXED	184	147.06	2.5

4.3 Thermal Conductivity

The thermal conductivity of six porous copper test samples was measured using Corsan's method (Corsan 1984) as described in Section 3.3. The structural properties and the thermal conductivity values of the six samples are summarised in Table 4.3. The samples have different relative densities or different pore sizes. Sample B6 was manufactured by sintering a bulk of copper powder with no space holder, which was compacted and sintered under the same process parameters as the other five samples. The relative density was measured using Archimedes method. The variation in density along the length of the sample is less than 6% based on quantitative metallographic measurements.

Table 4.3 Structural characteristics and thermal conductivity of thermal conductivity samples.

Sample Reference	Relative Density	Porosity (%)	Pore Size (μm)	Thermal Conductivity ($Wm^{-1}K^{-1}$)
B1	0.21	79	710-1000	24.8
B2	0.26	74	1000-1500	46.9
B3	0.27	73	710-1000	46.3
B4	0.28	72	425-710	45.9
B5	0.36	64	710-1000	68.7
B6	0.78	22	-	178

Figure 4.5 shows the temperature gradients in the test samples and their corresponding comparators at steady-state temperatures in the range of 100 ± 6°C at thermocouple 1. The first three data points (up to 100mm from thermocouple 1) represent the temperature readings of the three thermocouples in the comparator. The remaining four data points represent the thermocouple temperature readings in the porous copper specimen. The change in temperature gradient is clearly visible between thermocouples 3 and 4, where the interface between the comparator and the test sample is. The plots in Figure 4.5 display linear temperature gradients in both the solid copper parts and the porous copper parts, with the interface clearly visible in each case. This demonstrates negligible radial heat losses at steady-state temperatures within the range of 100 ±6°C. The temperature gradients in samples B1 to B6 and their corresponding comparators are: -0.59, -0.04; -0.47, -0.06; -0.51, -0.06; -0.46, -0.06; -0.38, -0.07; and –0.21, -0.095 Km^{-1}; respectively. Using equation (3.3), the corresponding values for the thermal conductivity for samples B1 to

B6 were calculated to be 24.8, 46.9, 46.3, 45.9, 68.7 and 178.0 $Wm^{-1}K^{-1}$ respectively.

Samples B2, B3 and B4 all have relative densities between 0.26 and 0.28 and different pore sizes of 1000 – 1500μm, 710 – 1000μm and 425 – 710μm respectively. The results show that for a given relative density, the pore size only has a very slight effect on the thermal conductivity, with measured values varying between 45.9 $Wm^{-1}K^{-1}$ and 46.9 $Wm^{-1}K^{-1}$ for samples B2, B3 and B4. The thermal conductivity of a porous copper sample is mainly determined by its relative density, or porosity. The experimental data of thermal conductivities for samples B1 to B6, relative to that of copper, are plotted as a function of relative density in Figure 4.6.

Empirical correlation and modelling have shown that the relationship between the thermal conductivity and the relative density of the porous metal can be expressed by power law (Kovacik *et al* 1999).

$$\frac{\lambda}{\lambda_0} = \left(\frac{\rho}{\rho_0}\right)^n \tag{4.1}$$

where λ is the thermal conductivity of the porous metal, λ_0 is the thermal conductivity of the bulk material in the cell wall, ρ is the density of the porous metal, ρ_0 is the density of the bulk metal and n is the exponent for thermal conductivity. The thermal conductivity vs. relative density curve fitted to Eq. (4.1) is also shown in Figure 4.6. The power law with an exponent $n = 2.05$ describes the experimental data well.

4.4 Electrical Conductivity

The electrical conductivity of thirty porous copper test samples was measured using a Sigmatest 2.068 conductivity meter as described in Section 3.4. Table 4.4 lists the electrical conductivity values of the test samples. The samples have different relative densities or different pore sizes. Samples C29 and C30 were manufactured by compacting copper powder, with no space holder present in the compact. The compaction pressure was kept the same as with the other samples. The relative density of each sample was measured using Archimedes method. For convenience, the porosity of the samples was also listed in addition to pore size and relative density.

Table 4.4 Measured electrical conductivity values of porous copper samples with different relative densities and pore sizes.

Sample Reference	Pore Size (μm)	Relative Density	Porosity (%)	Electrical Conductivity (Sm^{-1})
C1	250-425	0.16	84	1.3
C2	250-425	0.28	72	3.4
C3	250-425	0.31	69	7.2
C4	250-425	0.35	65	8.8
C5	250-425	0.38	62	9
C6	250-425	0.47	53	11.1
C7	425-710	0.15	85	1
C8	425-710	0.2	80	2.5
C9	425-710	0.25	75	4.5
C10	425-710	0.3	70	6.9
C11	425-710	0.32	68	7.6
C12	425-710	0.37	63	9.9
C13	425-710	0.44	56	12.2
C14	425-710	0.5	50	13
C15	425-710	0.57	43	17.9
C16	710-1000	0.17	83	1.9
C17	710-1000	0.22	78	5.21
C18	710-1000	0.3	70	6.19
C19	710-1000	0.37	63	9.2
C20	710-1000	0.4	60	9.4
C21	710-1000	0.42	58	9.9
C22	710-1000	0.46	54	12.4
C23	710-1000	0.51	49	14.3
C24	1000-1500	0.16	84	1.7
C25	1000-1500	0.25	75	5.68
C26	1000-1500	0.37	63	10.15
C27	1000-1500	0.43	57	13.1
C28	1000-1500	0.49	51	13.4
C29	-	0.78	22	28.2
C30	-	0.82	18	36.2

Figure 4.7 shows the effects of relative density and pore size on the measured electrical conductivity. Values for the electrical conductivity range between 1 and 36.2 Sm^{-1} across all test samples, compared to 60 Sm^{-1} for the copper bulk material. The samples manufactured with no space holder present (C29 and C30) show superior electrical conduction to the rest of the samples. Sample

C15, with a pore size of 425 – 710μm and a relative density of 0.57 demonstrates the best electrical conduction from the twenty-eight samples manufactured with a space holder present, with a value of 17.9 Sm^{-1} being recorded. The results show that the electrical conductivity of porous copper is strongly dependant on the relative density, with pore size only having a small effect. Samples with higher pore size generally exhibit better electrical conduction than those with small pores, at a fixed relative density.

Empirically, the relationship between the electrical conductivity and the relative density of the porous metal follows a power law in a similar form as Eq. (4.1) (Ashby 2000). Figure 4.8 shows the relative electrical conductivity as a function of relative density. The curve can be seen to fit the power law, with a critical exponent of 2.46 describing the experimental data well. This is considerably larger than the exponent fitting the thermal conductivity results obtained using Corsan's method.

4.5 Permeability

The viscous permeability of twenty-two porous copper test samples, D1 to D22, was measured using an open flow apparatus described in Section 3.5.2. The structural properties and the viscous permeability coefficients of the six samples are summarised in Table 4.5. The length of each test sample was in the range of 23 to 31mm, with a diameter of 20.5 ± 0.3mm. Each sample was categorised according to its pore size and porosity. Three pore size ranges of 150 – 250μm, 425 – 710μm and 1000 – 1500μm were studied, with porosities ranging

between 52.5 and 82.5%. The porosity of each sample was measured using Archimedes method. At high porosities, the structural characteristics of samples with a pore size lower than 425μm are poor, causing structural collapse when a fluid pressure gradient was generated across them. For this reason, a maximum porosity of 77% was tested in the 150 – 250μm pore size range. Sample D22 contained irregular shaped pores, whose size was in the region of 2 – 3mm. This sample was included for comparison purposes with the spherical pores of samples D1 to D21. The pore structure and size was checked using microscopic analysis, with no significant defects or contamination observed.

Table 4.5 Viscous permeability coefficients of samples with different structural characteristics.

Sample Reference	Pore Size (μm)	Relative Density	Porosity (%)	Permeability ($x10^{-10}m^2$)
D1	150 - 250	0.48	52.5	0.208
D2	150 - 250	0.46	53.8	0.372
D3	150 - 250	0.38	61.7	0.833
D4	150 - 250	0.29	70.6	1.701
D5	150 - 250	0.23	77	2.909
D6	425 - 710	0.47	53.4	0.048
D7	425 - 710	0.45	54.8	0.127
D8	425 - 710	0.40	59.7	0.173
D9	425 - 710	0.39	61.2	0.301
D10	425 - 710	0.36	63.7	0.404
D11	425 - 710	0.31	69.2	0.658
D12	425 - 710	0.29	71.4	1.224
D13	425 - 710	0.27	72.8	1.725
D14	425 - 710	0.17	82.8	7.505
D15	1000 - 1500	0.42	57.8	0.042
D16	1000 - 1500	0.37	62.6	0.181
D17	1000 - 1500	0.36	63.8	0.157
D18	1000 - 1500	0.30	69.8	0.403
D19	1000 - 1500	0.28	72	0.817
D20	1000 - 1500	0.24	76.5	3.631
D21	1000 - 1500	0.18	82.5	11.502
D22	2000 – 3000 (Angular)	0.24	76.1	3.089

Figure 4.9 shows graphically the variations of pressure drop with coolant flow rate for samples with different porosities and different pore sizes. The graphs are split into three porosity ranges. Figure 4.9(a) shows the pressure drop across samples with the lowest porosities up to 61.7%, Figure 4.9(b) shows samples whose porosity varies between 62.6 and 71.4% and Figure 4.9(c) shows samples with porosities greater than 72%. It is shown that samples with

the highest porosity show the lowest pressure drops at any given flow rate. The sample which generated the lowest pressure drop is D14, which has the highest porosity of 82.8% and a medium pore size of 425 – 710μm. Sample D21 produced almost the same pressure drops, with 0.075 N/mm^2 at a flow rate of 10 l/min. Of all the samples, D6 and D15, which have low porosities, generated the highest pressure drops at any given flow rate with a maximum of 0.29 N/mm^2 at 0.6 l/min. Figure 4.9(c) shows that at a given porosity, sample D22 with the irregular pore shape generates a larger pressure drop. Figure 4.10 shows the variations of pressure drop with coolant flow rate for samples with a similar porosity but different pore sizes. For a given porosity, the pressure drop generated by the sample reduces significantly as the pore size decreases.

The viscous permeability coefficient value for each sample was calculated from the pressure drops by applying equation (3.7). Figure 4.11 shows the variation of viscous permeability coefficient with porosity at different pore sizes. The viscous permeability coefficient is mainly affected by porosity, although pore size also has some influence. The graph shows an exponential rise in viscous permeability coefficient with porosity. Sample D21, with the highest porosity and largest pore size, displays the highest permeability coefficient. Sample D14, with a similar porosity as D21 but a smaller pore size, only produces a permeability coefficient approximately two thirds that of sample D21. At porosities below 75%, samples with the larger pore size show lower permeability values. Above 75% porosity, samples with larger pore sizes show a much more rapid increase in permeability than smaller pore sizes. The pore

shape does not seem to have any significant effect on the viscous permeability coefficient.

4.6 Heat Transfer

The heat transfer coefficient of a series of seventeen porous copper samples was measured using an open-flow heating apparatus described in Section 3.6.1. A summary of the structural characteristics and preform compaction pressure of each test sample is presented in Table 4.6. The test samples demonstrated good homogenous pore distribution and structure, with no contamination observed on any surfaces when examined under an optical microscope. Sample lengths were in the range of 21 to 31mm, with diameters in the range of 20.5 ± 0.3mm. The effects of pore size, porosity, preform compaction pressure, heat power input and coolant flow rate on the heat transfer coefficient were compared. Three pore size ranges were tested: 150 – 250μm, 425 – 710μm and 1000 – 1500μm. Porosities ranged between 53.4% in sample E3 and 81% in sample E17. The porosity of each sample was measured using Archimedes method. The preform compaction pressure in samples E1 to E13 was 200MPa, while 300MPa was used for samples E14 to E17.

Table 4.6 Structural characteristics and compaction pressures of the samples used for heat transfer coefficient measurements.

Sample Reference	Pore Size (μm)	Relative Density	Porosity (%)	Compaction Pressure (MPa)
E1	150 - 250	0.38	61.7	200
E2	150 - 250	0.29	70.6	200
E3	425 - 710	0.47	53.4	200
E4	425 - 710	0.45	54.8	200
E5	425 - 710	0.45	59.7	200
E6	425 - 710	0.40	61.2	200
E7	425 - 710	0.39	63.7	200
E8	425 - 710	0.36	69.3	200
E9	425 - 710	0.29	71.4	200
E10	425 - 710	0.27	72.8	200
E11	425 - 710	0.17	82.8	200
E12	1000 - 1500	0.37	62.6	200
E13	1000 - 1500	0.28	72.0	200
E14	150 - 250	0.30	70.0	300
E15	425 - 710	0.37	63.4	300
E16	425 - 710	0.28	71.6	300
E17	425 - 710	0.19	81.0	300

The convection heat transfer coefficient and Nusselt number were used to characterise the heat transfer performance of the test samples with the coolant flowing through them. They were calculated by applying Eq. (3.8) and Eq. (3.11) under each process condition.

Figure 4.12 shows the effect of porosity on the heat transfer coefficient at various coolant flow rates. At any given coolant flow rate, the heat transfer coefficient generally decreases with porosity in all samples tested. The maximum value for the heat transfer coefficient observed is 36.9 kW/m^2K^{-1} at a flow rate of 2 l/min in sample E3, which has the lowest porosity. The lowest value observed is 7.69 kW/m^2K^{-1} at a flow rate of 0.4 l/min in sample E10,

which has a high porosity. However, a significant peak in the heat transfer coefficient can be observed in Sample E6, which has a porosity of 61.2%.

Figures 4.13 and 4.14 show the effect of coolant flow rate on the heat transfer coefficient and Nusselt number respectively. The heat transfer coefficient and Nusselt number both increase almost linearly with increasing flow rate. It is clearly seen that the flow rate dominates heat transfer across all porosities.

Figures 4.15 and 4.16 demonstrate the effect of pore size on the heat transfer coefficient and Nusselt number, where samples E2, E9 and E14 are compared. For porous copper samples with a similar porosity, the heat transfer performance increases with increasing pore size, for any given coolant flow rate. Sample E14, with the largest pore size of 1000 – 1500μm, demonstrates the best heat transfer properties, while sample E2, with the smallest pore size of 150 – 250μm, shows the worst characteristics.

Figures 4.17 and 4.18 show the effect of compaction pressure used in manufacturing the porous copper samples on the heat transfer coefficient, displayed with varying porosity and flow rate respectively. The graphs show that a higher compaction pressure gives rise to better heat transfer characteristics for each sample tested. At any given flow rate, the heat transfer coefficient is approximately 25% higher when the higher compaction pressure of 300MPa is used during the manufacturing process.

Figures 4.19 (a) to (q) display the variation of the heat transfer coefficient and coolant flow rate for all samples, including the condition where no sample was present in the heating chamber. The effect of heat input power on heat transfer for samples E1 to E13 is shown in Figure 4.23 (a) to (m). Generally, the heat input power has little effect on the heat transfer coefficient, particularly at lower flow rates (less than 2 l/min). Samples E2, E5, E8, E9, E11, E14, E15 and E17 all show a characteristic peak in the heat transfer coefficient at various flow rates above 2 l/min. Beyond this peak, the heat transfer begins to diminish. A good example of this behaviour is shown in Figures 4.23 (n), (o) and (q). The maximum heat transfer coefficient (34.5 kW/m^2K^{-1}) was displayed by sample E16, which was produced at a compaction pressure of 300MPa and has a porosity of 71.6% and pore size of 425 – 710μm, at a coolant flow rate of 3 l/min. Sample E11, which was produced at a compaction pressure of 200MPa and has a porosity of 82.8% and pore size of 425 – 710μm, displayed the worst heat transfer performance. It had a maximum heat transfer coefficient of 12.4 kW/m^2K^{-1}, at a flow rate of 3 l/min. When no sample was present in the heating chamber (Figure 4.23 (r)), the heat transfer coefficient is low at all flow rates tested and remains below 5.5 kW/m^2K^{-1}.

4.7 Acoustic Absorption

4.7.1 Samples

The acoustic performance of sixteen porous copper test samples, F1 to F16, was measured using the standing wave tube method described in Section 3.7.1. Table 4.7 summarises the structural properties and size of the samples. pore size, relative density, porosity and diameter of each test sample. Each sample tested had different pore size, porosity or sample diameter. The pore size ranges used were: 250 – 425μm (F1 and F2), 425 – 710μm (F3 to F10), 710 – 1000μm (F11 and F12), 1000 – 1500μm (F13 and F14), and a combination of 425 – 710μm and 1000 – 1500μm (F15 and F16). Porosities ranged from 59.1% to 75.1%. The porosity of each sample was measured using Archimedes principle. Each sample had a thickness of 10 ± 0.5mm and a diameter of either 100mm or 30mm, for low or high frequency tests respectively. Microscopic analysis showed that all the samples exhibited good pore structure, minimal surface defects and a uniform pore distribution. For each sample, the acoustic absorption coefficient was measured in three different conditions: with no air gap, with a 20mm air gap or with a 50mm air gap between the sample and the tube end.

Table 4.7 Structural characteristics of samples F1 to F16 for acoustic tests.

Sample Reference	Pore Size (μm)	Relative Density	Porosity (%)	Diameter (mm)
F1	250-425	0.30	70.4	100
F2	250-425	0.32	69.2	30
F3	425-710	0.25	75.1	100
F4	425-710	0.28	71.8	100
F5	425-710	0.36	64.9	100
F6	425-710	0.42	59.2	100
F7	425-710	0.28	74.2	30
F8	425-710	0.34	69.3	30
F9	425-710	0.38	63.9	30
F10	425-710	0.41	59.1	30
F11	710-1000	0.32	68.8	100
F12	710-1000	0.32	69.4	30
F13	1000-1500	0.32	70.1	100
F14	1000-1500	0.32	69.9	30
F15	425-710/1000-1500 MIXED	0.31	69.2	100
F16	425-710/1000-1500 MIXED	0.32	70.2	30

4.7.2 No Air-Gap

Figure 4.20 shows the effect of porosity on the sound absorption coefficient at frequencies between 100 and 1000Hz, measured with no air gap between the samples and the back plate. The sound absorption coefficient has an approximate value of 0.1 between 100Hz and 1000Hz. At these frequencies, the sound absorption coefficient is always below 0.5, rising slightly towards a frequency of 1000Hz. The porosity shows no significant effect on the sound absorption

coefficient within this frequency range. The significant peaks that occur in all samples between 0Hz and 100Hz can be attributed to equipment errors and can be ignored.

Figure 4.21 shows the effect of porosity on the acoustic absorption coefficient within a frequency range of 500 to 5000Hz, measured with no air gap between the samples and the back plate. The absorption coefficient increases significantly at these higher frequencies. The maximum absorption coefficient of 0.996 was observed at a frequency of 5000Hz for sample F9, which has a porosity of 63.9%. Sample F7, with the highest porosity of 74.2%, shows the weakest acoustic absorption characteristics up to a frequency of 4100Hz. At this point, sample F10, with the lowest porosity of 59.1%, becomes the poorer absorber. Crossover effects can be seen at various frequencies, showing that there is a complex relationship between porosity and the acoustic absorption coefficient. Furthermore, there are two significant drops in the absorption coefficient in all samples at frequencies of 2900 and 3700Hz.

Figure 4.22 shows the effect of pore size on the absorption coefficient at frequencies between 100 and 1000Hz, measured with no air gap between the samples and the back plate. Again all samples display weak absorption characteristics at these low frequencies, with no obvious relationship between pore size and the absorption coefficient observed.

Figure 4.23 shows the effect of pore size on the absorption coefficient at frequencies between 500 and 5000Hz, measured with no air gap between the samples and the back plate. Within this frequency range, pore size has some considerable effect on the sound absorption coefficient. Samples with a higher pore size show higher values for the sound absorption coefficient at frequencies between 3700 and 4000Hz. At this point, the absorption coefficient for sample F14, with the largest pore size, begins to drop and it becomes the poorest absorber. The absorption coefficient for sample F2, with the smallest pore size, continues to rise and becomes the best acoustic absorber at a frequency of 5000Hz, where the absorption coefficient is 0.992. Sample F16, with the mixed pore sizes, shows good acoustic absorption properties at frequencies above 4000Hz when compared to the other test samples. Two significant drops in the absorption coefficient can again be seen at frequencies between 2900 and 3800Hz with all pore sizes. All samples show similar trends in the sound absorption coefficient as a function of frequency, with the peaks occurring at slightly different frequencies, leading to crossovers at high frequencies.

The overall acoustic performance can be assessed using the Noise Reduction Coefficient (NRC). This is calculated as the arithmetic mean of the sound absorption coefficient at frequencies of 250, 500, 1000 and 2000Hz (Bell 1982). The half-width of the resonant peak is defined as the width of the frequency band of the sound absorption peak at an absorption coefficient of 0.5 (Han *et al* 2003). The mean absorption coefficient has also been calculated for all the 8 conditions (16 samples) between the frequencies of 100 and 5000Hz. A summary of the

acoustic characteristics of all the conditions when backed with no air gap is given in Table 4.8.

Table 4.8 Characteristic parameters of acoustic absorption curves.

Sample reference	Pore Size (μm)	Average Porosity (%)	NRC	Mean Absorption Coefficient	Peak Absorption Coefficient	Half-width of resonant peak (Hz)
F1/F2	250 - 425	69.8	0.16	0.47	0.996 @ 4975Hz	>1880
F4/F8	425 - 710	70.6	0.18	0.53	0.938 @ 3800Hz	>2020
F11/F12	710 - 1000	69.1	0.20	0.54	0.984 @ 4325Hz	>2000
F13/F14	1000 - 1500	70.0	0.18	0.54	0.979 @ 3662Hz	>2550
F15/F16	425 - 710/1000 - 1500	69.7	0.18	0.51	1.000 @ 4712Hz	>1980
F3/F7	425 - 710	74.7	0.17	0.40	0.944 @ 4962Hz	>1300
F5/F9	425 - 710	64.4	0.21	0.50	0.999 @ 4925Hz	>1930
F6/F10	425 - 710	59.2	0.23	0.48	0.827 @ 3637Hz	>2120

Figures 4.24 and 4.25 show the NRC as a function of porosity and pore size, respectively. The NRC increases steadily between porosities of 59.1 and 74.2%, with values ranging between 0.17 and 0.23. The NRC increases with increasing pore size between nominal pore sizes of 338μm and 855μm, at which point the NRC begins to decrease. The NRC is generally low at all porosities and pore sizes, varying between 0.16 and 0.23.

A better indication of the general absorption performance over the complete frequency band tested is the mean absorption coefficient. This varies between 0.47 and 0.54 across all porosities and pore sizes. When backed with no air gap, all samples show a half-width of the resonant peak greater than 1300Hz, with sample F14 showing an effective range greater than 2550Hz. The peak absorption coefficient for each sample occurs at frequencies above 3500Hz and

the resonant peak for all samples is at a frequency above 2400Hz. This confirms that the porous copper samples display better absorption characteristics at higher frequencies, with no air gap present.

4.7.3 Effect of Air Gaps

With the introduction of a 20mm air-gap behind the samples, the characteristics of the sound absorption coefficients change significantly, as shown in Figure 4.26. The sound absorption coefficients peak at a lower frequency than when no air-gap is present, between 1600 and 2300Hz. After the peak, the coefficient falls steadily to a frequency of about 4000Hz, at which point the sound absorption plateaus somewhat.

The effect of porosity on the sound absorption coefficient can be seen by comparing samples F7 and F8. Both samples tested again display broad peaks. At a frequency of approximately 4000Hz, the acoustic absorption coefficients level out and oscillate around 0.5. Sample F7, with a porosity of 74.2%, is generally a more efficient acoustic absorber than sample F8, with a lower porosity of 69.3%, when backed by a 20mm air gap.

The effect of pore size on the acoustic absorption coefficient can be seen by comparing samples F2 (250 – 425μm), F8 (425 – 710μm), F12 (710 – 1000μm), F14 (1000 – 1500μm) and F16 (425 – 710μm/ 1000 – 1500μm). The samples

with the larger pore sizes are the better sound absorbing properties until they hit their peak absorption. After the peaks, the acoustic absorption properties reverse and the samples with the smallest pore sizes become the best absorbers. Dips in the sound absorption coefficient occur in all samples at frequencies in the range of 3000 to 4000Hz. There are also slight peaks at frequencies between 4000 and 4500Hz.

Figure 4.27 shows the acoustic absorption as a function of frequency when an air gap of 50mm is introduced behind the test samples. There are two prominent peaks in the sound absorption coefficient, occurring at frequencies of approximately 1300 and 4500Hz in all test samples. The trough between the two peaks occurs between 3000 and 3700Hz. In general, sample F14, with the largest pore-size of 1000 – 1500μm, exhibits the poorest sound absorbing properties, while sample F2, with the smallest pore size of 250 – 425μm, displays enhanced absorption characteristics. An increase in porosity also leads to higher acoustic absorption coefficients at frequencies between 1000 and 5000Hz.

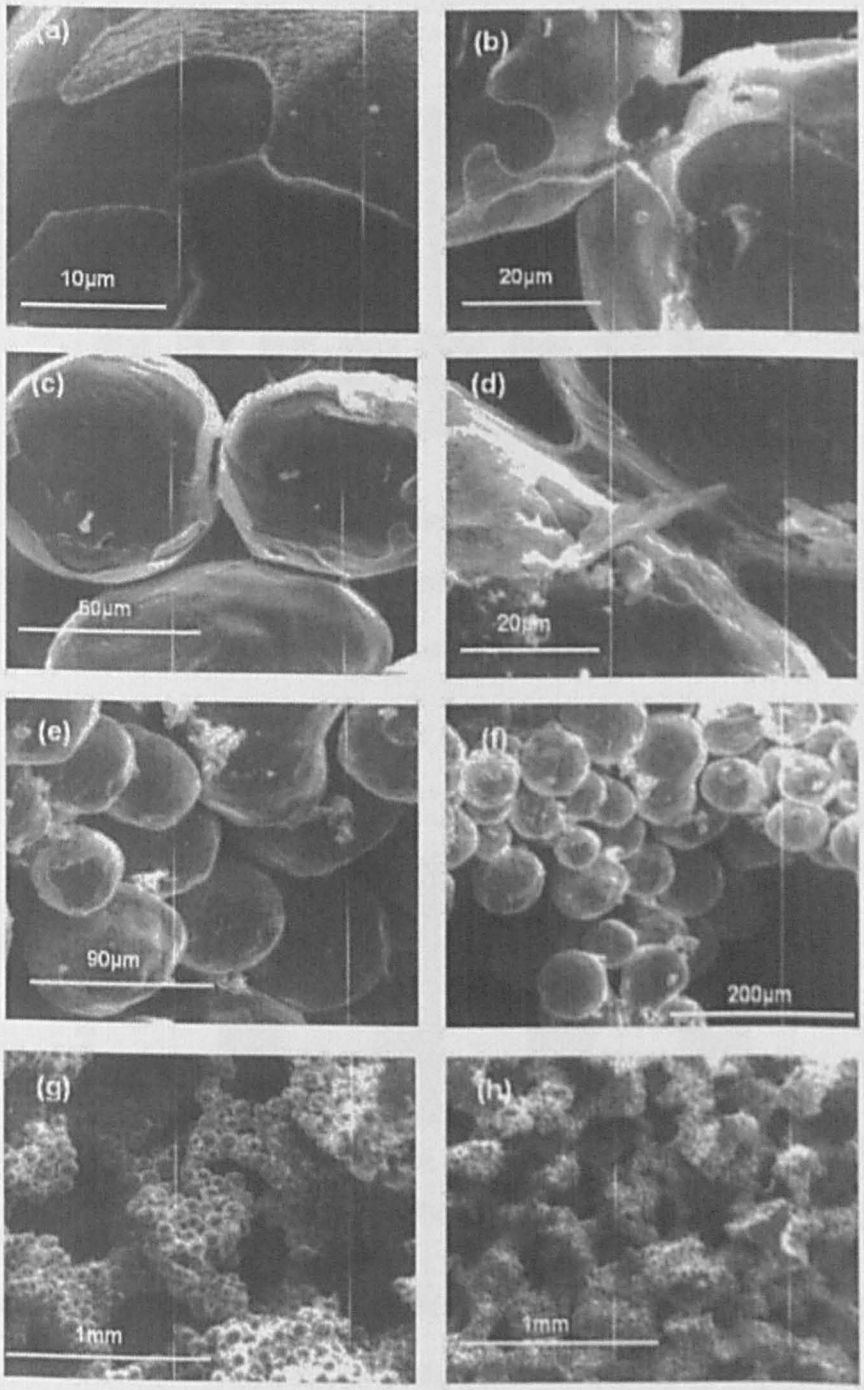

Figure 4.1 *SEM micrographs of an LCS copper sample showing representative features.*

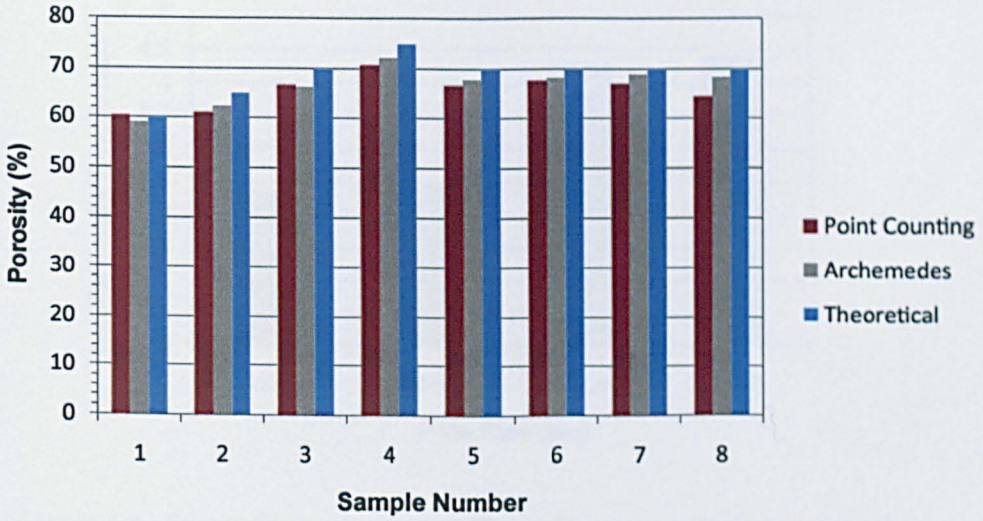

Figure 4.2 Variation of porosity between the point counting method, Archimedes method and the nominal value for samples A1 to A8.

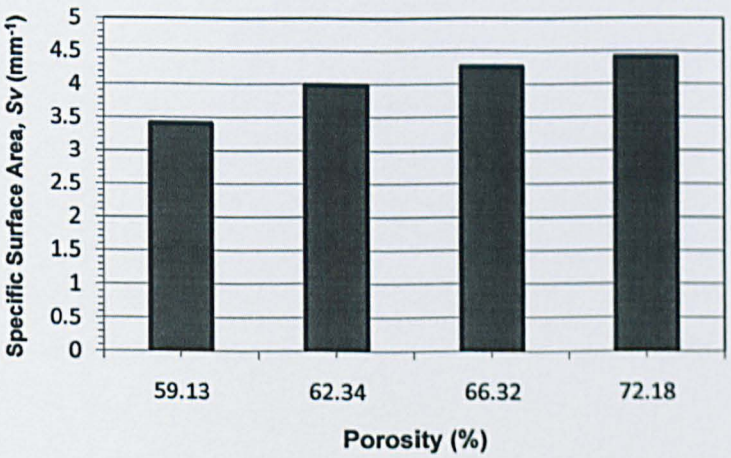

Figure 4.3 Effect of porosity on specific surface area, with fixed pore size 425-710μm.

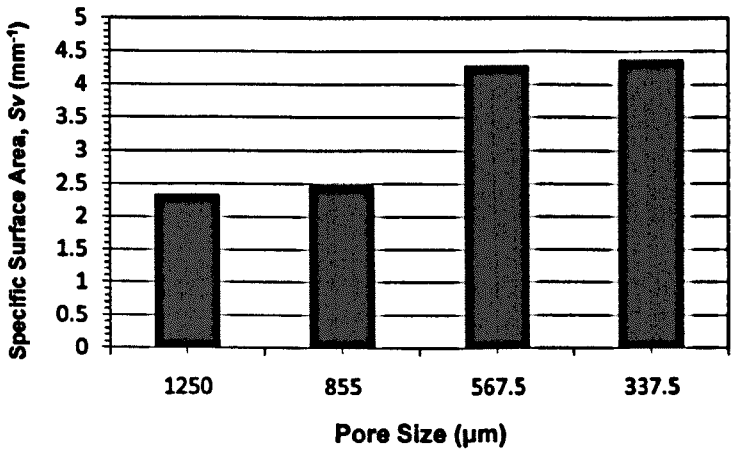

Figure 4.4 *Effect of pore size on specific surface area, with fixed nominal porosity of 70%.*

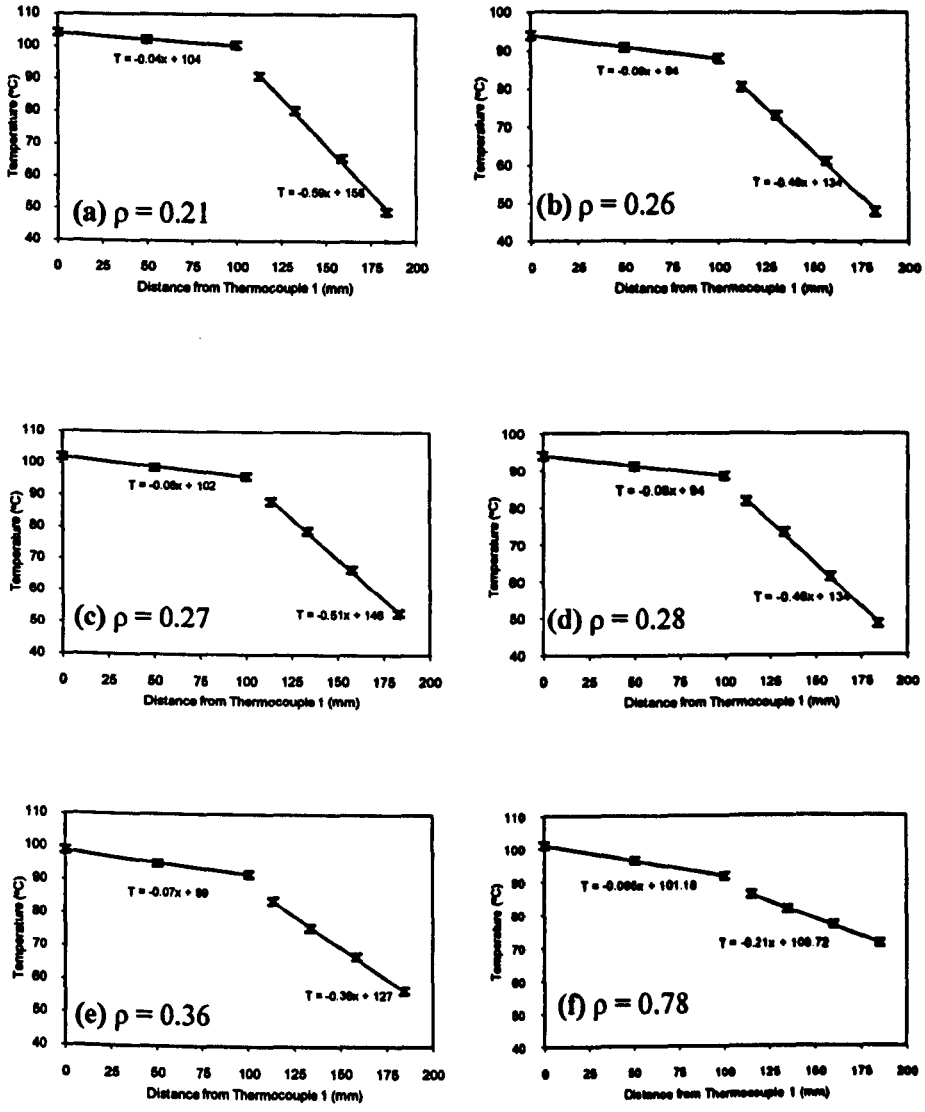

Figure 4.5 Temperature gradients in the solid copper comparators and the porous copper samples B1 (a), B2 (b), B3 (c), B4 (d), B5 (e) and B6 (f).

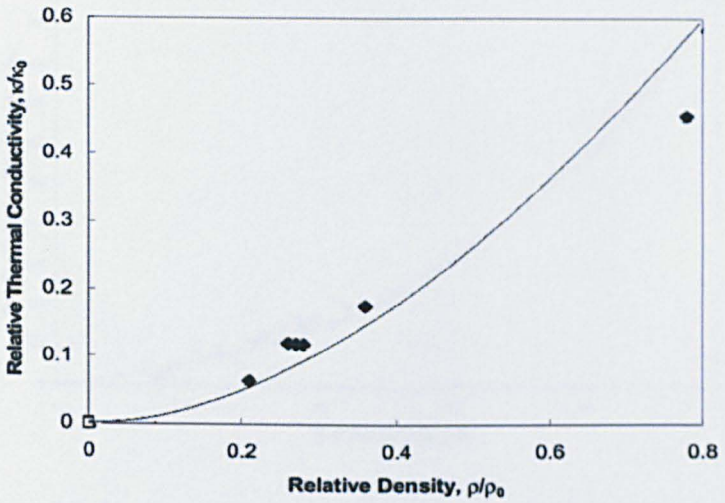

Figure 4.6 *Variation of relative thermal conductivity with relative density.*

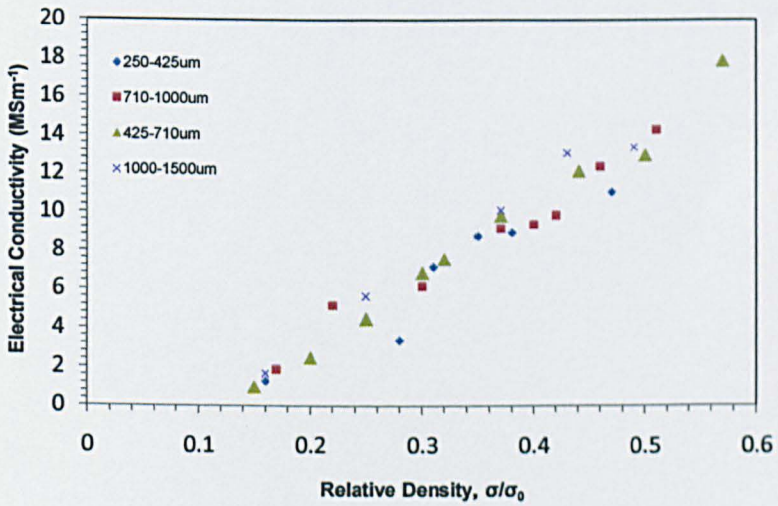

Figure 4.7 *Effect of pore size and relative density on electrical conductivity.*

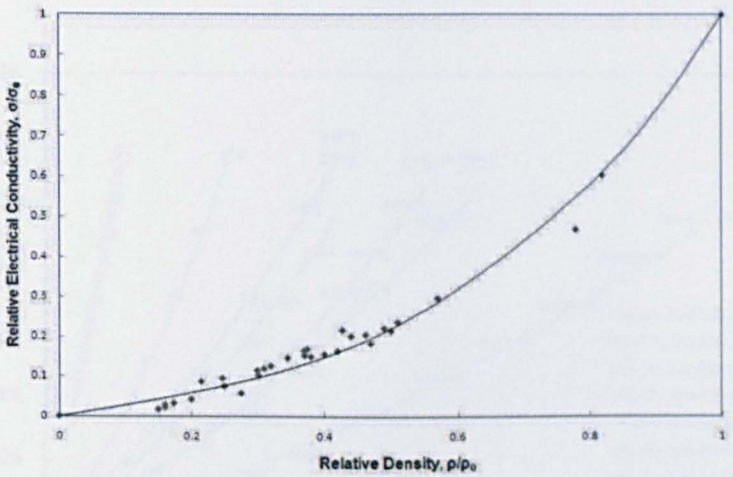

Figure 4.8 *Variation of electrical conductivity with relative density.*

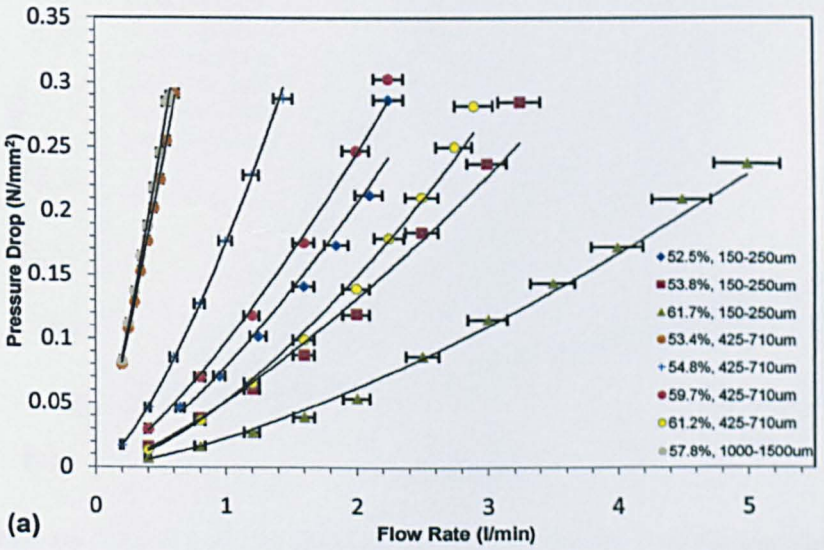

(a)

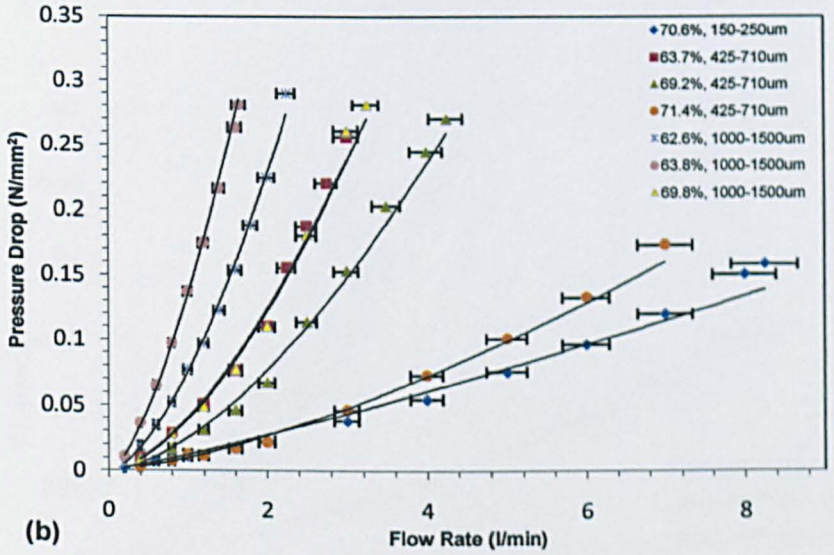

(b)

Figure 4.9 be continued

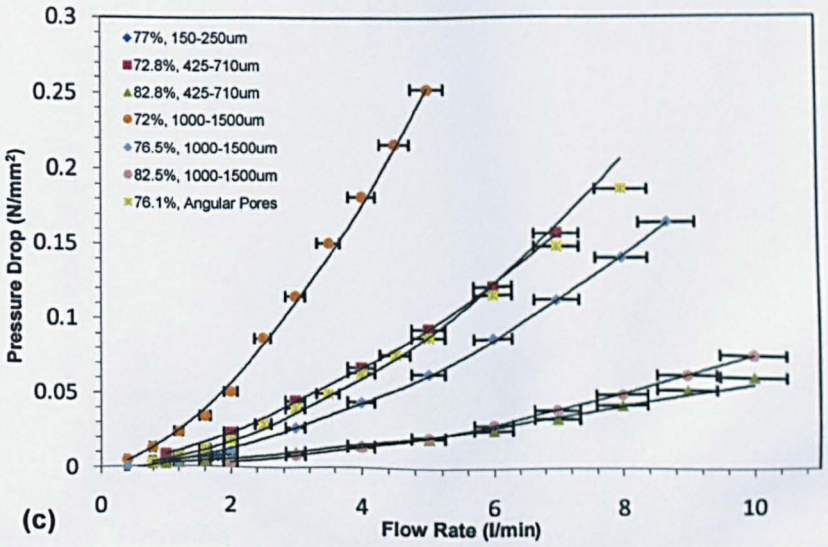

Figure 4.9 *Variation of pressure drop with coolant flow rate for samples with (a) low, (b) medium and (c) high porosities and different pore sizes.*

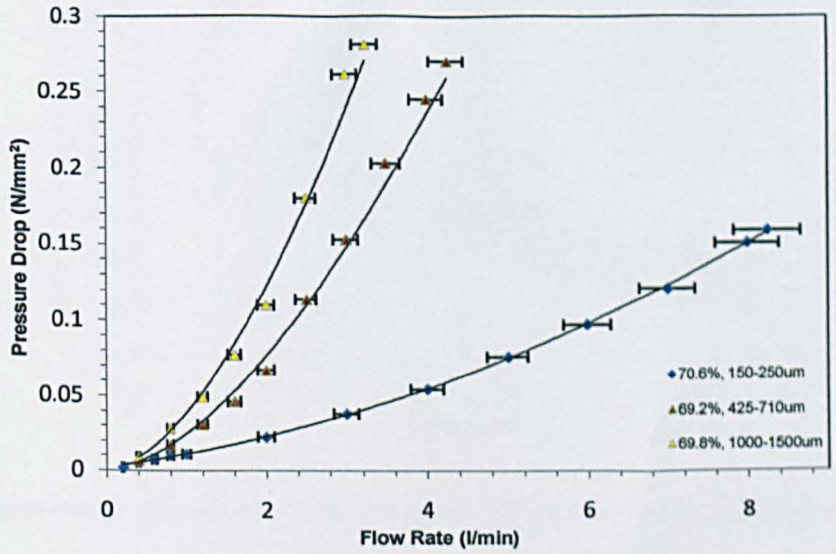

Figure 4.10 *Variation of pressure drop with coolant flow rate for samples with different pore sizes.*

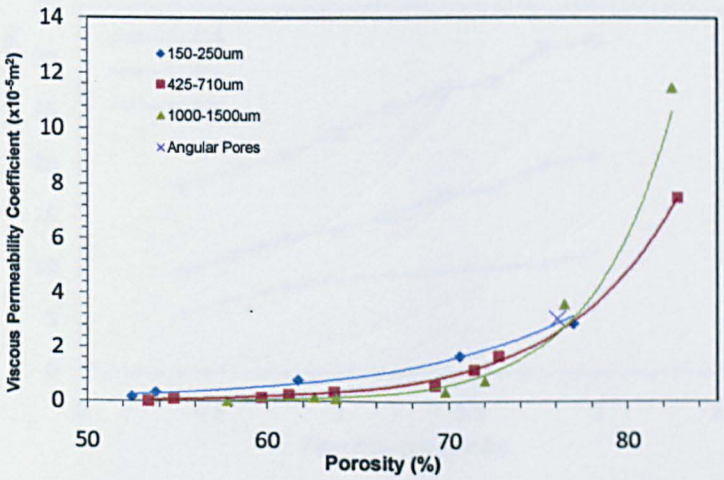

Figure 4.11 *Variation of the viscous permeability coefficient with porosity for samples with different pore sizes or shapes.*

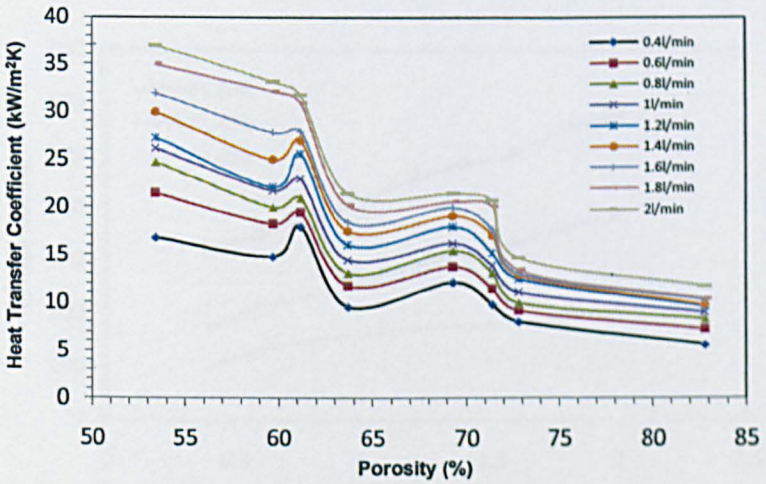

Figure 4.12 *Variation of heat transfer coefficient with porosity at different flow rates (Heat power input: 350W; Pore size: 425 – 710μm; Compaction pressure: 200MPa).*

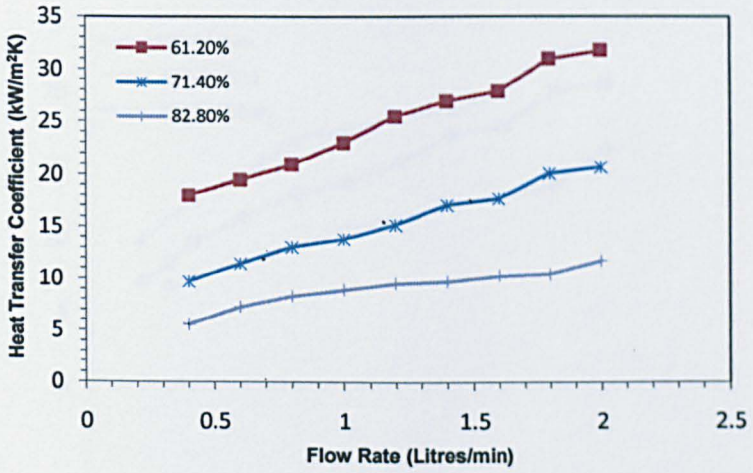

Figure 4.13 *Variation of heat transfer coefficient with coolant flow rate for samples with different porosities (Heat power input: 350W; pore size: 425 – 710μm; Compaction pressure: 200MPa).*

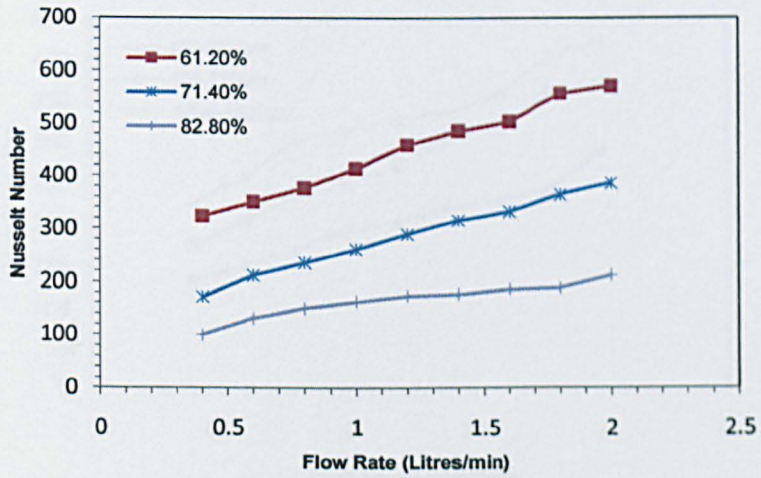

Figure 4.14 *Variation of Nusselt Number with flow rate for samples with different porosities (Heat power input: 350W; pore size: 425 – 710μm; Compaction pressure: 200MPa).*

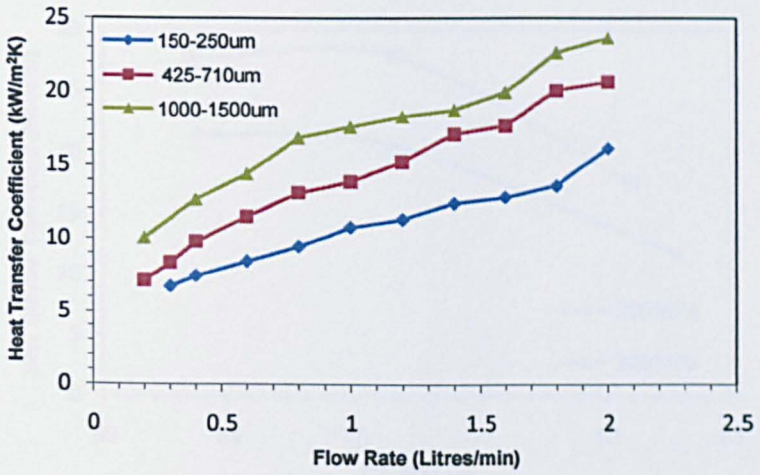

Figure 4.15 *Variation of heat transfer coefficient with coolant flow rate for samples with a similar porosity but different pore sizes (Heat power input: 350W; Porosity: 70 ± 1.4% ; Compaction pressure: 200MPa).*

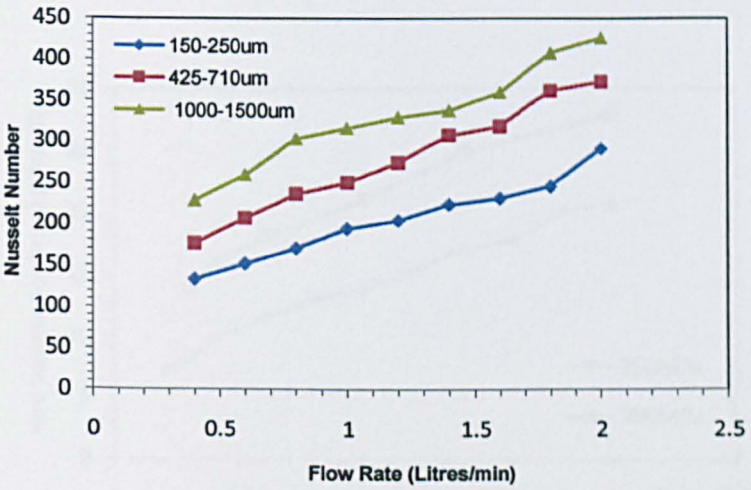

Figure 4.16 *Variation of Nusselt Number with coolant flow rate for samples with a similar porosity but different pore sizes (Heat power input: 350W; Porosity: 70 ± 1.4%; Compaction pressure: 200MPa).*

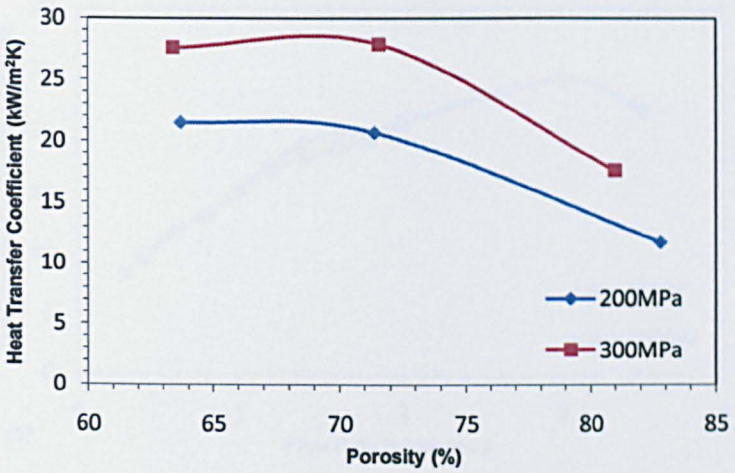

Figure 4.17 *Effect of compaction pressure used in manufacturing the porous copper samples on the heat transfer coefficient for samples with different porosities (Heat power input: 350W; Flow rate: 2 l/min; Pore size: 425 – 710μm).*

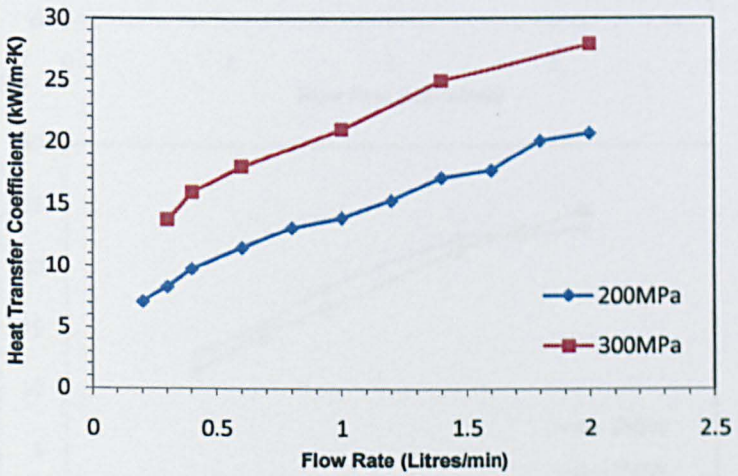

Figure 4.18 *Effect of compaction pressure used in manufacturing the porous copper samples on the heat transfer coefficient at different flow rates (Heat power input: 350W; Porosity 71.4%; Pore Size: 425 – 710μm).*

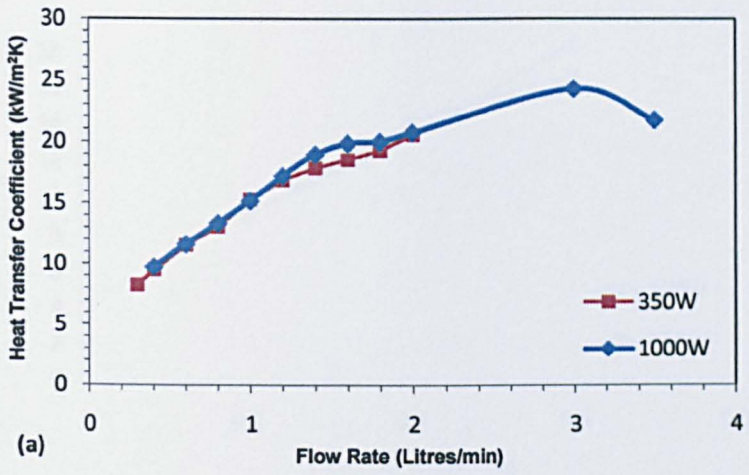

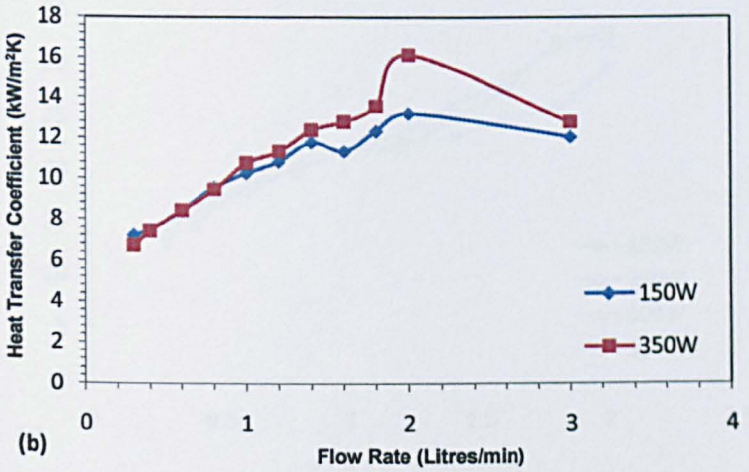

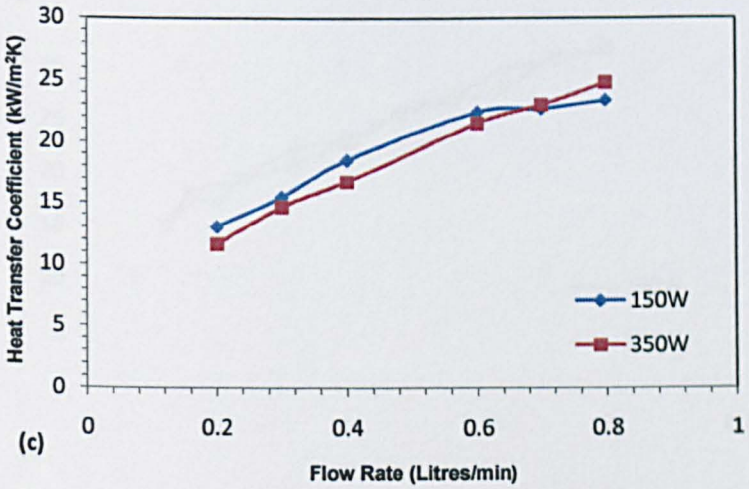

Figure 4.19 to be continued

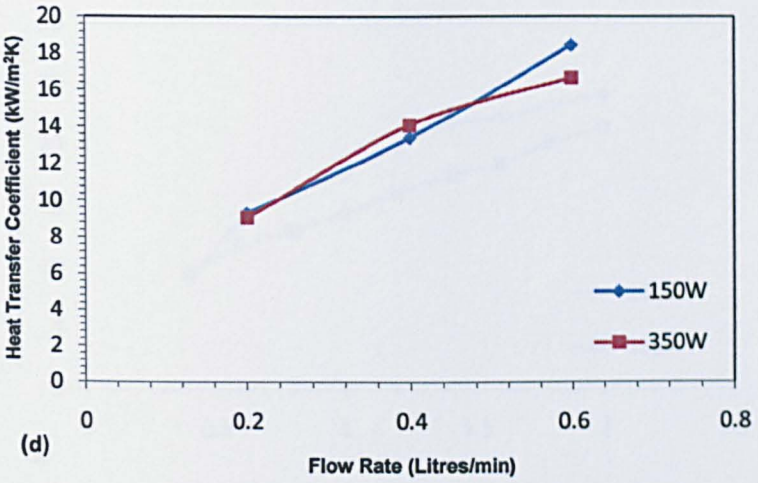

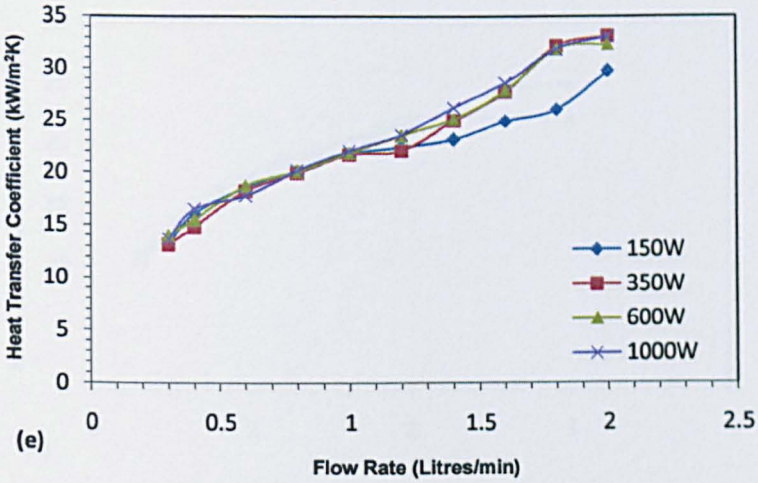

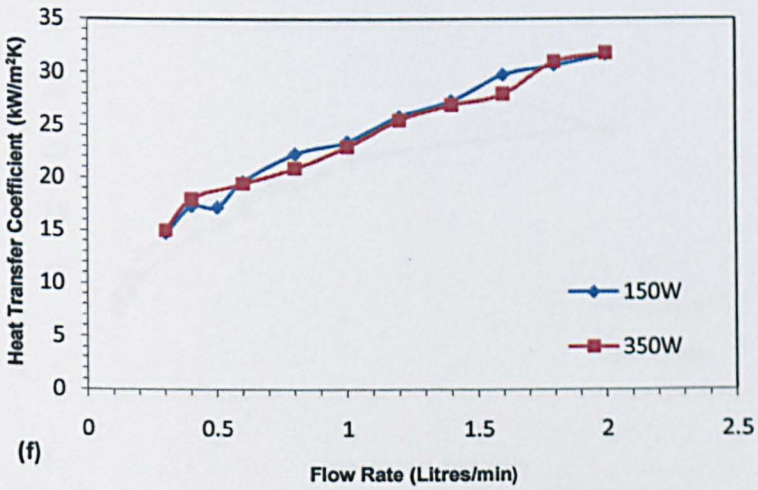

Figure 4.19 to be continued

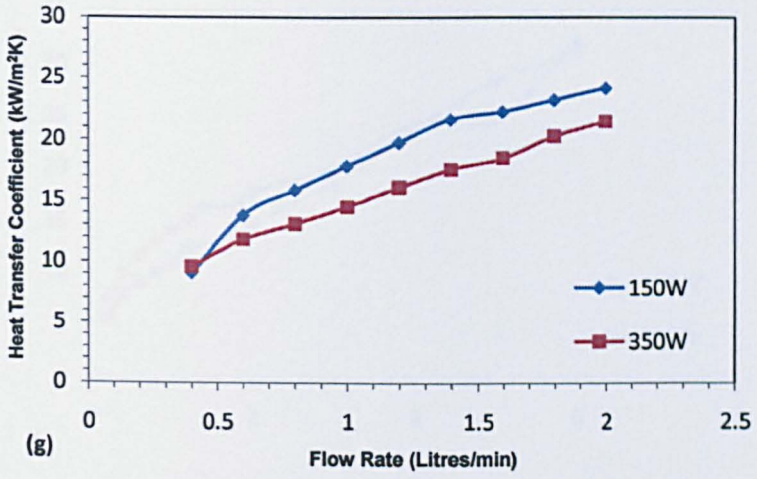

(g)

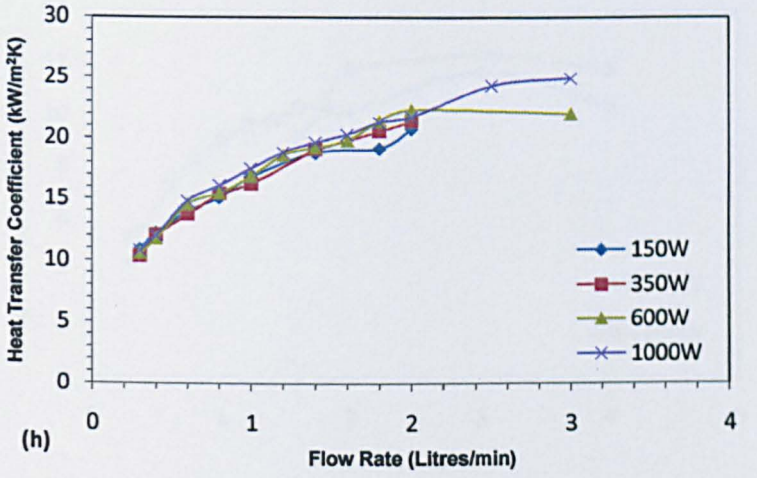

(h)

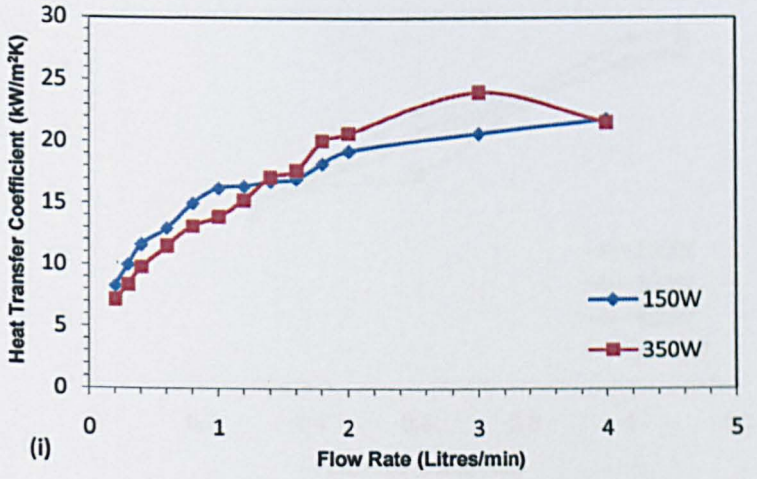

(i)

Figure 4.19 to be continued

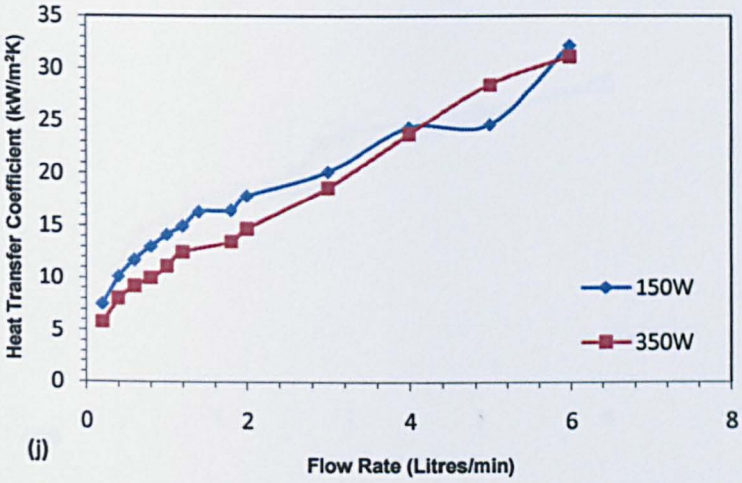

(j)

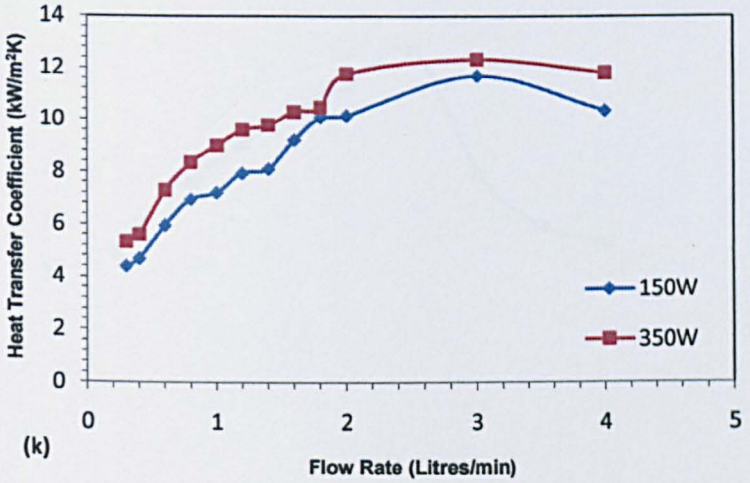

(k)

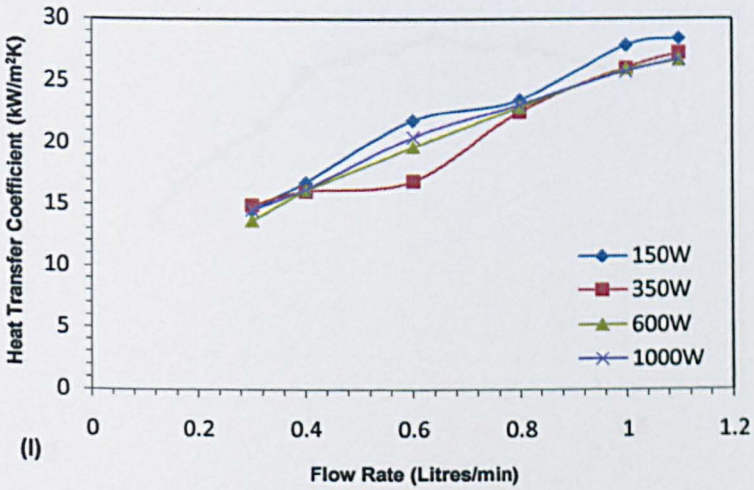

(l)

Figure 4.19 to be continued

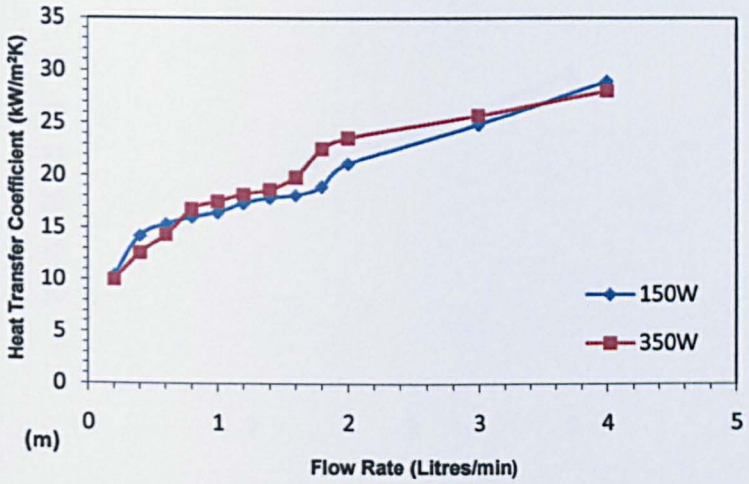

(m)

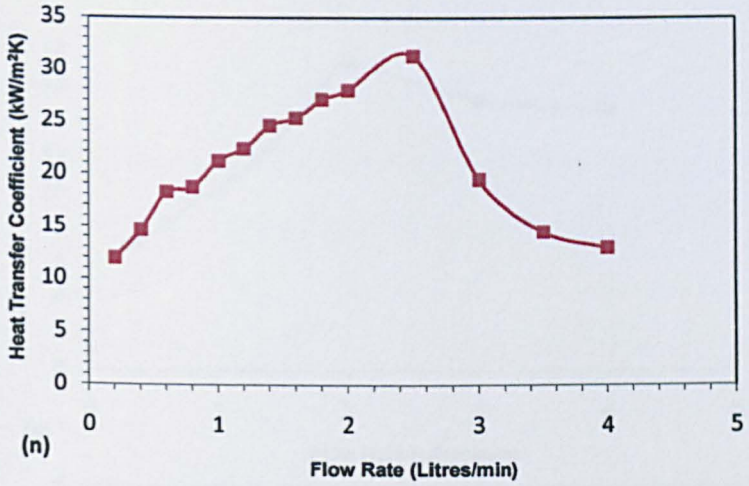

(n)

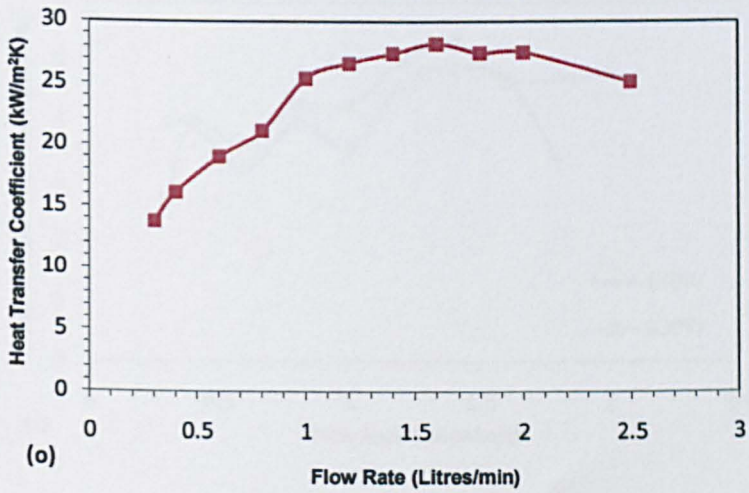

(o)

Figure 4.19 to be continued

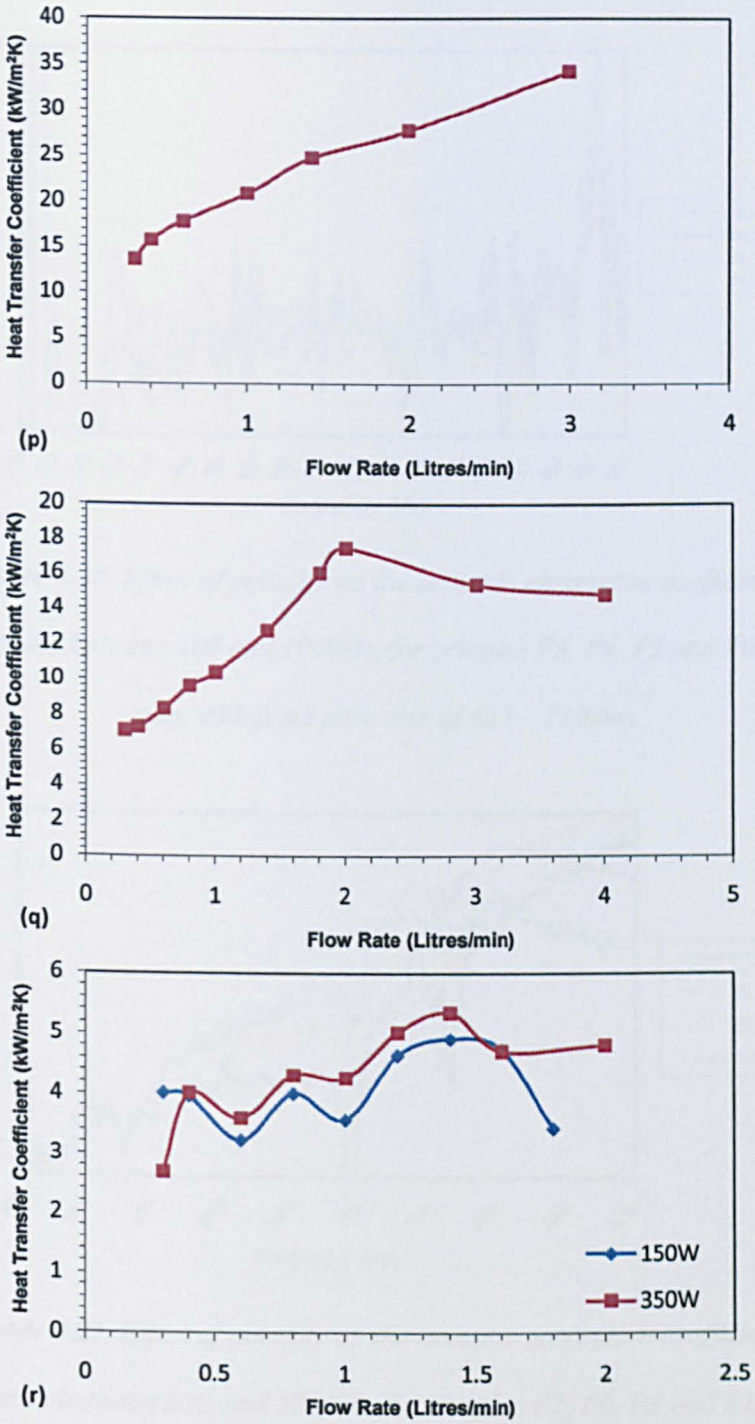

Figure 4.19 *Variations of the heat transfer coefficient with flow rate for samples E1 to E17 (a to q), and the heating chamber without a sample (r), measured with heat input powers of 150W and 350W. (n to q use a single heat input of 350W).*

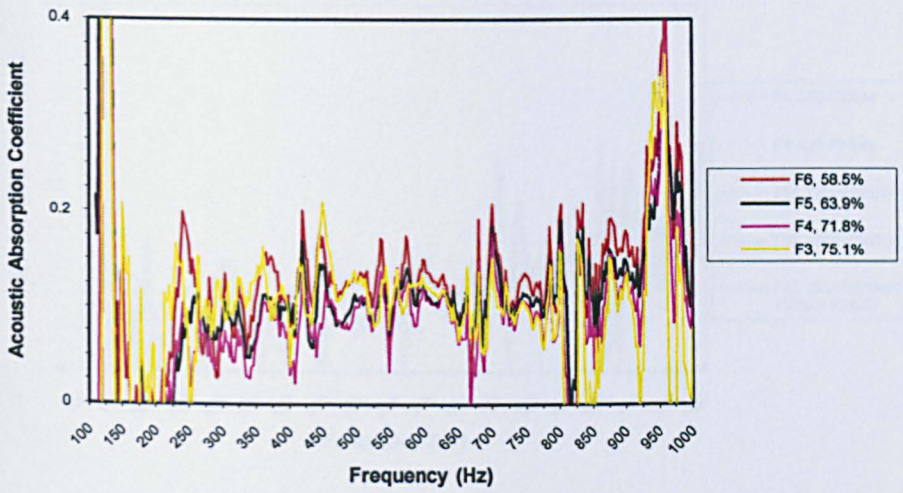

Figure 4.20 *Effect of porosity on the acoustic absorption coefficient at frequencies between 100 and 1000Hz, for samples F3, F4, F5 and F6 (No air gap, with fixed pore size of 425 – 710μm).*

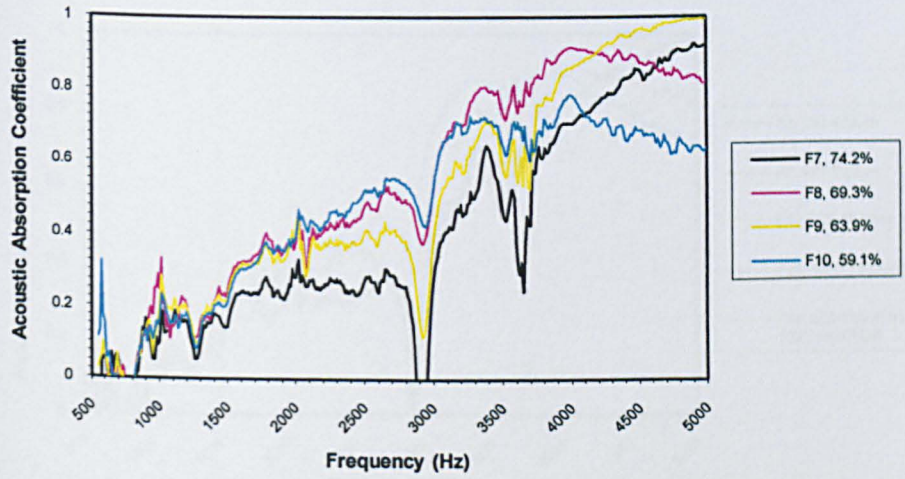

Figure 4.21 *Effect of porosity on the acoustic absorption coefficient at frequencies between 500 and 5000Hz, for samples F7, F8, F9 and F10 (No air gap, with fixed pore size of 425 – 710μm).*

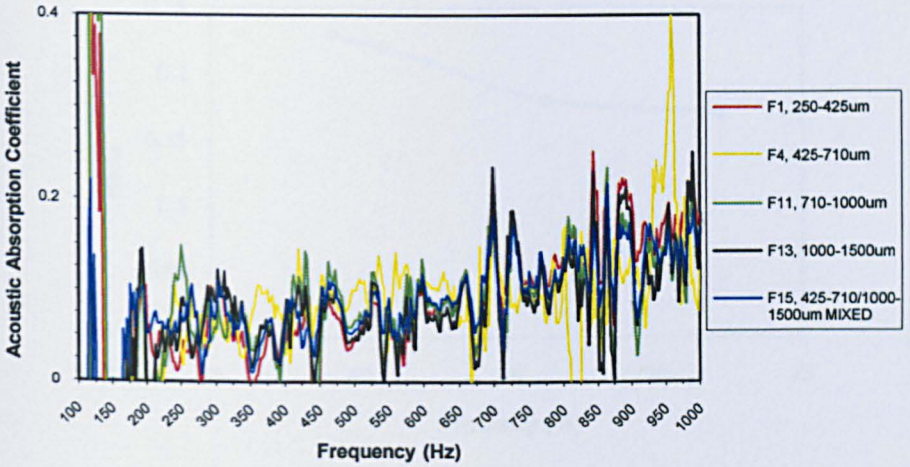

Figure 4.22 *Effect of pore size on the acoustic absorption coefficient at frequencies between 100 and 1000Hz, for samples F1, F4, F11, F13 and F15 (No air gap, with fixed porosity of 70 ± 1.8%).*

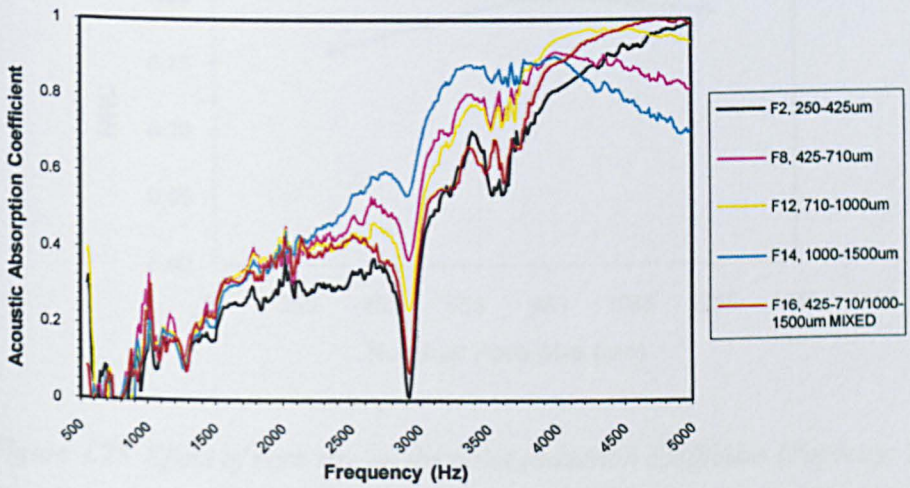

Figure 4.23 *Effect of pore size on the acoustic absorption coefficient at frequencies between 500 and 5000Hz, for samples F2, F8, F12, F14 and F16 (No air gap, with fixed porosity of 70 ± 0.8%).*

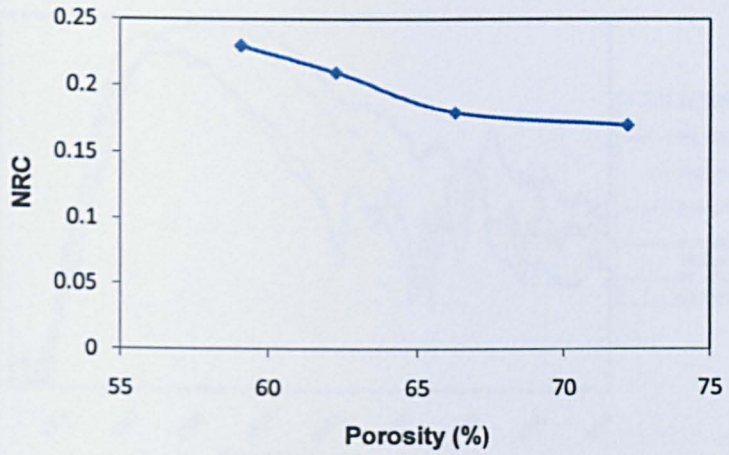

Figure 4.24 *Effect of porosity on the noise reduction coefficient (Pore size: 425 – 710μm, No Air Gap).*

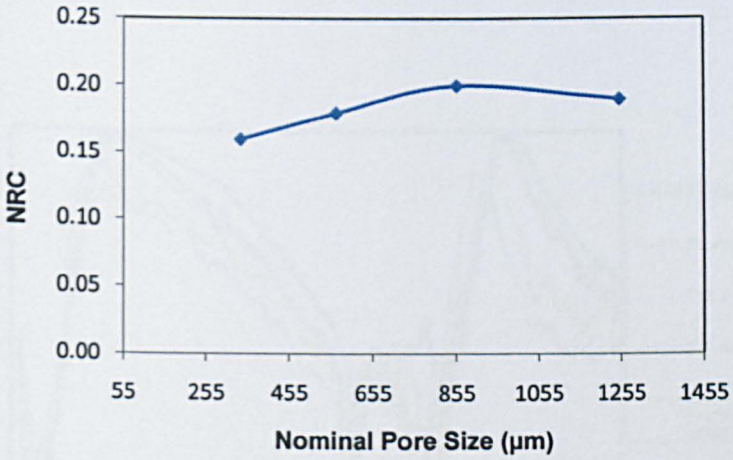

Figure 4.25 *Effect of pore size on the noise reduction coefficient (Porosity: 70 ± 1.8%, No Air Gap).*

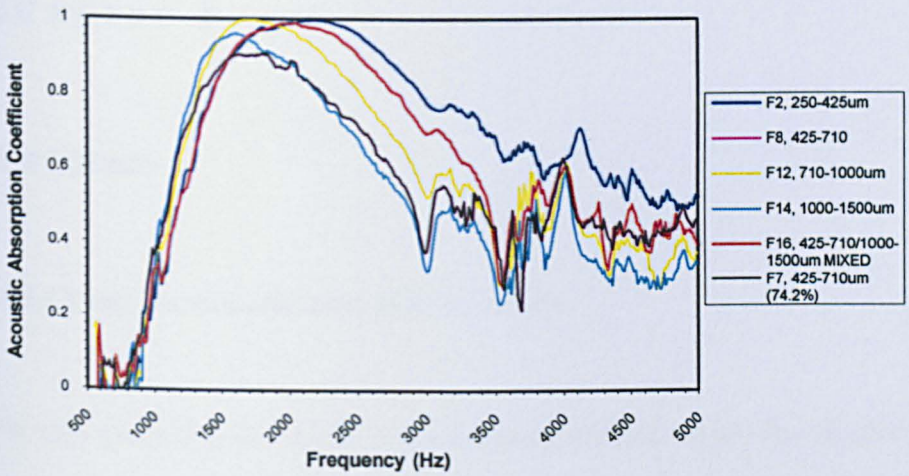

Figure 4.26 *The acoustic absorption coefficient at frequencies between 500 and 5000Hz for different pore sizes, tested with a 20mm air gap behind samples F2, F7, F8, F12, F14 and F16 (Fixed porosity of 70 ± 0.8%).*

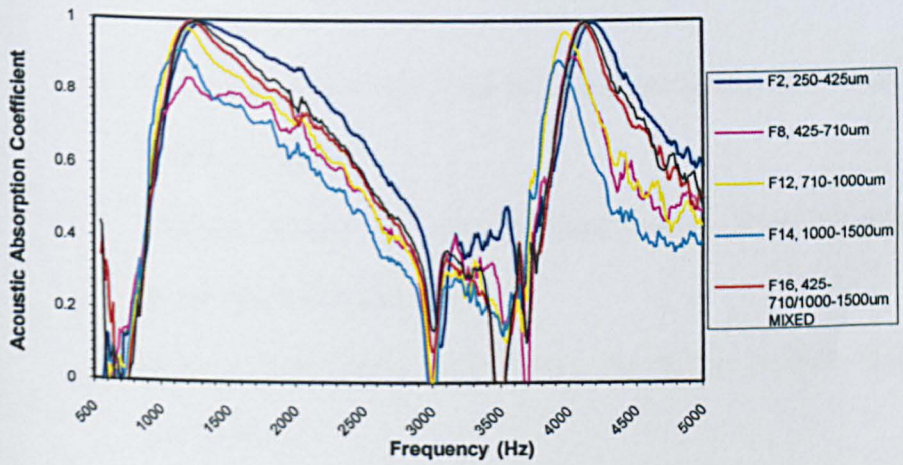

Figure 4.27 *The acoustic absorption coefficient at frequencies between 500 and 5000Hz for samples with different pore sizes tested with a 50mm air gap behind samples F2, F8, F12, F14 and F16 (Fixed porosity of 70 ± 0.8%).*

Chapter 5

DISCUSSION

5.1 LCS and As-Manufactured Microstructure

The LCS process is an efficient manufacturing method, which can be used to produce porous metals with varying parameters. The nature of the process means that porosities, pore shapes and pore sizes can be controlled to a very high degree of accuracy. Changes in the microstructure of porous metals produced by the LCS process are possible by adjusting various process parameters. These include:

- Varying pore size and shape by using the appropriate potassium carbonate granules
- Varying porosity by using different volume ratios of copper powder/carbonate granules
- Using different metal powders (Cu, Al, Fe) to produce various porous metals
- Using moulds with different sizes or shapes to produce net shape porous metal components
- Altering compaction pressure to change microstructural characteristics
- Changing the carbonate removal process

Two SEM micrographs showing the copper powder and potassium carbonate granules are shown in Figure 4.1. The copper powder particles are spherical in shape, with only very slight deviations on the sphericity. The mean size of the powder particles is approximately 40μm, but ranges between 20 and 75μm. The size of the potassium carbonate granules observed ranged between 53 and 1000μm. Again, the shape of the particles was roughly spherical, but in this case the sphericity was slightly lower, especially in the smaller particles. This can clearly be seen in Figure 4.1 (b). Mechanical sieving of the carbonate granules means that the longer they remain in the sieve, the more the particles are getting damaged by small collisions with each other and with the sieve tray. The smaller granule sizes would have been processed in the sieves for a longer period of time than the larger granules and therefore their sphericity and shape deteriorate. Figure 3.3 shows the morphology of the iron powder particles used to seal the ends of the compact. The iron powder has irregularly shaped particles with rough, uneven surfaces. The size of the particles was in the range of 100μm. As the purpose of the iron powder layers is to protect the sample from excessive oxidation, the characteristics of the iron powder particles do not really affect the quality of the porous copper sample produced.

One of the most important parameters of any porous metal is the porosity. The nominal porosity of each sample was calculated at the design stage using Eq. (3.1). Figure 4.2 shows the variation in porosity when measured by the Archimedes and point counting methods. There is very little deviation between the results, although both measurement techniques exhibit lower values to the nominal, calculated porosities. The maximum deviation between the nominal

and point-counted porosity is 5.42%. This occurs in sample A8, where the nominal porosity is 70%. The maximum deviation between the nominal porosity and the porosity measured using Archimedes method is 3.68%. This occurs in sample A3, where the nominal porosity is again 70%. The nominal porosity is calculated by assuming that no voids are present in the metal – carbonate mixture. On the one hand, as there is always a small amount of porosity in the powder mixture even after compaction, the porosity of the resultant porous metal sample is expected to be higher than the nominal porosity. On the other hand, the network of metal particles in the sample experiences shrinkage during sintering, leading to lower porosity in the sintered sample than that in the powder mixture compact. Overall, the real porosity of the porous metal can be either higher or lower than the nominal one, depending on which of the above two mechanisms are more dominant. However, the deviation of the real porosity from the nominal porosity is normally small. It should be noted that the point counting method obtains an estimated value from one surface. If the porosity of a sample is not perfectly uniform throughout its entirety, the surface at which the pores are counted will not be an ideal representation of the complete sample. This is accountable for any discrepancies between the Archimedes and point counting methods.

The effect of pore combination on the mechanical properties of an open cell aluminium foam was studied by Han *et al* (2003). They found that by combining different pore sizes in the same samples, the mechanical properties of the foam could be optimised. The nature of the LCS process allows different combinations of pore sizes and shapes as well as porosity to be controlled to a very high degree

of accuracy. It is possible using this process to manufacture a layered construction, whereby each layer has specific pore properties. This would involve layering individual Cu/K_2CO_3 mixes within the steel tube prior to compaction. Layered constructions could be useful in acoustic absorption or filtering applications.

The desired shape and size of the required porous metal structure can be achieved in two ways. Firstly, a bulk of the material can be manufactured and then machined to size using mechanical workshop equipment, such as lathes, milling machines, CNC machines, drills etc. When taking this route, it is important that machining takes place before the carbonate is removed. This avoids deformation and distortion of the outer pore structure upon shaping. The second route is to produce the required shape directly from the shape of the mould in which the preform is located. When using this option three design parameters must be taken into consideration. Firstly, the steel punch must be machined to fit the exact inner profile of the mould being used. It is important that the punch has an engineering sliding fit to ensure it does not get stuck in the mould during compaction. Secondly, the thickness of the mould wall must be sufficient to withstand the lateral forces produced upon compaction. If the walls are too thin, the mould will distort and twist during compaction. As a general rule, a minimum wall thickness of approximately $1/30^{th}$ of the perimeter is required, when mild steel is used as the mould. Lastly, the method of compaction needs to be considered. If a large piece of porous metal is required, the hydraulic press must be capable of achieving the required compaction pressure. For example, for a sample with a diameter of 22mm, a compaction of approximately 6 – 7 tons is

required to achieve a pressure of 200MPa. If the diameter of the sample is increased to 100mm, a hydraulic press capable of delivering 600 tons is required to deliver the same pressure.

Effective solid-state sintering of copper powder can only be achieved if the oxide layer at the surfaces of the metal particles is disrupted by mechanical deformation during compaction. The compaction pressure can be adjusted to alter microstructure and mechanical characteristics (Zhao *et al* 2003). An optimum compaction pressure between 200 and 300MPa exists where samples retain their original perform shapes and have good strength. Reducing the compaction pressure below 200MPa, severe spalling of the metal powder ensues, resulting in imperfect geometries. Above 300MPa, cracks are induced into the samples leading to fracture.

Carbonate removal can be achieved using two routes. This study has employed dissolution as the method of choice; however removal can also be accomplished by carbonate decomposition (Zhang and Zhao 2007). The melting point of K_2CO_3 is 891°C, at which point it begins to decompose (Zhao *et al* 2004). By elevating the furnace temperature to 950°C for a period of 30 minutes after sintering, it is possible to remove the carbonate without utilizing the dissolution process, which saves manufacturing time. The porous metal samples produced by the decomposition route generally have higher tensile strength and higher flexural strength than those produced by the dissolution route.

The microstructure of LCS porous copper shows unique characteristics when compared to existing porous metals. The result of sintering copper particles around a carbonate spacer is an extremely high internal surface area. Figure 4.3 shows how the specific surface area increases as the porosity increases. At any given pore size a higher porosity will give rise to a larger number of pores per unit volume. The microstructure of the porous copper matrix is characterized by discontinuous interstices and voids, as well as particle boundaries in the pore walls. If the number of pores per volume increases, it follows that the internal surface per unit volume will also increase. Similarly, if the porosity is fixed and the pore size decreases, the specific surface area will increase. This was observed in figure 4.4.

Effective bonding between particles is achieved through localized fusion, provided that the copper particles are not separated by oxide films. Bonding between adjacent copper particles relies on a sustained intimate contact between the metal surfaces during sintering. Small air gaps introduced into the preform can cause oxidization of the metal surfaces when exposed to the sintering temperature for a prolonged period of time.

5.2 Thermal Conductivity

Corsan's method provided a convenient, compact apparatus in which the thermal conductivity of the porous copper could be evaluated. When compared to the National Bureau of Standards, USA, agreement between the measured and

certified values of stainless steel, electrolytic iron and tungsten is better than ±3.1% throughout a temperature range between 50 and 500°C (Corsan 1984). A measurement of a copper test specimen in this study gave a thermal conductivity value of 394.7 $Wm^{-1}K^{-1}$, with the value given by the manufacturer being 396 $Wm^{-1}K^{-1}$. Temperature gradients obtained from the experiment were consistent throughout the porosity range, indicating a reasonable accuracy of the measurements using this method.

There are four mechanisms contributing to the heat transfer and thus the thermal conductivity of the porous copper samples. These mechanisms are thermal conduction through the cell walls, thermal conduction through the gas within the pores and interconnecting channels, convective effects within the pores and radiation through the cell walls. By far the most dominant of these mechanisms is solid conduction through the cell walls. However the other three will firstly be considered.

If the relative density of the porous metal is increased, or the porosity is decreased, the radiative heat transfer will decrease due to a larger amount of cell walls acting as barriers to the radiation. In a similar way, if the pore-size is decreased, the radiative heat transfer will again decrease due to the larger number of reflective surfaces within the porous metal. Radiation through the cell walls is not possible in a case of optically non-transparent metals. Radiation within the cells can be ignored, when the thermal conduction of the cell wall material is greater than 20 $Wm^{-1}K^{-1}$ (Degischer and Kriszt 2002).

Gaseous conduction in an open cell porous metal depends greatly on the relative density of the porous metal. The gas in the pores is air and the value of thermal conductivity for air at atmospheric pressure is 0.025 $Wm^{-1}K^{-1}$ (Degischer and Kriszt 2002), which is well below the thermal conductivity of solid copper. When compared to the solid conduction through the pore walls, gaseous conduction becomes insignificant. This is particularly the case for the test samples used in this study, which have relatively low porosities.

Convection within the cells is important only when the Grashof number (the ratio between force driving convection and opposing viscous force) is greater than about 1000 (Degischer and Kriszt 2002). In order for convection to take place, there needs to be sufficient space within a pore where a temperature difference can be present so that the convection current can be present. For this reason, the effect of heat transfer through convection will be greater samples with larger pores. However, convection in porous metals with a pore size less than about 10mm is negligible (Gibson and Ashby 1988). Table 4.3 shows samples B2, B3 and B4, with pore sizes of 1000 – 1500μm, 710 – 1000μm and 425 – 710μm respectively, and relative densities of 0.27 ± 0.01. The thermal conductivity of these samples varies only by 0.1 $Wm^{-1}K^{-1}$, confirming that convection can be ignored for the relatively small pore sizes used in this study.

It is well documented that the overwhelming majority of heat transfer through porous metals is via solid conduction through the cell walls (Ashby *et al* 2000, Banhart, 2001, Banhart *et al* 2003, Jackson and Leach 1993, Lu and Chen 1999, Ogushi *et al* 2004). Increasing the relative density of the porous copper sample

increases the volume of the cell walls, which in turn increases the thermal conductivity. This can clearly be seen in figure 4.6.

If the cell walls were defect free solid copper and electron movement were the only mechanism for both electrical and thermal conductivity, then electrical conductivity and thermal conductivity of the porous copper samples would be expected to conform to the same power law in equation (4.1) with an exponent n close to 2. Figures 4.6 and 4.8 show that both the variations of electrical conductivity and thermal conductivity with relative density follow a power law, confirming that electron movement is the main mechanism for electrical and thermal conduction in the cell walls. Feng *et al* (2002) found that percolation theory can also be applied to describe the dependence of the electrical conductivity of aluminium alloy foams on the relative density.

The values obtained for electrical conductivity were converted to thermal conductivity values by the Wiedemann – Franz relationship, using equation (3.6). For comparison purposes, a Mathis TCi thermal conductivity analyzer was also used on a series of four samples. The principle of the operation is based on the modified transient plane source technique and can be used to measure the thermo-physical properties of a sample material. Figure 5.1 shows a direct comparison between measurements taken using Corsan's method, the Mathis TCi method and the Wiedemann-Franz calculation method. The exponent of the fitted thermal conductivity curve determined by Corsan's method is lower than that of the curve determined by the Sigmatest method. At any relative density, the thermal conductivity measured by Corsan's method is higher than that calculated

from electrical conductivity by Eq. (3.6). To explain this phenomenon, the integrity of the cell walls and the other mechanism contributing to thermal conduction must also be considered.

In fact, the cell walls are not perfect solid copper but contain numerous defects formed during the manufacturing process. The integrity of the pore walls is highly dependant on the quality of sintering. As pressure is applied during compaction, a series of stages take place: (1) slippage of the particles with little deformation, (2) elastic compression of the individual contact areas between particles, (3) plastic deformation of these contact points to form areas of gradually increasing size and (4) large deformation of the powder mass. The chosen compaction pressure is crucial to ensure good contact points between each particle. If the compaction pressure is too low, there will be little plastic deformation of the contact points and the sintering quality will be poor. This in turn will result in poor solid conduction through the pore walls. German (1984) found that when sintering copper powders, the neck growth between particles was rapid between compaction pressures of 0 and 200MPa. Between 200 and 600MPa however, neck size showed limited growth. Zhao *et al* (2003) found that the optimum compaction pressure for liquid-state sintered aluminium foams was in the range of 200 – 250MPa. At compaction pressures below 200MPa severe spalling of the aluminium particles ensued. At compaction pressures above 300MPa, cracks were induced in the samples, leading to complete fracture.

Low conductivity metal oxides such as potassium carbonate remaining in the structure, impurities, cracks and various other defects within the cell walls,

characteristic of sintered components can largely impede the flow of electrons and thus significantly reduce the electrical conductivity. The measured electrical conductivity, and therefore the calculated thermal conductivity, is lower than that predicted for perfect cell walls and the fitted power law has a high exponent of 2.46.

The thermal conductivity in solid walls has another contributing mechanism. In addition to electron conduction, lattice vibration waves, or phonons, can also transport heat. While most of the sintering defects in the cell walls are electrical insulators, they can contribute to thermal conduction. Moreover, conduction, convection and radiation in or through the gas within the interconnected pores also contribute to thermal conductivity of the porous metal sample. For these reasons, the thermal conductivity values obtained using the Corsan's method were significantly higher than those converted from the electrical conductivity values obtained using the Sigmatest method.

The exponent of the thermal conductivity curve representing the Mathis TCi measurements has a higher value of 2.74. At any given relative density, the measured thermal conductivity is considerably lower than the results obtained using the other two techniques. The calibration modules supplied with the equipment are categorised by solids, liquids, powders and pastes and therefore the porous copper did not fit any specific category. Also, because of the nature of the structure, it is difficult to obtain a perfect contact surface, which is critical for accurate and repeatable results. Air-gaps between the sample surface and the sensor would account for the measured thermal conductivity values being lower

than those measured using the other two methods. The consistency in irregularities on each sample surface, mean that the measured values still conform to the power law. For these reasons, tests using the Mathis TCi conductivity analyser were only carried out on four samples to provide a comparison with the other two conductivity methods employed.

5.3 Permeability and Heat Transfer

5.3.1 Pressure Drop and Permeability

The test apparatus used an open flow arrangement to test the permeability of the porous copper test samples. The open flow system meant that a pump was not necessary to drive the coolant through the test samples. Instead, the coolant was delivered via the mains water supply, through the system to the main drain. The mains water supply had a maximum pressure of 3.6bar, but varied slightly due to differences in water expenditure from other applications around the building at different times. Closing the ball valve on the feed line by 50% kept the input coolant pressure steady, resulting in a maximum deviation in input coolant pressure of 0.2bar. This slight change in supply pressure had little effect on any experiment results since the permeability was calculated by measuring the difference between input and output pressures. The maximum supply pressure of 3.6 ± 0.2bar meant that a maximum flow rate of 10 l/min was achieved through the two samples with the highest porosity, but only a low flow rate of less than 1 l/min could be attained through the two samples with lowest porosity. By

introducing a coolant pump, it would be possible to develop higher flow rates in samples with lower porosity. The Omega PXM219 transducers used to measure the input and output pressures worked well within the system, with the full-scale error of ±1% being considered negligible for the results obtained. The flow meters used had an accuracy of ±4% over the full scale and a repeatability of ± 1%. The spherical shaped float used in the flow-meter resulted in a high stability, minimizing parallax errors when taking readings for each test. Flow meters which use spinners and sensors to measure flow are available, offering a higher accuracy over larger flow ranges.

The experimental results presented in Section 4.5 clearly show that a lower pressure drop is generated when the porosity of the test sample is increased. An increase in porosity results in the flow resistance decreasing due to the smaller solid fraction within the porous copper. This effect was consistent over all samples. Figure 4.10 also shows that the pressure drop generated by a sample reduces significantly as the pore size decreases at a given porosity. This effect can be attributed to the microstructure of the porous copper. Section 4.1 described how the pores within the copper matrix are interlinked by small cavities and interstices (Figure 4.1). If the nominal pore size within a sample decreases, the pore density, or number of pores per unit volume will increase. This increase in pore density results in a higher connectivity, with more pores being interlinked. This gives the coolant flowing through the sample more flow channels per unit volume in which it can flow through, giving rise to lower flow resistance and thus a lower pressure drop at any given flow rate. The viscous permeability coefficient is related to pressure drop by Eq. (3.7). This indicates

that as the pressure drop across a sample at a given flow rate decreases, the viscous permeability coefficient will increase. Figure 4.11 shows an exponential rise in the permeability coefficient with porosity. Again, this can be explained by the connectivity of the pores. If a low porosity is considered, theoretical treatment suggests that a scenario could exist where pores are present, but they are not interlinked, resulting in a flow resistance of 100% (i.e. impermeable). This is in spite of the fact that pores are still present within the copper matrix. As the porosity is increases above 50%, the chances of one pore being connected to another will increase exponentially, resulting in an exponential increase in permeability. The pore shape had no significant effect on the permeability, when spherical and irregular shaped pores at similar porosity were compared.

Different microstructures mean that pressure drop characteristics vary extensively between porous metals (Boomsma *et al* 2003, Khayargoli *et al* 2004, Dukhan 2006, Despois and Mortensen 2005). Linear pressure drop plots show a validity of Darcy's law, while increasing Darcian flow velocities result in curves which follow the quadratic Forcheimer equation. Figure 5.2 shows the pressure drop curves of a series of metal foams from a study carried out by Khayargoli *et al* (2004). The pressure drops in this case can be seen to contain a quadratic term. The RECEMAT™ metal foams show increasing pressure drops as the pore diameter increases. This is in good agreement with the pressure drop curves for the LCS porous copper used in this study, as well as with other researchers.

For general comparison, the dimensionless Reynolds number (*Re*) can be used to describe the hydraulic characteristics of a material. The Reynolds number is

defined for porous media by Kaviany (1995). When applied to porous media, the characteristic length used in the Reynolds number is replaced by the square root of the permeability (K), as shown in equation (5.1).

$$\mathrm{Re} = \frac{\rho V \sqrt{K}}{\mu} \tag{5.1}$$

where ρ is the density of the fluid, V is the Darcian flow velocity and μ is the dynamic viscosity of the fluid. Figure 5.3 shows the variation of the Reynolds number with porosity at different pore sizes. *Re* can be seen to increase in an exponential fashion between values of 3 and 60 as the porosity increases. This indicates the characteristic low flow rates and high pressure drops in samples with low porosities. When coupled with thermal characteristics, permeability becomes a critical parameter in the design of heat exchangers.

5.3.2 Heat Transfer

The heat transfer performance of the porous copper samples was evaluated using the experimental apparatus and test procedure described in Section 3.6. Again, an open flow arrangement was used, meaning that the supply pressure of the coolant varied by ± 0.2bar. Again, this did not affect any results due to the instantaneous measurements of both the input and output coolant pressures. The thermometers used to measure the inlet and outlet temperatures of the coolant offered extremely high precision over a large temperature range, with a high response time. The relatively small temperature differences between inlet and

outlet coolant temperatures meant that accurate temperature readings were crucial to the experiment.

Section 4.6 described how the heat transfer coefficient was measured. For true heat transfer measurements, the inlet and outlet temperatures of the coolant should be measured directly at the two end surfaces of the test samples. In this experiment, however, the test samples were shorter than the heating chamber and the thermometer probes were located just outside the ends of the heating chamber. The total heat transfer coefficient, h_{TOT}, is composed of that of the porous copper sample, h_{SAMPLE}, and that of the heating chamber, h_{CH}:

$$h_{TOT} = h_{SAMPLE} + h_{CH} \tag{5.2}$$

Figure 4.19 (r) shows the relationship between the convective heat transfer coefficient and the flow rate for the heating chamber without a sample. It shows that at a flow rate of 2 l/min, the corresponding heat transfer coefficient of the heating chamber is 4.8 W/m^2K. The test samples were about 20mm shorter than the heating chamber, i.e. 20mm (or 40%) of the heating chamber was in contact with the coolant flow at any time. The heat transfer coefficients of the samples could be calculated by subtracting the heat transfer coefficient of the chamber effect from the measured total heat transfer coefficient. If h_{TOT} is measured to be 20 W/m^2K, for example, then $h_{SAMPLE} = 20 - (0.4 \times 4.8) = 18.08$ W/m^2K. This method was employed to compensate for the heating effect of the heating chamber on all the test samples, giving a more accurate calculated value of the heat transfer coefficient. Another source of error is due to the slight different

lengths of the test samples. Compared with the heating chamber effect, however, it is less significant.

Heat transfer from the heat source (heating chamber in this case) to the coolant consists of two stages: thermal conduction in the copper matrix of the porous copper sample and convection between the copper matrix and the coolant. Figure 4.12 shows how the heat transfer coefficient generally decreases with increasing porosity, at a fixed pore size. This trend is consistent over all coolant flow rates. As the porosity increases, the volume of the solid phase saturated in the coolant is reduced, resulting in a decrease in thermal conduction in the copper matrix to the coolant. It seems the thermal conduction in the copper matrix is the critical stage of the two controlling the overall heat transfer. However, there was an apparent increase in heat transfer coefficient at a porosity of 61.2%. This seems to be the result of the structural change happening in the porous copper samples around this porosity. In LCS, to achieve a soundly sintered copper matrix the copper particles need to fill completely in the interstices between the potassium carbonate particles. Around this critical volume percentage of copper particles, or of potassium carbonate particles, for the complete filling, the integrity of the copper matrix, or cell walls, is expected to vary. The sudden increase in heat transfer at a porosity of 61.2% is likely to coincide with the structural transition. Whether this is the case or not needs further investigations.

The heat transfer coefficient also increases linearly with flow rate. As the flow rate increases, convection is enhanced. For the coolant being at the same temperature, more heat is taken away by the coolant. In addition, the pressure

drop across the test sample also increases as the flow rate increases. The increase in coolant pressure causes more turbulence within the porous network. This extra turbulence causes the coolant to mix and access more of the small interstices within the structure, giving rise to more heat exchange between the solid copper surfaces and the coolant.

Section 4.6 also described how the heat transfer coefficient increases as the nominal pore size increases. Larger pores give rise to larger convective surfaces within the copper network that are able to efficiently transfer heat from the solid to the liquid phase. It should be observed that samples with a smaller pore size exhibit better permeability characteristics than those with larger pore sizes. Better permeability would suggest a better heat transfer due to the lower pressure drops generated by the sample at any given flow rate. However, the effect of large convective surfaces in the solid phase outweighs this mechanism and becomes dominant when pore size is considered in heat exchanger design.

Section 4.6 also showed that the compaction pressure applied during the manufacturing process has a significant effect on the heat transfer coefficient, with an increase in compaction pressure resulting in an increase in heat transfer. When the compaction pressure is increased, the mechanical properties of the porous copper are enhanced as a result of more effective sintering between the copper powder particles (Zhao *et al* 2005). Better particle bonding would give rise to better thermal conduction in the solid phase and better convective surfaces for heat to be dispersed into the coolant. This effect was consistent throughout all porosities and flow rates.

The heat input power delivered to the heating chamber seemed to have little effect on the heat transfer, with no definite correlation observed. An increase in heat input power resulted in increased block temperature and subsequent increase in the sample temperature. The consequence of this is that the difference between the inlet and outlet temperatures was greater, but the rate of heat transfer to the coolant was also increased. With both q and ΔT being directly related by Eq. (3.9), the convective heat transfer coefficient is expected to remain the same at any given heat input power.

A peak in the heat transfer coefficient was observed at various flow rates above 2 l/min, depending on the porosity and pore size (Figure 4.19). The open flow arrangement of the test apparatus meant that it was possible that air bubbles could enter the system. Increasing flow rates generate more turbulence within the porous structure, inducing air bubbles. At higher flows, these air bubbles could be observed at the outlet pipe going to drain. The thermal conductivity of air is approximately 24 times less than that of water (Callister 2000). If air bubbles are induced into the coolant flow, the heat transfer between the solid and the coolant would become less efficient. The amount of turbulence generated would depend on porosity and pore structure. This would give rise to the peaks observed at higher flow rates. A closed flow arrangement with the introduction of a coolant pump would eliminate these air bubbles, giving a more accurate representation of the overall heat exchanger performance.

5.3.3 Comparison with Other Heat Exchangers

Figure 5.5 shows the average Nusselt number as a function of Reynolds number for a series of samples taken from a study by Haack *et al* (2001). Samples S1 to S7 represent FeCrAlY foams manufactured by Porvair, while samples 1, 3 and 4 are aluminium foams with the data obtained from Calmidi and Mahajan (2000). The porosities of the samples range between 85 and 95%, producing high flow rates and high Reynolds numbers. The graph shows that the maximum Nusselt number from all the test samples is just below 600, with a corresponding Reynolds number of approximately 90. With a Reynolds number below 50, none of the foams tested in the study by Haack *et al* (2001) had corresponding Nusselt numbers above 400. The comparatively high Nusselt numbers at corresponding low flow rates shown in Figures 4.14 and 4.16 would suggest that LCS porous copper is a highly competitive heat exchanger, particularly when a combination of low porosity and large pore size is implemented.

Boomsma *et al* (2003) tested high porosity aluminium alloy metal foams for use as compact heat exchangers. Nusselt number increased with the coolant flow velocity, with a maximum value of 133 being achieved at a flow velocity of approximately 1.3m/s (corresponding to 25 l/min in the LCS tests). The LCS porous copper considerably out-performs the aluminium alloy metal foams, showing Nusselt numbers up to four times higher at much lower flow rates.

As well as technical performance, cost must also be taken into account when considering the design of heat exchangers. If a closed fluid flow system is used,

a device must be introduced, capable of pumping the coolant through the heat exchanger. The energy required to operate the system, may outweigh the performance. In the study made by Boomsma *et al* (2003), pressure drops generated by the alloy heat exchangers were relatively low due to the highly porous foams being tested. The pumping power required for the LCS porous copper would be considerably higher as a result of the lower porosities and the larger pressure drops.

5.4 Acoustic Behaviour

The open-celled porous copper samples used in this study demonstrate varied acoustic behaviour that is dependent on relative density (or porosity), pore size, frequency and the introduction of an air-gap between the absorber and back plate. The LCS method used to manufacture the samples in this investigation gives rise to a unique structural and morphological network of interconnected pores. Pores are interlinked via complex arrays of small channels located between a number of sintered copper particles. The channels are typically in the order of between 5μm and 20μm, approximately two orders of magnitude smaller than the pores and about 2 – 10 times smaller than the sintered copper particles.

5.4.1 Acoustic Absorption Mechanisms

There are several mechanisms which contribute to the sound absorption properties of materials (Morse 1948). These include viscous losses due to flow resistance, as the air is forced in and out of the pores, cracks and interconnecting

channels, mechanical damping within the absorber and by thermoelastic damping.

It is generally accepted that any kind of porosity improves mechanical damping due to stress concentration and mode conversion around pores (Banhart *et al* 1996). Porous absorbers are effective primarily for high frequencies with short wavelengths. Golovin and Sinning (2004) studied the different internal friction mechanisms involved in damping within cellular metals. They found that for an absorber which is fixed against a rigid wall (i.e. no air gap), the maximum particle velocity within the sound wave occurs at ¼ and ¾ wavelengths. If the thickness of the absorber is less than ¼ wavelength, the absorber will have little effect. If an air gap is established between the absorber and the rigid wall, the performance of the absorber will demonstrate almost the same performance as a thicker one. The greatest effect is attained when the distance between the rigid wall and the centre of the absorber is exactly ¼ the wavelength of the incident sound wave. This is because the maximum amplitude of both the incident and reflected waves are occurring within the absorber. The sound attenuation will obviously be constrained within a narrow frequency band and give rise to a peak in the absorption coefficient within this band.

The pore walls themselves have rough, uneven surfaces that are dictated by the sintered copper particles. These irregular surfaces, when combined with the complex network of interconnecting channels, give rise to a high flow resistance. As the sound wave travels from one pore into a smaller gap or channel, the velocity of the air decreases due to friction. If no air gap is present between the

test sample and the back plate, forcing air into the sample will raise the pressure within the pores. This will result in a significant proportion of the sound wave energy being converted to heat energy.

5.4.2 Effect of Air Gap

At frequencies below 1kHz, the introduction of an air-gap considerably enhances the sound absorption properties, as shown in figure 5.4. Increasing the air-gap also shifts the peak sound absorption coefficient towards lower frequencies.

Figures 4.20–23 show that when the absorbers are backed with no air gap, sound attenuation is poor at lower frequencies and increases steadily with frequency. This can be explained when the wavelength of the incident sound wave is considered. The wavelength, λ, is related to the speed of sound, c, and the frequency of the sound wave, f, by:

$$\lambda = \frac{c}{f} \tag{5.3}$$

It has already been noted that the maximum velocity of the sound wave occurs at ¼ wavelength (Golovin and Sinning 2004). This results in the maximum sound absorption due to internal friction and heat losses occurring at frequencies where ¼ wavelength peaks at the centre of the absorber (i.e. 5mm from the rigid wall for the 10mm thick samples). Using equation (5.3), this would result in the sound absorption coefficient peaking at approximately 16.5kHz. If a 20mm air gap is considered, the centre of the absorber is 25mm away from the rigid back wall.

This would result in the peak sound absorption due to internal friction occurring when the wavelength is 100mm. If equation (5.3) is applied, the frequency at which this peak absorption occurs is approximately 3.3kHz. Similarly, when a 50mm air gap is present, the absorption coefficient due to frictional losses should peak at frequencies of 1.5kHz and 4.5kHz. This is in agreement with the results shown in figures 4.26 and 4.27. It confirms that the sound absorption is dominated by internal frictional and viscous losses within the pores and interconnecting channels within the porous copper. If a sine wave representing the particle velocity of the sound wave is considered, the area under the curve represents the distance travelled by the air particles. By mathematically integrating the sine wave, it is possible to calculate the theoretical frictional and viscous losses over the frequency range when considering wave velocities approaching the absorber. Figure 5.6 shows a theoretical model when only these absorption mechanisms are considered with a 20mm air gap. The model is in good agreement with Figure 5.7, with the absorption characteristics showing the same trend at similar frequencies. The maximum absorption coefficient predicted by the model is approximately 0.7. When compared to the actual peak absorption coefficient of 0.9 in figure 5.7, it becomes apparent that another absorption mechanism, other than frictional damping must be occurring.

5.4.3 Resonance

When considering the interlinking of the pores with the relatively smaller gaps between the copper particles, one must also consider the effect of cavity, or Helmholtz resonance. A Helmoltz resonator comprises of an air cavity with a narrow neck. The air within the cavity has a spring-like effect at the particular

resonant frequency of the enclosed air volume. The resonant frequency for a Helmoltz resonator is given by:

$$f = \frac{c}{2\pi}\sqrt{\frac{A}{LV}} \tag{5.4}$$

where c is the velocity of sound, A is the cross-sectional area of the neck, L is the length of the neck and V is the volume of the cavity (Irwin and Graf 1979).

When the absorber is backed with no air gap, we have a possible scenario against the wall, where the pore is closed and an interconnecting channel can act as the neck of the resonator and the pore can act as the cavity. If a typical resonator with a pore whose diameter is 900μm and interconnecting channel has dimensions in the region of 10μm is considered, the resonant frequency can be calculated to be in the order of about 10kHz. In fact, the pores can collectively act as a range of cavities with various volumes and the interconnecting channels act as a range of necks of various lengths. As a consequence, there exist a range of resonant frequencies instead of a single one.

When the absorber is backed by an air gap, the enclosed volume between the absorber and the rigid back wall can be considered the cavity and the pores or channels can be thought of as the neck of the resonator. With this being the case, the resonant frequency will decrease as the air gap behind the absorber increases. If a 20mm air gap is considered for a sample with a pore size of 710 – 1000μm, a

typical value for the resonant frequency can be calculated using equation (5.4) to be in the region of approximately 500Hz. A large number of different sized channels and pores mean that there will be a wide range of different sized cavity resonators all tuned into different frequencies. This will give good sound absorption properties over a wider frequency band when all the resonators are amalgamated and lead to a higher NRC.

5.4.4 Effect of Pore Size

Figure 4.23 shows that the absorbers with the larger pore sizes exhibit the best performance up to a frequency of about 4kHz. From Eq. (5.4), it can be seen that the Helmoltz resonance within these larger pores will occur at lower frequencies than those absorbers with larger pores. As the frequency increases, the wavelength decreases and damping of the sound wave due to frictional losses begins to have more effect. As frictional losses become dominant, a crossover phenomenon arises at about 4kHz. At this point, the absorbers with the smallest pores become the best sound absorbers.

5.4.5 Effect of Porosity

Figure 4.21 shows that a higher porosity results in the worst sound absorption properties up to a frequency of approximately 4.2kHz. As the frequency is increased, damping due to frictional and viscous losses also increases and becomes the dominant sound absorption mechanism. At this point, the absorbers with the higher porosities become the best sound absorbers.

A study carried out by Han *et al* (2003) into the sound absorption properties of open-celled aluminium foams, manufactured by the infiltration process, showed that the foams had better sound absorption capacities at frequencies above 1kHz, when compared to commercial metal foams currently available. This was because of the complex pore morphology and high flow resistance, combined with rough internal pore surfaces. For samples of 10mm thickness and no air gap backing, the average NRC of the aluminium foams are lower than the NRC of the sintered porous copper samples tested in this study. The peak absorption coefficients of the porous copper are also significantly higher than those of the aluminium foam samples. This difference in performance can be explained by the more complex internal pore morphology in a sintered product than a cast product.

Acoustic absorption varies extensively throughout different porous metals and foams (Ashby 2000, Berg *et al* 2003, Lu *et al* 1999, 2000, Xie *et al* 2004, Kovacik *et al* 1999, Jiejun *et al* 2002). Most authors agree that frictional losses and thermoelastic damping are the main mechanisms responsible for acoustic absorption in porous metals. When backed with no air gap, the samples showed an excellent acoustic absorption capacity at higher frequencies, approaching 5kHz. Coupled with the relatively high half-widths of the resonant peak, this makes LCS porous copper an attractive candidate for a wide range of applications in noise and vibration control of aircraft, automobiles, machinery and construction.

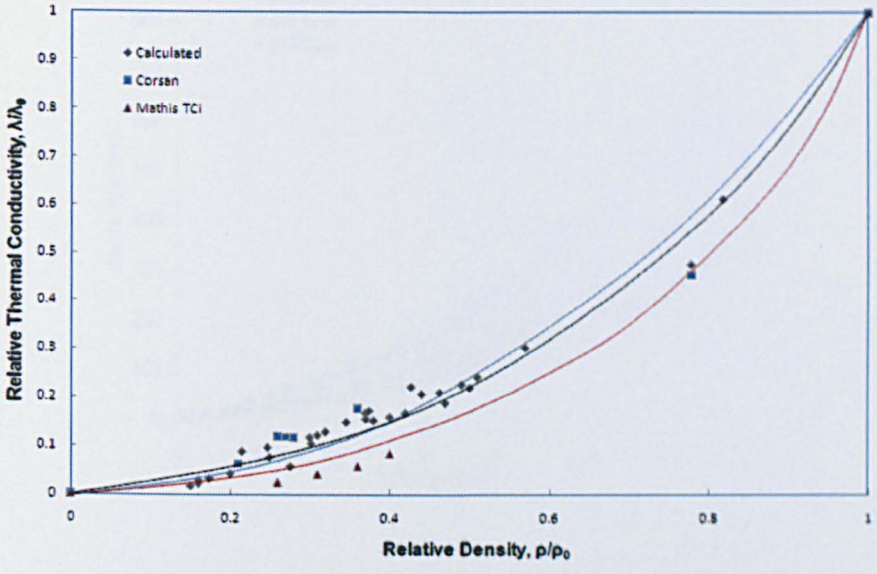

Figure 5.1 *Variation of thermal conductivity with relative density, comparing Corsan's method, the Mathis TCi analyzer method and calculations based on the Wiedemann – Franze law.*

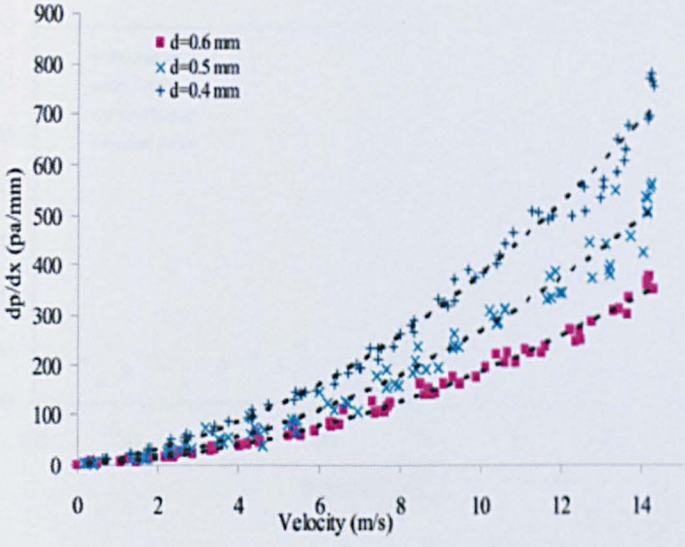

Figure 5.2 *Effect of pore diameter on the pressure drop for RECEMAT™ metal foams (Taken from Khayargoli et al 2004).*

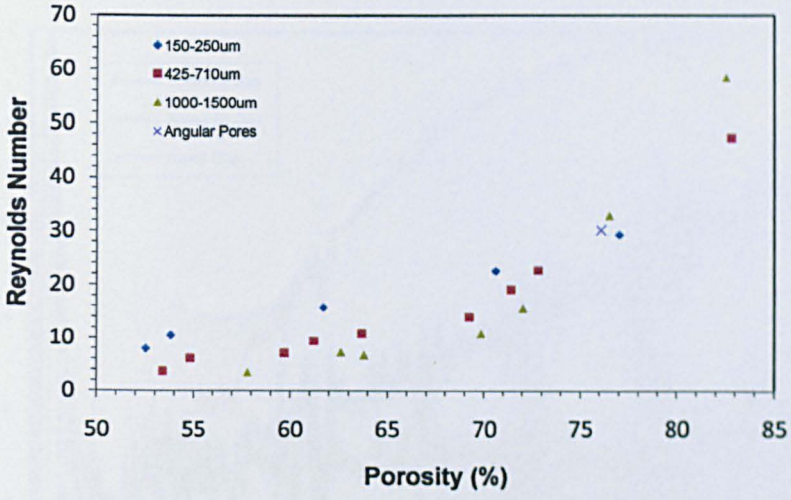

Figure 5.3 *Effect of porosity on the Reynolds Number of samples D1 to D22, at a flow rate of 2 l/min.*

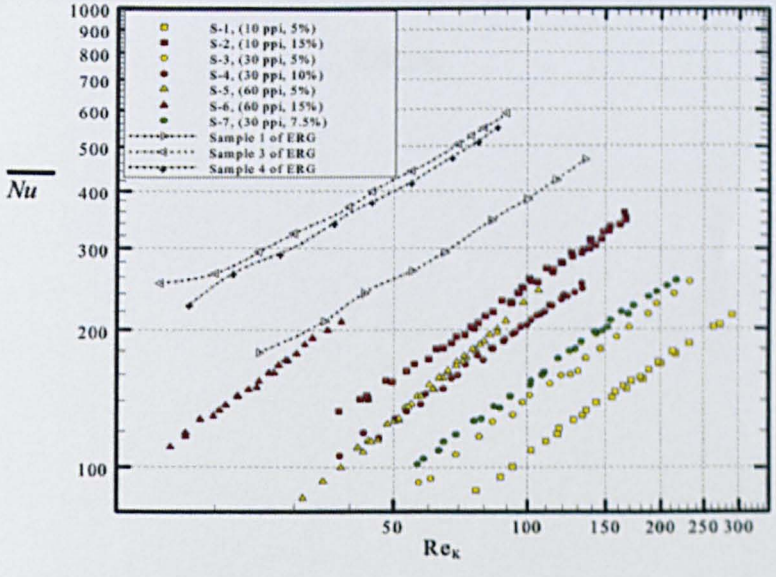

Figure 5.4 *Comparison of FeCrAlY foams (Porvair) with aluminium foams (ERG), data from Calmidi and Mahajan (2000).*

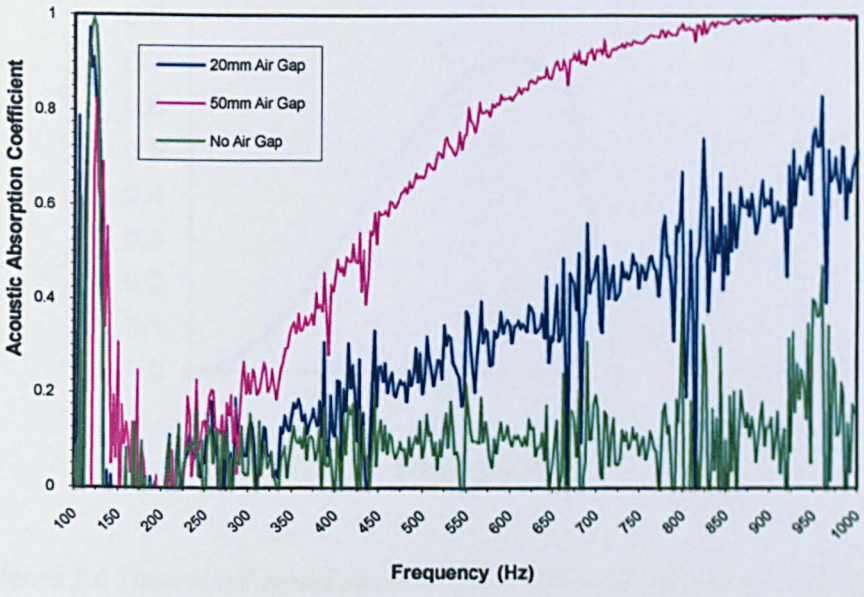

Figure 5.5 *Comparison of the effect of air gaps behind the test samples, at frequencies between 100 and 1000Hz (Porosity: 70.4 %; Pore Size: 425 – 710μm).*

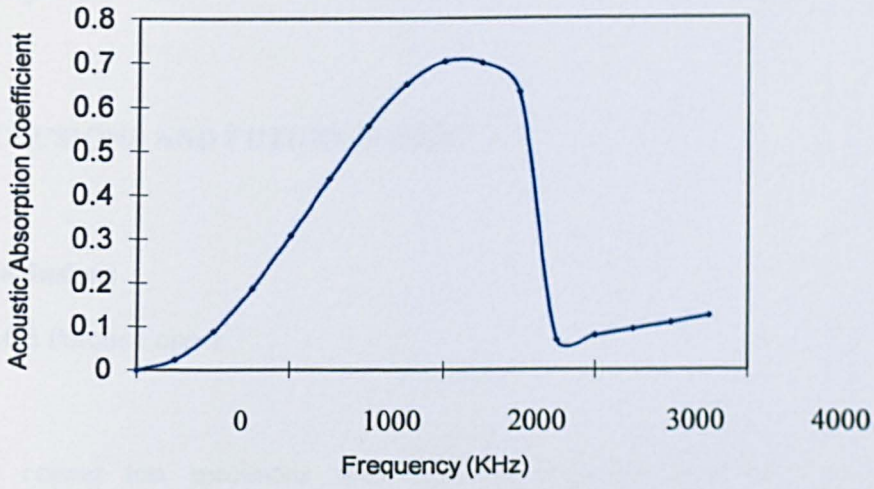

Figure 5.6 *Theoretical model showing the variation of the acoustic absorption coefficient and frequency, with an air gap of 20mm, when considering frictional and viscous losses only.*

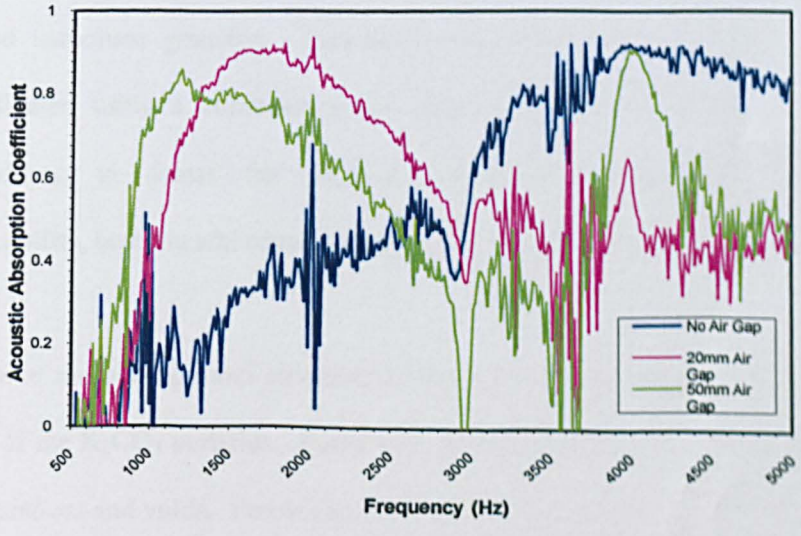

Figure 5.7 *Comparison of the effect of air gaps behind the test samples, at frequencies between 500 and 5000Hz (Porosity: 69.3%; Pore Size: 425 – 710μm).*

Chapter 6

CONCLUSIONS AND FUTURE WORK

6.1 Conclusions

6.1.1 LCS Porous Copper

Porous copper test specimens with differing pore structures have been manufactured using the LCS process. Microstructural and morphological aspects have been examined using SEM analysis, optical microscopy and quantitative metallography. Porosities of the test samples ranged between 43 and 85%, with spherical pore sizes ranging between 150 and 1500μm in diameter. Angular pores, with sizes in the region of 3mm were also produced using irregularly shaped carbonate granules. Functional properties of the test samples were investigated using a combination of original and conventional experimental procedures, to assess the thermal conductivity, electrical conductivity, permeability, heat transfer capabilities and acoustic absorption properties.

The pore morphology and structure of the LCS porous copper closely match those of the K_2CO_3 particles. Pores have rough surfaces and are interconnected by interstices and voids. Porosities and pore sizes can be accurately controlled at the manufacturing stage, resulting in a porous structure with uniform pore distribution. The LCS process provides a highly controllable and efficient system for producing high quality porous metals with differing microstructures, depending on the intended function or application.

LCS porous copper displays a wide range of good, functional properties that can be exploited in a number of practical situations. It is the possibility of combining these structural, thermal, electrical and acoustic properties that make the material attractive for unique industrial applications.

6.1.2 Thermal Conductivity

The effective thermal conductivity of LCS porous copper was measured and compared using three methods. A novel experimental technique developed by Corsan was used as the primary measurement procedure. Heat transfer through the porous copper was dominated by conduction in the solid phase, with heat transfer via convection, radiation and gaseous conduction being negligible. The thermal conductivity increased with relative density and fitted the power law, with a value for the critical exponent for thermal conductivity of 2.05. Electrical conductivity of thirty separate samples, manufactured using the same process, was also measured. The electrical conductivity values were converted to thermal conductivity values using the Wiedemann – Franz law. The as-obtained thermal conductivity also increased with relative density and fitted the power law, but with a higher critical exponent of 2.46. The disparity in the thermal conductivity values between these two methods was mainly because the sintering defects in the cell walls, such as oxides, impurities and cracks, made contributions to thermal conduction but not to electrical conduction. The pore size of the porous metal did not have any significant affect on the thermal conductivity. Thermal conductivity readings obtained from the Mathis TCi analyzer again increased with relative density, following the power law with an exponent of 2.74. This

high exponent value was explained by discrepancies in the experimental equipment and procedure.

6.1.3 Fluid Permeability

The effect of porosity and pore size on the fluid permeability of LCS porous copper was evaluated and compared using an open flow system. Samples with the lowest porosity displayed the highest pressure drops as a result of the increased flow resistance from the solid phase. Pressure drops decreased significantly as the pore size was decreased. This was attributed to the increased amount of flow channels and interstices contained between the smaller pores, giving a lower flow resistance. The viscous permeability coefficient showed an exponential increase with porosity. This was a result of an increase in pore connectivity as the porosity rises. The Reynolds number remained below 60 for all samples, indicating low fluid flows that are dominated by viscous forces.

6.1.4 Heat Transfer with Coolant

An open-flow heating arrangement was used to assess the heat transfer characteristics of seventeen LCS porous copper samples, using water as the coolant. The heat transfer coefficient was measured for each sample at various coolant flow rates and heat input powers. The Nusselt number was also calculated to compare the performance with existing heat exchangers. The heat transfer coefficient generally decreased as the porosity increased. This happens

as a result of the reduction of volume in the solid phase causing a decrease in thermal conduction from the copper network to the coolant. As the flow rate increases, convection increases allowing more heat to be removed by the coolant. Consequently a linear relationship between the heat transfer coefficient and the flow rate ensues. Pore size also had a significant effect on heat transfer performance. Larger pore sizes gave rise to increased heat transfer. The larger pores in the copper matrix exhibit larger convective surfaces, from which heat can be transferred to the coolant. Increasing the compaction pressure from 200MPa to 300MPa at the manufacturing stage resulted in superior heat transfer performance. The particle bonding was enhanced as the compaction pressure was increased, giving more integral convective pore surfaces for the heat to be dispersed from. The result was an increase in heat transfer coefficient of between 15 and 25%, over a range of porosities. The heat power input had no significant effect on the overall heat transfer performance. LCS porous copper proved to be a competitive candidate for heat exchanging devices when compared to existing porous metal materials.

6.1.5 Acoustic Absorption

The acoustic absorption performance of sixteen LCS porous copper test samples was assessed using the standing wave impedance tube method. The acoustic absorption coefficient has been measured between 100Hz and 5kHz on a number of different porous copper test samples manufactured by the LCS method. The samples show excellent sound absorption properties as the frequency approaches 5kHz, when no air gap is present behind the absorber. This is generally due to

the high amount of frictional losses within the complex network of pores and interconnecting channels. The sintered copper particles, which form the pore walls give rise to a unique uneven pore surface, which contributes to the internal frictional and viscous losses. Sound absorption at lower frequencies can be improved by the introduction of an air gap behind the absorber. Increasing the air gap behind the absorber shifts the sound absorption peak to lower frequencies. Superior sound absorbers can be made for particular frequencies by calculating the exact size of the air gap for that frequency. Sound attenuation within the porous copper samples is principally due to a combination of thermal losses, viscous losses and Helmoltz resonators. Each mechanism is dependant on the frequency, presence of an air gap, pore size and porosity of the absorber. Parameters such as pore size and porosity can be controlled easily and accurately when manufacturing porous copper using the LCS method. This gives the material the ability to be produced specifically to absorb a certain frequency band. When combined with the materials rigidity, fire retardance, electrical shielding and impact absorption properties, this makes it a good candidate to be used in a range of industrial noise control applications.

6.2 Future Work

The majority of experimental tests involved within this investigation have used spherical shaped carbonate granules to create spherical pores with sizes ranging between 150μm and 1500μm. Comparing the effect of irregularly shaped and spherical pores, as well as larger pore sizes on each of the functional properties tested within this study would prove particularly interesting. The unusual pore

morphology characteristic of LCS porous copper would also make a correlation between specific surface area and the various functional properties a worthwhile area of research.

The thermal conductivity measurements presented were all taken at a temperature in the region of 100°C, where conduction through radiation is negligible. Raising the temperature by increasing the heat input power would allow the thermal conductivity at elevated temperatures to be measured. The effect of radiative heat transfer could then be observed and compared to the results already obtained.

Improvements could be made on the permeability test apparatus by using a closed-flow system, implementing a pump to generate the fluid flow. A closed-flow arrangement would eliminate any back-pressure into the sample and ensure no air bubbles get in the system. A comparison with the gas permeability of LCS porous copper would also be beneficial.

Heat transfer could be assessed and compared when a coolant other than water is introduced. Comparing water with water-ethylene glycol, which has a much higher dynamic viscosity and lower thermal conductivity, would prove an interesting investigation. A practical experiment would be to measure the emissivity and assess the use of LCS porous copper in heat-sink applications for the cooling of high power electronic devices. Existing heat-sinks are usually manufactured from finned aluminium. This finned geometry could be recreated on a block of LCS porous copper using CNC machining. The considerable

increase in surface area when compared to traditional aluminium heat-sinks could prove beneficial to heat dissipation from the electronic device.

The acoustic absorption tests carried out in this study have concluded that LCS porous copper exhibits excellent absorption characteristics at particular frequencies. The effects of Helmholtz resonance as a primary absorption mechanism could be investigated further by using different pore size combinations and layered pore constructions. Examining these effects could lead to a "tuned" LCS porous copper absorber that is designed for maximum absorption at an exact frequency. This could prove beneficial in industrial applications when the noise reduction of monotonic equipment is desirable.

REFERENCES

Abramenko, A. N., Kalinichenko, A. S., Burtser, Y., Kalinichenko, V. A., Tanaeva, S. A., and Vasilenko, I. P. "Determination of the thermal conductivity of foam aluminium", J. Eng. Phys. And Thermophys., Vol. 72, No. 3, pp 369-373, 1999.

Albracht, F., and Lotze, G. "Acoustical investigation of sintered highly porous metal fibre structures as sound absorbers", J. of Appl. Phys. 32, pp 22-29, 1999.

Antohe, B.V., Lage, J.L., Price, D.C., and Weber, R.M. "Experimental determination of permeability and inertia coefficients of mechanically compressed aluminium porous matrices", J. of Fluids Engineering 119, pp 405-412, 1997.

Arrance, F.C.. US Patent 3287 166. 1966.

Ashby, M. F. "The mechanical properties of cellular solids", Metall. Trans. A14, p 1755, 1983.

Ashby, M.F., Evans, A., Fleck, N.A., Gibson, L.J., Hutchinson, J.W., and Wadley, H.N.G. "Metal Foams: A Design Guide", Butterworth-Heinemann, Oxford. 2000.

Baillis, D., Raynaud, M., and Sacadura, J. F. "Determination of Spectral Radiative Properties of Open Cell Foam: Model Validation", J. of Thermophysics and Heat Transfer 14, No. 2, 2000.

Banhart, J., Baumeister, J., and Weber, M. "Damping Properties of Foamed Aluminium", Mater Sci Eng A205, pp 221-228, 1996.

Banhart, J. "Manufacture, characterization and application of. cellular metals and metallic foams", J. Prog Mater Sci 46, 2001.

Banhart, J., Fleck, N. A., and Mortensen, A. ""Cellular Metals: Manufacture, Properties, Applications", MIT-Verlag, 2003.

Bejan, A. "Convection Heat Transfer", John Wiley & Sons, New York, 1995.

Bell, L. H., "Industrial Noise Control", Marcel Dekker, New York, p199, 1982.

Berg, A., Maysenholder, W., and Haesche, M., "Noise reduction of open-pore aluminium foams", in "Cellular Metals: Manufacture, Properties, Applications" by Banhart, J., Fleck, N. A., and Mortensen, A., MIT-Verlag, 2003.

Bhattacharya, A., Calmidi, V. V., and Mahajan, R. L. "An analytical-Experimental Study for the Determination of the effective thermal conductivity of high porosity fibrous foams", Applications of Porous Media Methods for Engineered Materials, AMD 233, pp 13-20, 1999.

Bhattacharya, A. and Mahajan, R.L., "Thermo physical Properties of High Porosity Metal Foams", Int. J. of Heat and Mass Transfer 45, 2002.

Bjorksten, J., and Rock, E. J. US Patent. 3794481, 1972.

Boomsma, K. and Poulikakos, D. "On the effective thermal conductivity of a three-dimensionally structured fluid-saturated foam", Int. J. of Heat and Mass Transfer 44, pp 827-836, 2001.

Boomsma, K. and Poulikakos, D. "Metal Foams as Novel Compact High Performance Heat Exchangers" J. of Fluid Engineering 124, pp 263-272, 2002.

Boomsma, K., Poulikakos, D., and Zwick, F. "Metal Foams as High Performance Heat Exchangers", M. Mechanics of Materials 35, pp 1161-1176. 2003.

Boomsma, K., Poulikakos, D., and Ventikos, Y., "Simulations of flow through open cell metal foams using an idealized periodic cell structure", Int. J. of Heat and Fluid Flow 24, pp 825-834, 2003.

Bray, K. Eng. Mater. Des. 16, 1972.

British Standard: "Acoustics-Determination of Sound Absorption Coefficient and Impedance in Impedance Tubes-Part 2: Transfer Function Method", BS EN 10534-2, London: BSI, 2001.

Callister, W. D. "Materials Science and Engineering: An Introduction", 5th Ed., John Wiley & Sons, New York, 2000.

Calmidi, V.V., and Mahajan, R. L. "The effective thermal conductivity of high porosity fibrous metal foams", J. of Heat Transfer – Transactions of the ASME 122, pp 466-471, 1999.

Calmidi, V. C., and Mahajan, R. L. "Forced Convection in High Porosity Metal Foams", Trans. Of ASME, J. of Heat Transfer 122, pp 557-565, 2000.

Carter, V.E. "Metallic Coatings for Corrosion Control", Butterworths, London, 1977.

Cohen, L.A., Power, W.A. and Fabel, D.A.. Mater. Eng. 67, p 44, 1968.

Corsan, J. M. "A compact thermal conductivity apparatus for good conductors", J. Phys. E: Sci. Instrum. 17, 1984.

Cox, J. D., Wagman, D. D., and Medvedev, V. A. "*CODATA Key Values for Thermodynamics*", Hemisphere, New York, 1999.

Darcy, H. Les "Fontaines Publiques de la ville de Dijon", Dalmont, Paris, 1856.

Davies, G.J. and Zhen, Shu. "Metallic foams: their production, properties and applications", Chapman and Hall Ltd., 1983.

Davis, P. A., Olague, N. E., and Goodrich, M. T. "Application of a validation strategy to Darcy's experiment", Advances in Water Resources 15, pp 175-180, 1992.

Degischer, H.P., and Kriszt, B. "Handbook of Cellular Metals, Production, Processing, Applications", Wiley-VCH, Berlin, 2002.

Delesse, A. "Pour determiner la composition des roches", Ann. Des Mines 13, pp 379-388. 1848.

Despois, J.F., and Mortensen, A. "Permeability of open-pore microcellular materials", Acta Materialia 53, pp 1381-1388, 2005.

Diedericks, G. P. J., and du Plessis, J. P. "Modelling of flow through homogeneous foams", Mathematical Engineering in Industry 6, pp 133-154, 1997.

Dilley, D. C. Mach. Prod. Eng. 125, 1974.

Drolet, J.P. Int. J. Powder Met. Powder Tech. 13, p 222. 1977.

Dukhan, N. "Correlations for the pressure drop for flow through metal foam", Exp. In Fluids, pp 665-672, 2006.

Du Plessis, J. P., and Masliyah, J. H., "Mathematical modeling of flow through consolidated isotropic porous media", Transport in Porous Media,3(2):145- 16, 1988.

Du Plessis, J. P., Montillet, A., Comiti, J., and Legrand, J. "Pressure. drop prediction for flow through high porosity metallic foams", Chem Eng Sci 49, pp 3545–35, 1994.

Dupuit, J. "Etudes Theoretiques et Pratiques sur le Mouvement des Eaux", Dunod, Paris, 1863.

Elliott, J.C. US Patent 2751 289, 1956.

Ettel, V. A. "New Inco Powders and Foams for Nickel Batteries", NiCad 98, Prague, 1998.

Everest, F.A. "Master Handbook of Acoustics", 4th Ed., McGraw-Hill, New York, 2001.

Fazekas, A., Dendievel, R., Salvo, L., and Brechet, Y. "Effect of microstructural topology upon the stiffness and strength of 2D cellular structures", Int. J. Mech. Sci 44, pp 2047-2066, 2002.

Fedorchenko, I.M.. Sov. Powder Metall. Met. Ceram. 18, p 625, 1979.

Feng, Y., Zheng, H., Zhu, Z. and Zu, F. "The microstructure and electrical. conductivity of aluminium alloy foams", Materials Chemistry and Physics 78, pp 196-201, 2002.

Fleck, N. A. MIT Verlag, Bremen, p 391, 1999.

Forchheimer, P. "Wasserbewegung durch Boden", Z. Ver. Deutsch. Ing. 45, 1736-1741, pp 1781-1788, 1901.

Fourie, J. G., and J. P. Du Plessis, "Pressure Drop Modelling in Cellular. Metallic Foams", Chem. Eng. Sci., 57, p 2781, 2002.

Gabe, D.R. "Principles of Metal Treatment and Protection", Pergamon Press, Oxford, 1972.

Gardner, A.R. Prod. Eng. 38, p 141, 1967.

German, R.M. "Powder Metallurgy Science", Metal Powder Industries Federation, Princeton, 1984.

Gibson, L.J., and Ashby, M.F.. Cellular Solids Tech. Pergamon Press, Oxford, 1988.

Gibson, L. J., and Ashby, M. F. "Cellular Solids: Structure and Properties", 2nd Ed, Cambridge University Press, Cambridge, 1997.

Gifkins, R.C. Materials Australia, Vol. 33 no.1, pp 11-13. 2001.

Glagolev, A.A. "On the Geometrical Methods of Quantitative Mineralogic Analysis of Rocks", Trans. Inst. Econ. Min., 59, Moscow, 1933.

Glicksman, L. R. "Ch. 5, Heat Transfer in Foams", Low Density Cellular Plastics, ed, by Hilyard, N. C., and Cunningham, A., Chapman and Hall, 1994.

Golovin, I.S., and Sinning, H.R. "Internal Friction in Metallic Foams and some related Cellular Structures", Materials Science and Engineering A 370, pp 504-511. 2004.

Haack, D., Butcher, K., Kim, T., Hodson, H.P. and Lu, T.J. "Heat Exchangers Applications for Change of Phase Media and Fuel Cell Systems" ASME International Mechanical Engineering Congress & Exposition, in: Proceedings of the V.3, PID-4B, Book No. I00548, New York, 2001.

Han, F., Cheng, H., Wang, J., and Wang, Q. "Effect of pore combination on the mechanical properties of an open cell aluminium foam", Scripta Materialia 50, pp 13-17, 2003.

Han, F., Seiffert, G., Zhou, Y., and Gibbs, B. J "Acoustic absorption behaviour of an open-celled aluminium foam", J. Phys. D: Appl. Phys. 36, pp 294-302, 2003.

Hyun, S. K., and Nakajima, H. "Anisotropic compressive properties of porous copper produced by unidirectional solidification", Mat. Sci. & Eng. A 340, pp 258-264, 2002.

Irwin, J.D., and Graf, E.R. "Industrial Noise and Vibration Control", Prentice-HaEnglewood Cliffs, NJ, 1979.

Jackson, G. V., and Leach, A. G. "Thermal conductivity of foams. II. The thermal conductivity of a layer mineral foam", J. Phys. D: Appl. Phys. 26, pp 740-745, 1993.

Jiejun, W., Chenggong, L., Dianbin, W., and Manchang, G. "Damping and sound absorption properties of particle reinforced Al matrix composite foams", Composites Science and Technology 63, pp 569-574, 2002.

Kaviany, M. "Principles of Heat Transfer in Porous Media", 2nd Edition, Springer-Verlag, New York, 1995.

Khayargoli, P., Loya, V., Lefebvre, L. P. and Medraj, M., "The impact of microstructure on the permeability of metal foams", CSME Forum 220, 2004.

Kim, S.Y., Paek, J.W. and Kang, B.H. "Flow and heat transfer correlations for porous fin in a plate-fin heat exchangers", J. Heat Transfer 122, p 572, 2000.

Klett, J., Stinton, D., Ott, R., Walls, C., Smith, R., and Conway, B. "Heat Exchangers/Radiators utilizing graphite foams", Oak Ridge National Laboratory, US Department of Energy, 2001.

Kovacik, J., Tobolka, P., and Simancik, F. "Noise Attenuation using Aluminium Foams", in "Metal Foams and Porous Metal Structures" by Banhart, J., Ashby, M.F., and Fleck, N.A., MIT Verlag, 1999.

Kuchek, H.A. US Patent 3236 706, 1966.

Kumar, A., and Reddy, R.G. "Effect of channel dimensions and shape in the flow-field distributor on the performance of polymer electrolyte membrane fuel cells", J. Power Sources 114, p 54, 2003.

Lee, S. C., and Cunnington, G. R. "Conduction and radiation heat transfer in high-porosity fibre thermal insulation", J. Thermophys. Heat Transfer 14(2), pp 121-136, 2000.

Lenel, F. V. "Powder Metallurgy: Principles and Applications", Metal Powder Industrial Federation, Princeton, NJ, USA, 1980.

Lu, T. J., Stone, H. A., and Ashby, M. F. "Heat Transfer in open-cell Metal Foams", Acta Mater 46, pp 3619-3635, 1998.

Lu, T.J., Hess, A., and Ashby, M.F. "Sound Absorption in Metallic Foams", J. Appl. Phys. Vol. 85, No. 11, pp 7528-7539, 1999.

Lu, T.J., and Chen, C. "Thermal and Fire Retardance properties of cellular. aluminium alloys", Acta Materialia 47(5), pp 1469-1485, 1999.

Lu, T.J., Chen, F. and He, D. "Sound Absorption of Cellular Metals with Semi-open pores", J. Acoust. Soc. Am. 108, pp 1697-1709, 2000.

Ma, X., Peyton, A.J., and Zhao, Y.Y. "Measurement of the electrical conductivity of open-celled aluminium foam using non-contact eddy current techniques", NDT&E International 38, pp 359-367, 2005.

Mahjoob, S., and Vafai, K. "A synthesis of fluid and thermal transport models for metal foam heat exchangers", Int. J. of Heat and Mass Transfer, 51, pp 3701-3711, 2007.

Morse, P.M. "Vibration and Sound", McGraw-Hill, New York, 1948.

Nakajima, H. Materials Science and Engineering A 386, pp 390-395, 2004.

Niebylski, US Patent 3834 881, 1974.

Ogushi, T., Chiba, H., Nakajima, H., and Ikeda, T. J. "Measurement and analysis of effective thermal conductivities of lotus-type porous copper", Appl. Phys., Vol. 95, No. 10. 2004.

Pack, J. W., Kang, B. H., Kim, S. Y., and Hyun, J. M. "Effective Thermal Conductivity and Permeability of Aluminium Foam Materials", Int. J. of Thermo Physics, 21(2), 2000.

Pizzirusso, J. Mach. Des. 53, p 135, 1981.

Singh, R., and Kasana, H. S. "Computational aspects of effective thermal conductivity of highly porous metal foams", J. App. Thermal Engineering 24, pp 1841-1849, 2004.

Sosnik, B. U.S. Pat. Nos. 2434775 and 2553016, 1948.

Sullins, A. D., and Daryabeigi, K. "Effective Thermal Conductivity of High Porosity Open Cell Nickel Foam", 35th AIAA Thermophysics Conference, 2001.

Sun, D. X., and Zhao, Y. Y. "Static and Dynamic Energy Absorption of Al Foams Produced by the Sintering and Dissolution Process", Metall Mater Trans 34B, pp 69-74, 2003.

Tadrist, L. and Miscevic, M. "About the Use of Fibrous Materials in Compact Heat Exchangers", Experimental Thermal and Fluid Science, 2003.

Tao, X. F., Zhang, L. P., and Zhao, Y. Y. "Mechanical Response of Porous Copper Manufactured by the Lost Carbonate Sintering Method", Mat. Sci. Forum Vols. 539-543, pp 1863-1867, 2007.

Thiele, W. Met. Mater. 6, pp 349– 52, 1972.

Thomson, E. "Quantitative Microscopic Analysis", J. Geol. 38, 3, p 193, 1930.

Tracey, V.A.. Int. J. Powder Met. 12, p 25. 1976.

Underwood, E.E. "Quantitative Stereology", Addison-Wesley, 1970.

www.imechanica.org/node/2979 (Accessed on 14/11/08).

www.metalfoamheatexchangers.com (Accessed on 14/11/08).

Xie, Z., Ikeda, T., Okuda, Y., and Nakajima, H. "Sound absorption characteristics of lotus-type porous copper fabricated by unidirectional solidification", Materials Science and Engineering A386, Issues 1-2, pp 390-395, 2004.

Yarnton, D. Eng. Mater. Des. 9, p83, 1966.

Zhang, E. and Wang, B. "On the compressive behaviour of sintered porous coppers with low to medium porosities – Part I: Experimental Study", Int. J. of Mech. Sci. 47, pp 744-756, 2004.

Zhang, H.Y., Pinjala, D., Joshi, Y.K., Wong, T.N., Toh, K.C., and Iyer, M.K..IEEE "Transactions on Components and Packaging Technologies", Vol. 28, No. 2, pp 272-280. 2005.

Zhang, L. P., and Zhao, Y. Y. "Fabrication of high melting-point porous metals by lost carbonate Sintering Process via Decomposition Route", Journal of Engineering Manufacture, 222, pp 267-271, 2007.

Zhao, Y.Y., and Sun, D.X. "A Novel Sintering-Dissolution Process for Manufacturing Al Foams", Scr. Mater. 44, pp 105-110, 2001.

Zhou, C.Y., Lu, T.J., Hodson, H.P., and Jackson, J.D. "The temperature dependence of effective thermal conductivity of open-celled steel alloy foams", Materials Science and Engineering A 367, pp 121-131, 2003.

Zhao, Y. Y., Fung, T., and Zhang, L. P. "Lost carbonate sintering process for manufacturing metal foams", Scripta Materialia, 52, pp 295-298, 2005.